Tuning the electronic properties of Zr UiO-66 through defect-functionalised multivariate modulation.

Carmen Rosales-Martínez, Marcelo Assis,* Celia Castillo-Blas,* Isabel Abánades Lázaro*

Table of Contents

S.1. General Experimental Remarks

Powder X-Ray Diffraction (PXRD): PXRD profiles were collected in Kapton capillary at room temperature using a D8 discovery Bruker diffractometer from 2 to 40 2Θ degrees using copper radiation (Cu Kα = 1.5418 Å), with a 0.015 step size (University of Valencia). Pawley refinements were carried out using TOPAS v.7 software.

Thermogravimetric Analysis (TGA): were carried out with a Mettler Toledo TGA/SDTA 851 apparatus between 25 and 800 °C under ambient conditions (10 °C·min^{-1}scan rate and an air flow of 9 mL·min−1). (University of Valencia)

Nuclear Magnetic Resonance Spectroscopy (NMR): NMR spectra were recorded on a Bruker AVIII 300 MHz spectrometer. (University of Valencia)

Gas Uptake: N_2 adsorption and desorption isotherms were performed in a Tristar II Plus Micromeritics sorptometer, at 77 K. Activation was set at 120ºC, under vacuum, for 24 hours on the already activated samples.

Scanning Electron Microscopy (SEM) and single point energy-dispersive X-Ray analysis (EDX): particle morphologies and dimensions were studied with a Hitachi S-4800 SEM at an accelerating voltage of 20 kV. (University of Valencia)

Energy-dispersive X-Ray analysis (EDX) mapping: the mapping of different elements was studied using a SCIOS 2 field emission scanning electron microscope with focused ion beam at an accelerating voltage of 20 kV. (University of Valencia)

Fourier Transform Infrared Spectroscopy: IR spectra of solids were collected using a Shimadzu Fourier Transform Infrared Spectrometer, FTIR-8400S, fitted with a Diamond ATR unit. (Universityof Valencia)

Dynamic Light Scattering and Z-potential: Colloidal analysis and Z-potential were performed by DLS with a Zetasizer Ultra potential analyser equipped with Non-Invasive Backscatter optics (NIBS) and a 50 mW laser at 633 nm. (University of Valencia).

Photoluminescence (PL) measurements: PL emissions were measured at room temperature using a MonoSpec 27 Jarrel-Ash monochromator coupled with a Hamamatsu R446 photomultiplier using excited by a Innova Argon-ion laser. (λ_{exc} = 350.7 nm; 2.57 eV, 200 mW). The PL emission spectra were deconvoluted using Voigt-type functions with PeakFit™ software, fixing three distinct components located at 410, 481, and 542 nm for all spectra. (University Jaume I)

Pair Distribution Function (PDF): Total scattering data were collected using an X-ray energy of 38 KeV (λ = 0.3269 Å) at the BL04 (MSPD) beamline, ALBA synchrotron, Spain. All powder samples were ground and loaded into kapton capillaries (1 mm inner diameter) to heights of 15-25 mm sealed with plasticine and mounted in the standard BL04 (MSPD) pins (1.2 mm of diammeter). Total scattering data were collected at room temperature for the background (i.e. empty instrument), empty kapton capillary and for all samples in a Q range of 0.55 – 23.0. Subsequent Fourier transformation of the normalised total scattering data produced in a real space pair distribution function D(r) for each material. In this work, we use the D(r) form of the pair distribution function to accentuate high r correlations. All processing of the total scattering data was performed using GudrunX following well-documented procedures. [1,2]The structural model was calculated using PDFGUI from the optimized model of the reported UiO-66 fcu.[3]

Band gap measurements: UV-Vis diffuse reflectance spectroscopy (DRS) was performed on a Jasco V-670 spectrophotometer using an integrated Labsphere in the range 200-900 nm. (University of Valencia)

S.2. Materials and Synthesis

All reagents unless otherwise stated were obtained from commercial sources and were used without further purification.

Synthesis: In 8 mL vials, $ZrCl_4$ (0.45 mmol, 1 equivalent), terephthalic acid (0.45 mmol, 1 equivalent), and the modulators (0.45 mmol, 1 equivalent) were dissolved in 5 mL of DMF with 0.35 mL of glacial acetic acid. The reaction mixtures were sonicated for 5 minutes and placed in an oven at 120ºC. After 24 hours, the reaction mixtures were cooled down to room temperature.

Activation protocols: The resultant powder was collected by centrifugation (5000 rpm, 5 min) and washed with DMF (X3) and MeOH (x3) through dispersion-centrifugation cycles. The samples were dried at room temperature overnight and further activated by stirring the samples in MeOH for approximately 24 hours, after which 2 further MeOH dispersion-centrifugation cycles were performed. The samples were further dried under vacuum at 120ºC for 24 hours before characterization.

S.3. Characterisation
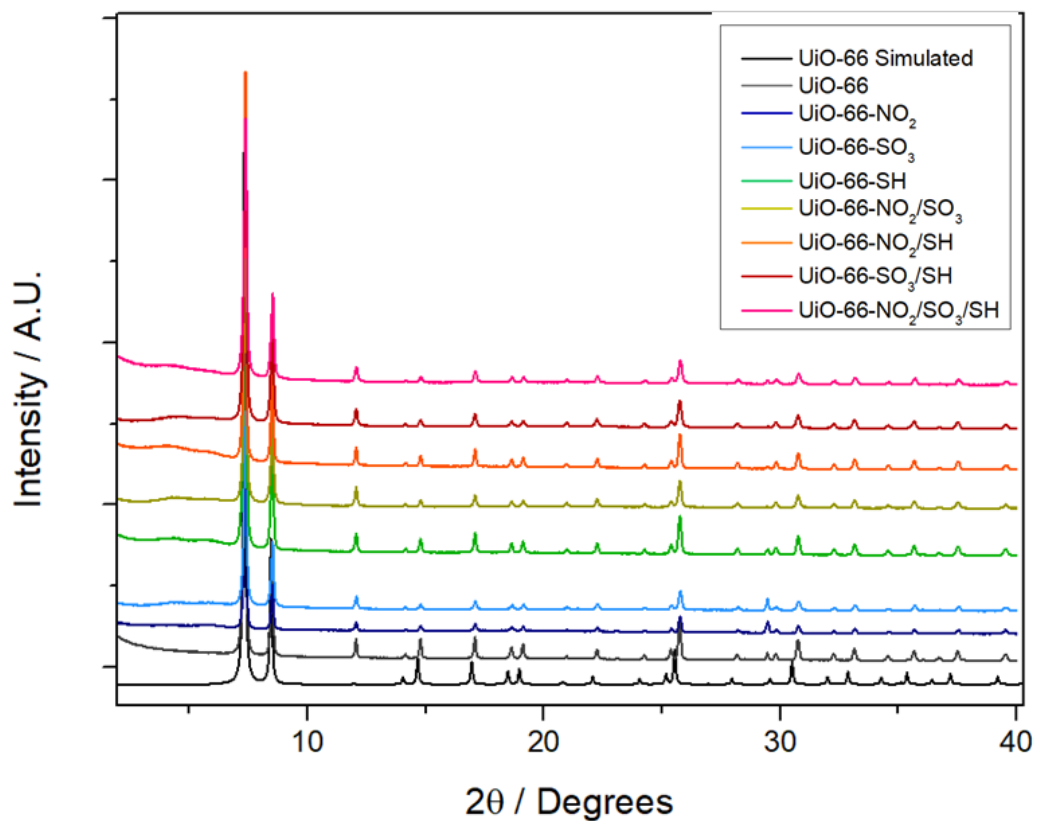
S.3.1 Powder X-Ray Diffraction (PXRD)

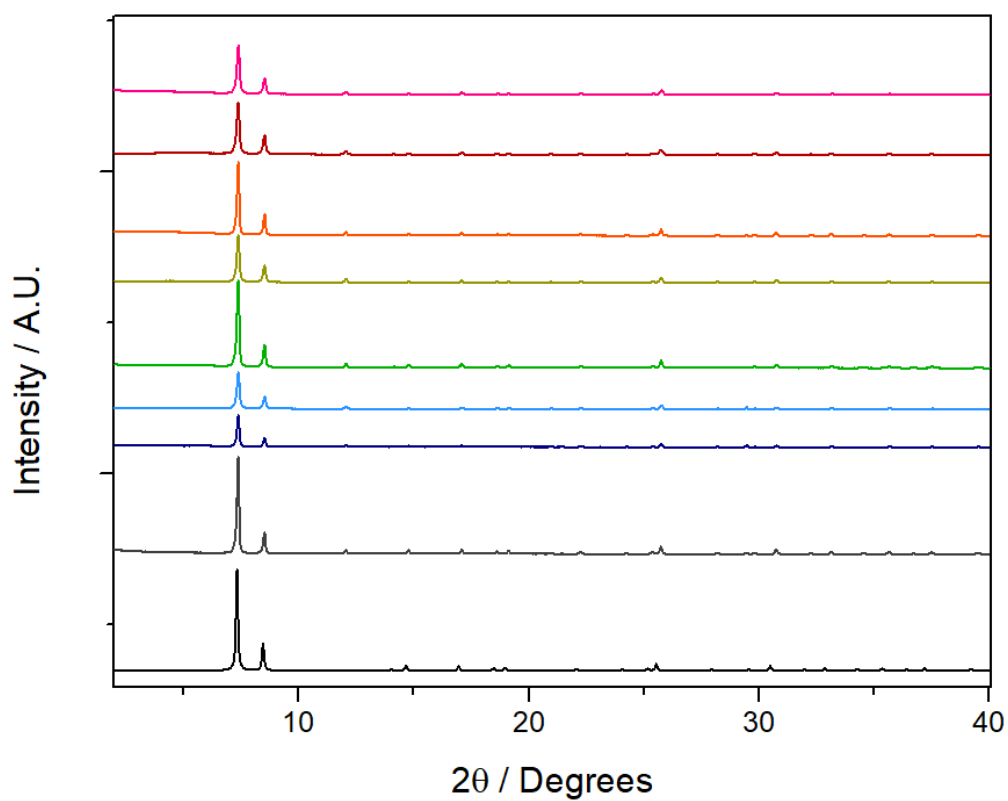**Figure S1:** PXRD patterns compared to simulated UiO-66.

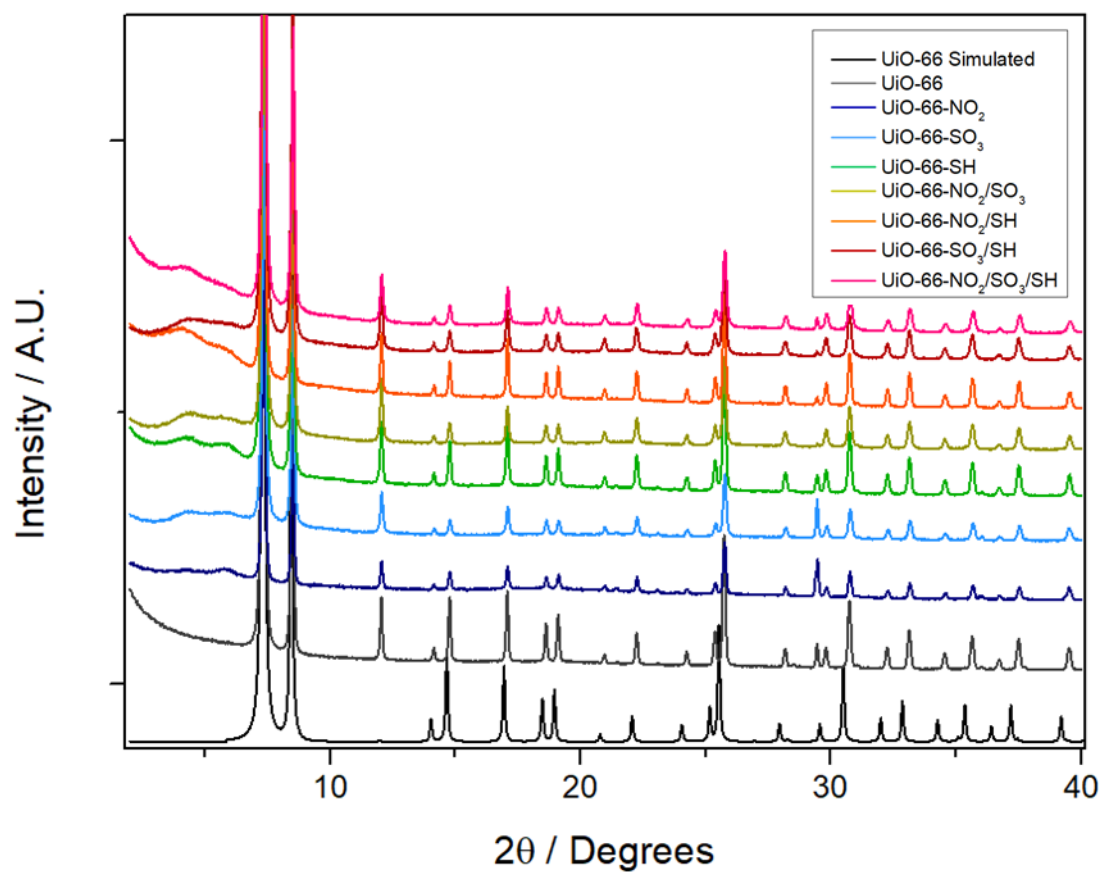**Figure S2:** PXRD patterns compared to simulated UiO-66. Legend in Figure S1 applies.

Figure S3: Zoom of the PXRD patterns compared to simulated UiO-66, showing the appearance of *reo* phase features.

Table S1. Summary of results from Pawley refinements.

| Material	R_p	R_{wp}	Space group	Zero	Lattice parameter	Profile parameters	Lattice parameter reported from literature [4]
UiO-66 pristine	7.36 %	11.80 %	*Fm-3m*	-0.0242 (4)	a = 20.7346 (7)	U = 0.203 (9) V = -0.031 (9) W = 0.0072 (6)	20.7680(6)
UiO-66-NO$_2$	9.51 %	5.12 %	*Fm-3m*	-0.0219 (5)	a = 20.7210 (9)	U = 0.220 (5) V = -0.038 (15) W = 0.0087 (9)	
UiO-66-SO$_3$	8.88 %	5.17 %	*Fm-3m*	-0.0191 (5)	a = 20.7174 (8)	U =0.29 (4) V =-0.059 (15) W = 0.0073 (9)	
UiO-66-SH	9.41 %	6.37 %	*Fm-3m*	-0.0243 (4)	a = 20.7286 (6)	U = 0.225 (33) V = -0.043 (11) W = 0.0094 (7)	
UiO-66-NO$_2$/SO$_3$	5.46 %	4.11 %	*Fm-3m*	-0.0197 (3)	a = 20.7299 (4)	U = 0.27 (3) V = -0.054 (8) W = 0.0074 (5)	
UiO-66-NO$_2$/SH	8.61 %	5.48 %	*Fm-3m*	-0.0216 (4)	a = 20.722 (6)	U = 0.22 (3) V = -0.0341 (10) W = -0.0077 (6)	
UiO-66-SO$_3$/SH	5.79 %	4.13 %	*Fm-3m*	-0.0219 (3)	a = 20.7324 (5)	U = 0.24 (3) V = -0.041 (11) W = 0.0081 (7)	
UiO-66-NO$_2$/SO$_3$/SH	5.06 %	3.46 %	*Fm-3m*	-0.0193 (3)	a = 20.7141 (5)	U = 0.28 (3) V = -0.059 (11) W = 0.0089 (7)	
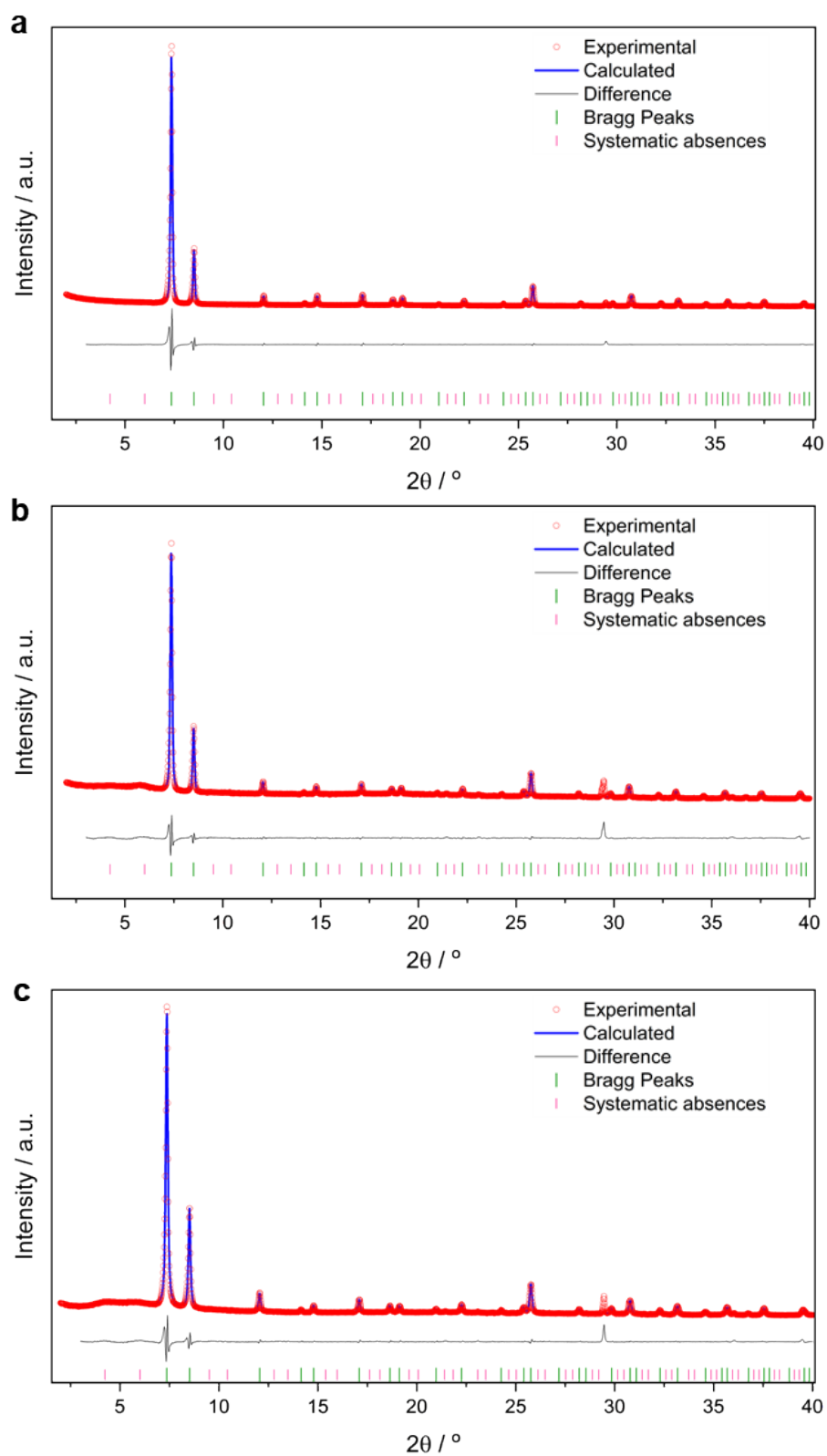
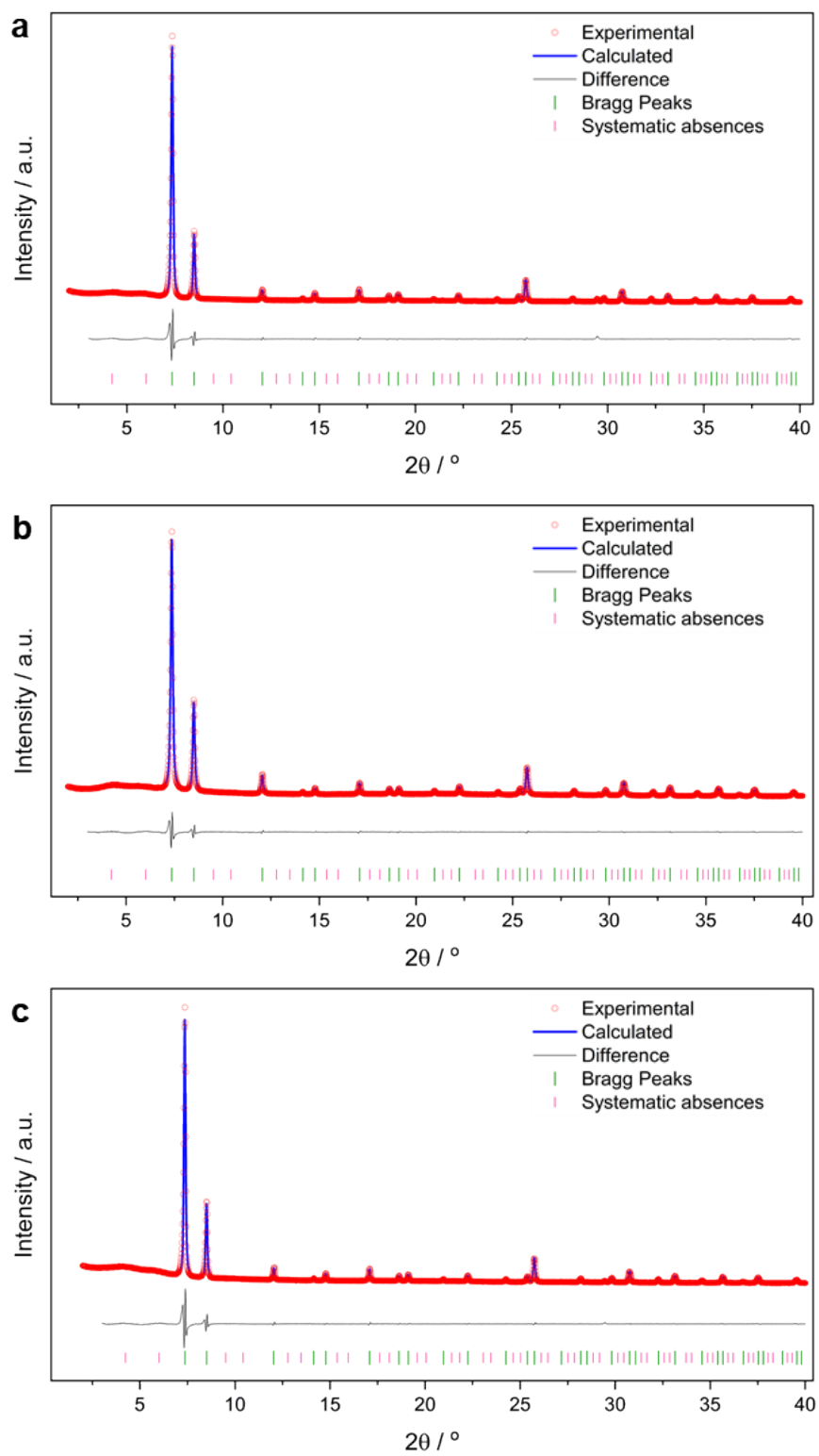**Figure S4**. Pawley refinement of the **a**. UiO-66 pristine, **b**. UiO-66-NO$_2$ and **c**. UiO-66-SO$_3$.

Figure S5. Pawley refinement of the **a**. UiO-66-SH, **b**. UiO-66-NO$_2$/SO$_3$ and **c**. UiO-66-NO$_2$/SH.
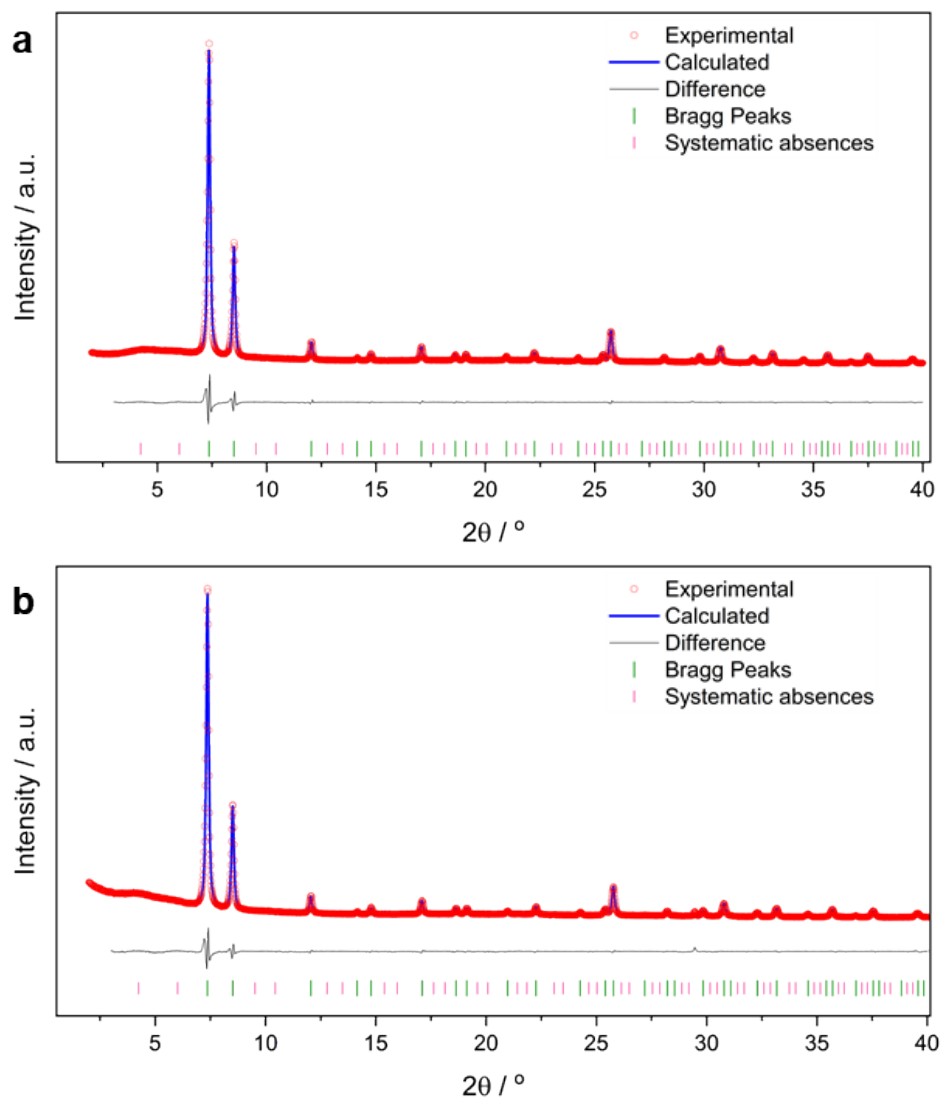
Figure S6. Pawley refinement of the **a**. UiO-66-SO$_3$/SH and UiO-66-NO$_2$/SO$_3$/SH.

S.3.2 Proton Nuclear Magnetic Resonance (^{1}H NMR)

Benz-X modulators were present in the ^{1}HNMR profiles alongside with formic acid coming from the decomposition of DMF during synthesis, and acetic acid. Incorporation of modulators and defect-compensating species, is expressed as the **molar ratio** (R_{mod}) between modulator and bdc, $Rmod = \dfrac{Mod}{bdc}$ and as the **molar percent** of modulator (mol%) compared to bdc, mol% $= \dfrac{Mod}{Mod + bdc} * 100$, while the **total modulator percent** (total mod%) is calculated taking into account all modulators and bdc,

$$total\ mod\% = \frac{Mod1 + mod2 + mod3...}{Mod1 + mod2, mod3... + bdc} * 100$$

The terephthalic acid linker appears as a singlet at *ca.* 8.1 ppm (4H). The singlet that corresponds to 1 H at *ca.* 7.9 ppm is attributed to DMF, while the singlet at *ca.* 8.2 ppm is attributed to formic acid (1H) comping from the decomposition of DMF during synthesis.[5] The modulator signals that have been used to perform the integrations that result in the estimation of the modulator content compared to the linker, are represented in **Figure S7**, and each of them integrates two protons. It is important to comment, that due to the low integration of modulator signals in comparison to the linker, we consider the values provided as an estimation.

Please note that minor shifting of these signals can be observed due to the use of deuterated sulphuric acid to digest the MOFs for ^{1}H NMR analysis.
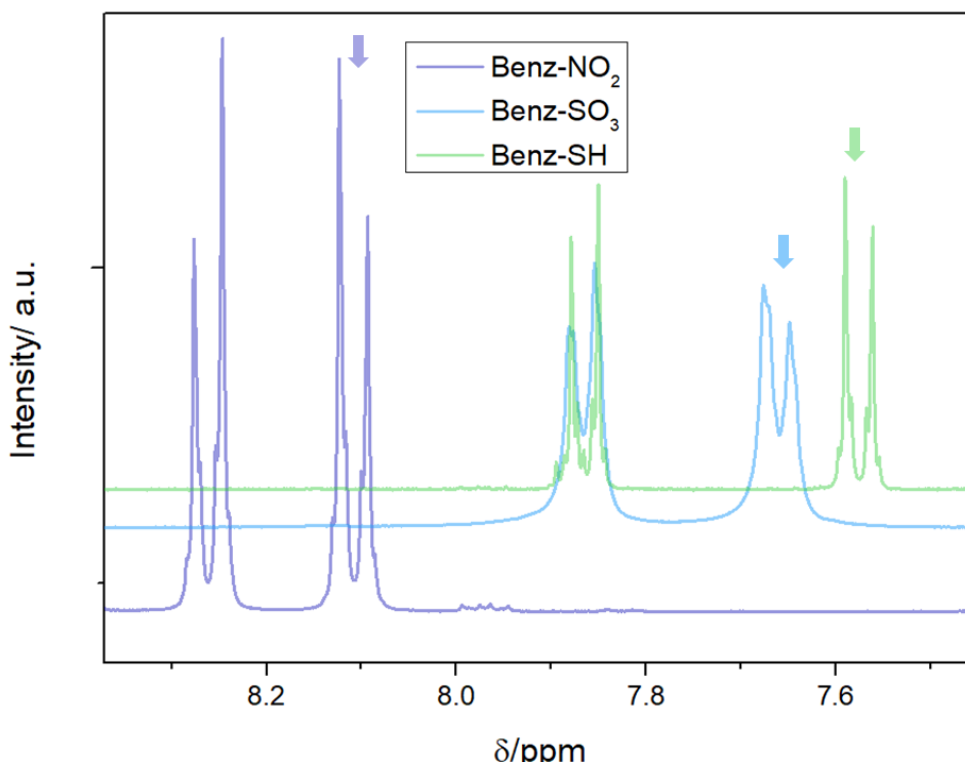

Figure S7: ^{1}HNMR profiles of free modulators in acidified DMSO, highlighting the signals that are used for estimation of the modulator/linker ratios and molar percent through acid-digested ^{1}H NMR. Dark blue Benz-NO$_2$, light blue Benz-SO$_3$ and green Benz-SH.

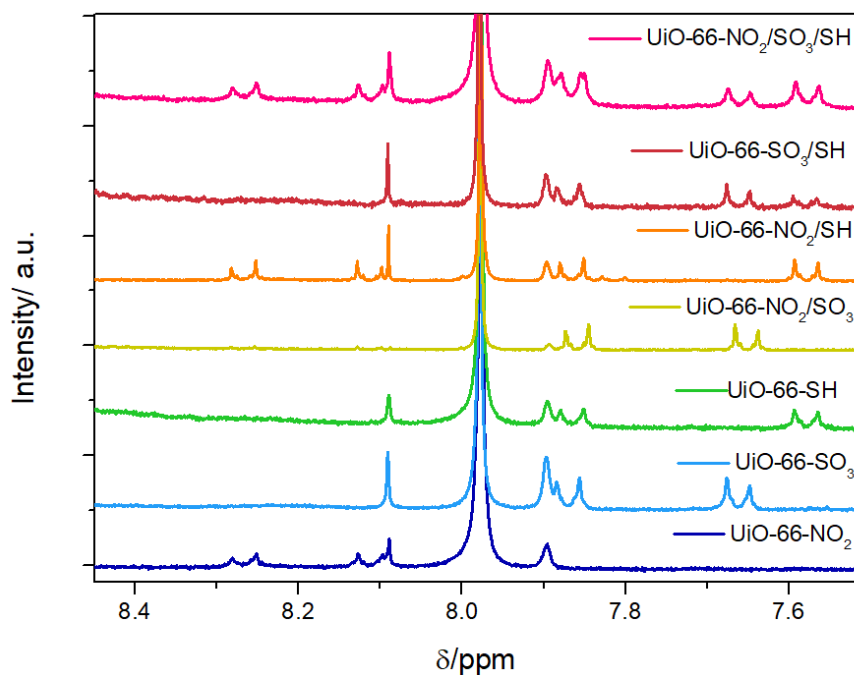## S.3.2.A. ^{1}H MNR of activated samples

Figure S8: Amplification of ^{1}HNMR profiles acid-digested samples after dispersion centrifugation cycles, without a 24-hour wash, showing the presence of modulators, formic acid, and DMF.
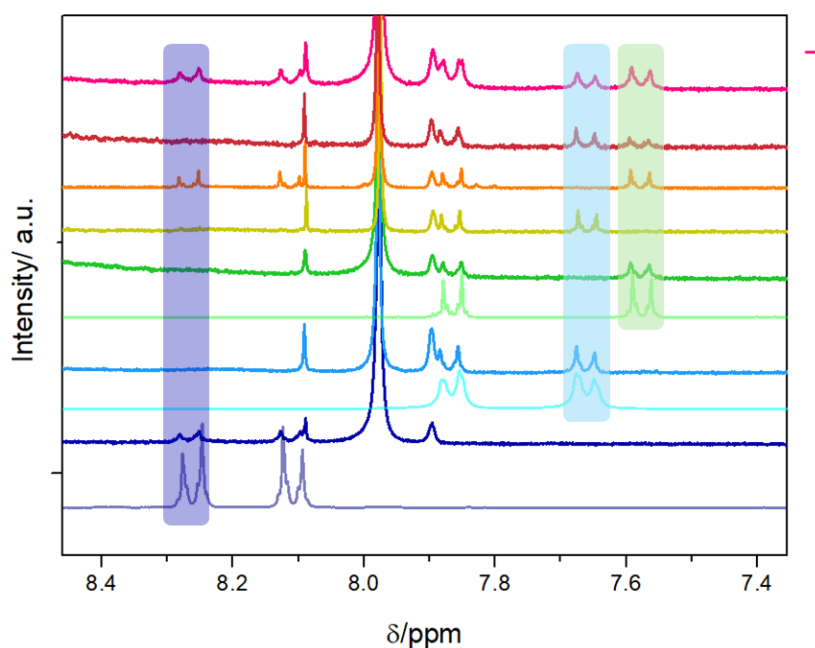

Figure S9: Amplification of ^{1}HNMR profiles acid-digested samples after dispersion centrifugation cycles, without 24 hours wash, compared to free modulators, showing the presence of modulators, formic acid, and DMF. The legend of Figure S8 applies to this figure. Dark blue Benz-NO$_2$, light blue Benz-SO$_3$ and green Benz-SH.

S.3.2.B. ^{1}H MNR of activated samples after24 hour methanol exchange
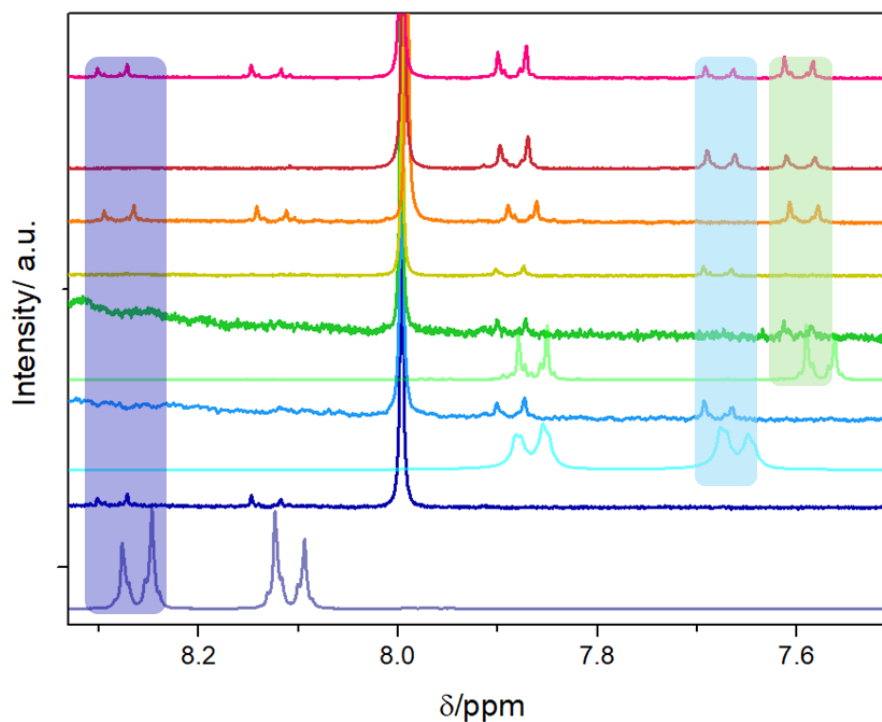
Figure S10: Amplification of ^{1}HNMR profiles acid-digested samples after stirring 24 hours in methanol (full activation protocol), compared to the free modulators, showing the presence of modulators and formic acid, and the absence of DMF. The legend of Figure S8 applies to this figure. Dark blue Benz-NO$_2$, light blue Benz-SO$_3$ and green Benz-SH.
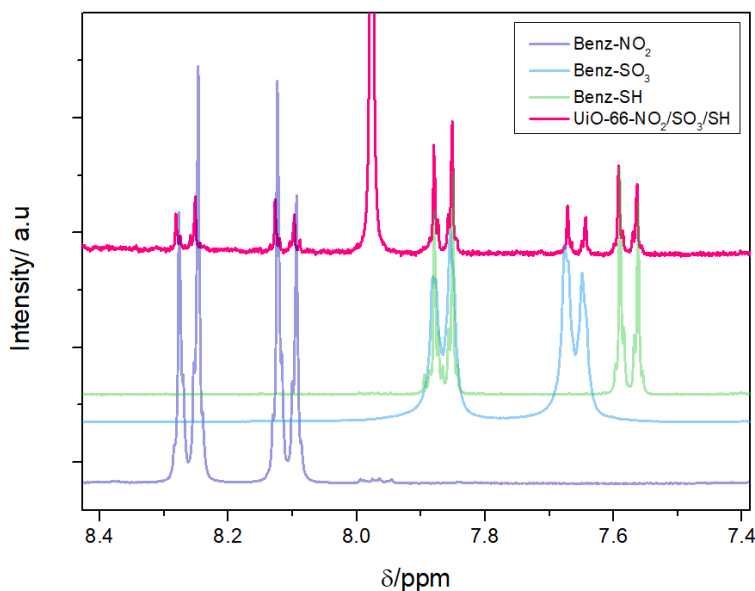

Figure S11: Amplification of ^{1}HNMR profiles acid-digested tri-modulated MOF after stirring 24 hours in methanol (full activation protocol), compared to the free modulators, showing the presence of modulators and formic acid, and the absence of DMF.

Table S2: Tabulated data extracted from acid-digested ^{1}HNMR of activated MTVM UiO-66 MOFs, expressed in molar ratio compared to the linker. Note that Bez-NO$_2$ cannot be effectively quantified in the UiO-66-NO$_2$/SO$_3$ sample.

Sample	NO$_2$/BDC	SO$_3$Na/BDC	SH/BDC	AcOH/BDC	FA/BDC
UiO-66-NO$_2$	0.072	n/a	n/a	0.001	0.101
UiO-66-SO$_3$	n/a	0.2	n/a	0.013	0.28
UiO-66-SH	n/a	n/a	0.041	0.029	0.141
UiO-66-NO$_2$/SO$_3$	<0.01	0.169	n/a	0.005	0.267
UiO-66-NO$_2$/SH	0.153	n/a	0.186	0.032	0.189
UiO-66-SO$_3$/SH	n/a	0.054	0.015	0.041	0.277
UiO-66-NO$_2$/SO$_3$/SH	0.169	0.054	0.115	0.024	0.202

Table S3: Tabulated data extracted from acid-digested ^{1}HNMR of activated MTVM UiO-66 MOFs, expressed in molar percent compared to the linker. Note that NO$_2$ cannot be quantified.

Sample	NO$_2$ mol%	SO$_3$Na mol%	SH mol%	AcOH mol%	FA mol%
UiO-66-NO$_2$	6.683	n/a	n/a	0.050	9.175
UiO-66-SO$_3$	n/a	16.667	n/a	1.316	21.875
UiO-66-SH	n/a	n/a	3.947	2.822	12.322
UiO-66-NO$_2$/SO$_3$	< 1	14.472	n/a	0.449	21.095
UiO-66-NO$_2$/SH	13.270	n/a	15.668	3.061	15.926
UiO-66-SO$_3$/SH	n/a	5.109	1.515	3.941	21.687
UiO-66-NO$_2$/SO$_3$/SH	14.430	5.120	10.287	2.306	16.830

Table S4: Tabulated data extracted from acid-digested ^{1}HNMR of activated MTVM UiO-66 MOFs, expressed in molar percent compared to the linker plus modulators. Note that NO$_2$ cannot be quantified.

Sample	NO$_2$mol%	SO$_3$Na mol%	SH mol%	Total mods%
UiO-66-NO$_2$	6.683	n/a	n/a	6.683
UiO-66-SO$_3$	n/a	16.667	n/a	16.667
UiO-66-SH	n/a	n/a	3.947	3.947
UiO-66-NO$_2$/SO$_3$	<0.01	14.472	0.000	14.472
UiO-66-NO$_2$/SH	11.429	n/a	13.878	25.306
UiO-66-SO$_3$/SH	0. n/a	5.036	1.439	6.475
UiO-66-NO$_2$/SO$_3$/SH	12.610	4.035	8.575	25.221

Table S5: Tabulated data extracted from acid-digested ^{1}HNMR of activated MTVM UiO-66 MOFs, expressed as the average and standard deviation of three samples, in molar ratio compared to the linker, showing similar incorporation trends.

Sample	NO$_2$	sd	SO$_3$Na	sd	SH	sd
UiO-66-NO$_2$	0.100	0.064				
UiO-66-SO$_3$			0.300	0.115		
UiO-66-SH					0.061	0.030
UiO-66-NO$_2$/SO$_3$	0.018	0.021	0.153	0.059		
UiO-66-NO$_2$/SH	0.151	0.058			0.221	0.088
UiO-66-SO$_3$/SH			0.335	0.206	0.265	0.181
UiO-66-NO$_2$/SO$_3$/SH	0.110	0.056	0.054	0.021	0.135	0.036
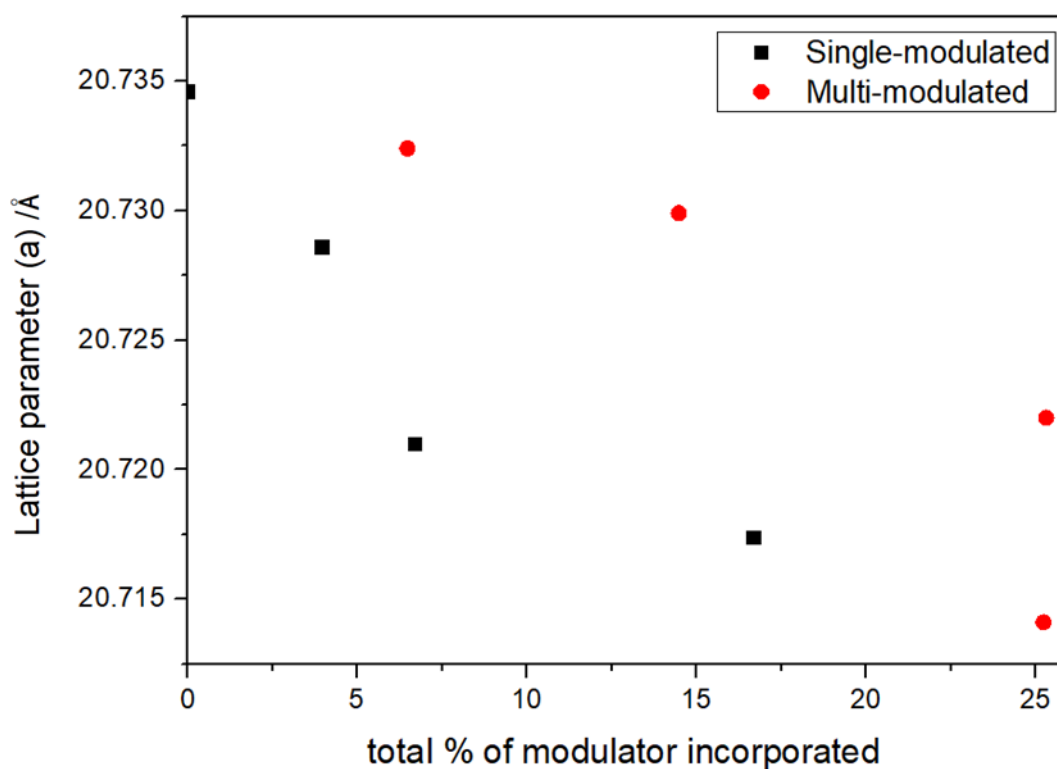
Figure S12: Variation in lattice parameter determined by Pawley refinements as a function of the total Benz-X modulators incorporated in molar percent, extracted from Table S4.

S.3.3 Fourier transformed Infra-Red (FT-IR)

In agreement with previous work on Benz-SO$_3$ modulation, UiO-66-SO$_3$ displayed new bands attributed to asymmetric and symmetric stretching frequencies of sulfonate, [6] at 1115 (ν_{as}SO$_3$), 1032 (ν_{as}SO$_3$) and 1010 (ν_sSO$_3$) cm^{-1}. These bands are shifted in comparison with the free modulator, due to the attachment (at least partial) of sulfonate groups to Zr clusters. A new band at 780 cm^{-1} (C-S stretching) is observed in the FT-IR spectra of S-containing-MOFs. The presence of NO$_2$ bands is masked by the MOF's signals but observed at 1527 cm^{-1} and 1340 cm^{-1}.
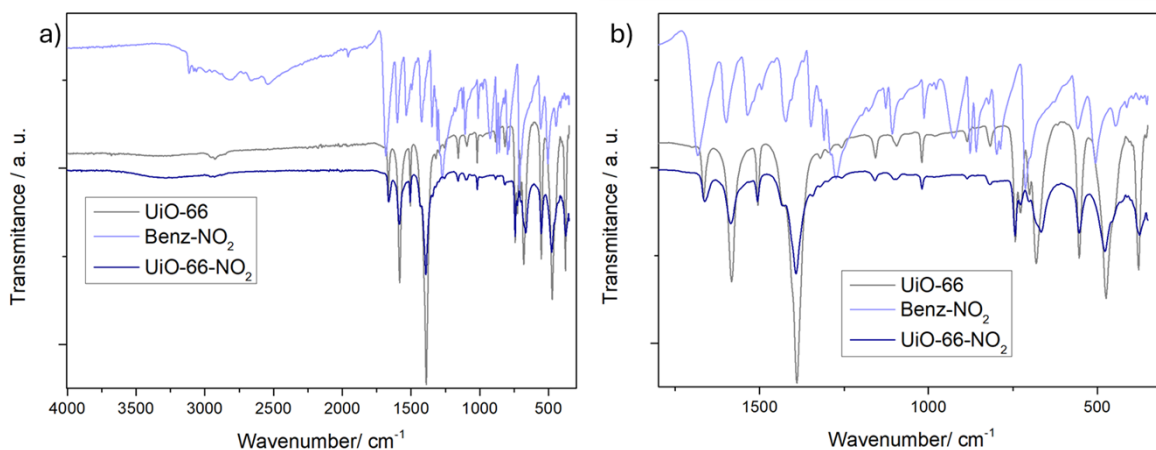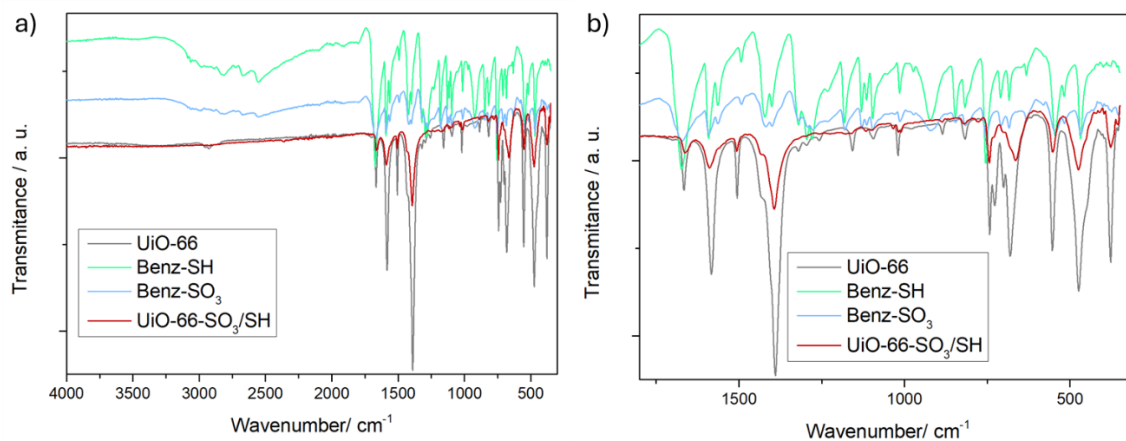

Figure S13: Raw FT-IR profiles of UiO-66-NO$_2$ compared to pristine UiO-66 and Benz-NO$_2$ modulator.
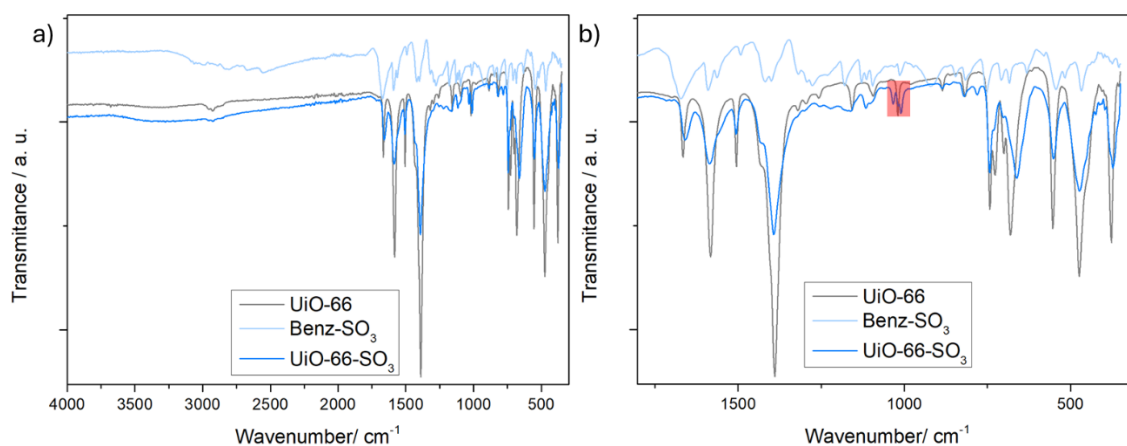
Figure S14: Raw FT-IR profiles of UiO-66-SO$_3$ compared to pristine UiO-66 and Benz-SO$_3$ modulator.
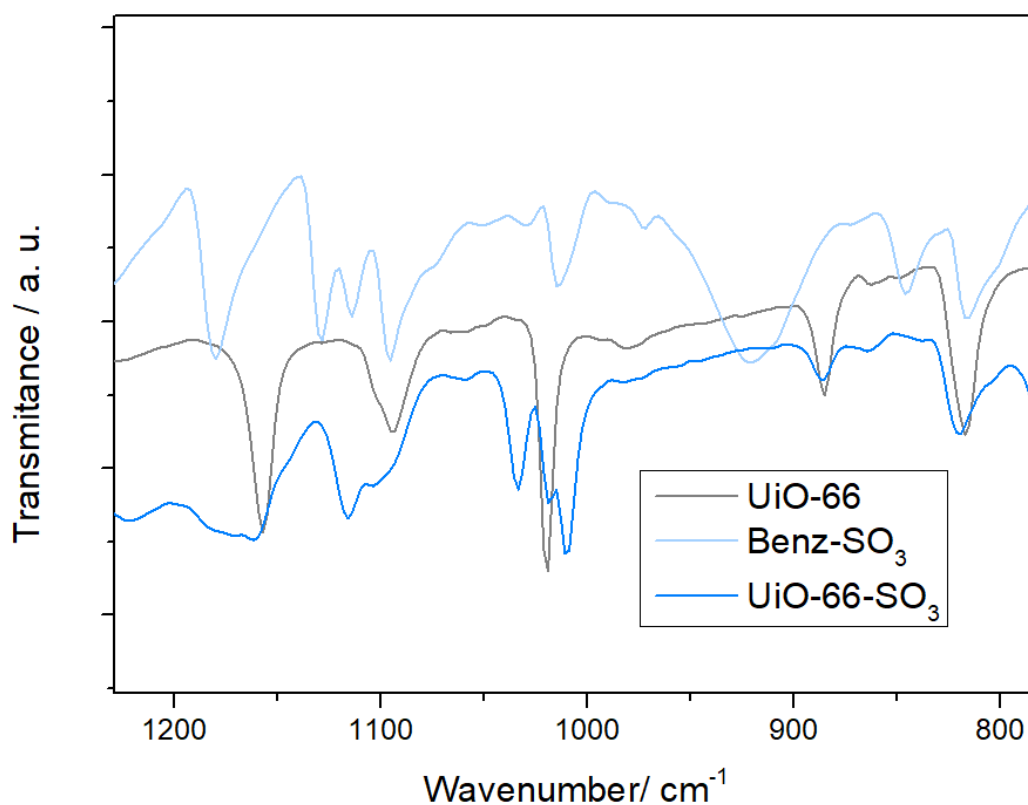
Figure S15: Amplification of the raw FT-IR profiles of UiO-66-SO$_3$ compared to pristine UiO-66 and Benz-SO$_3$ modulator, showing the shifting of SO$_3$ signals as a consequence of the attachment of sulfonate signals to Zr$_6$ units.
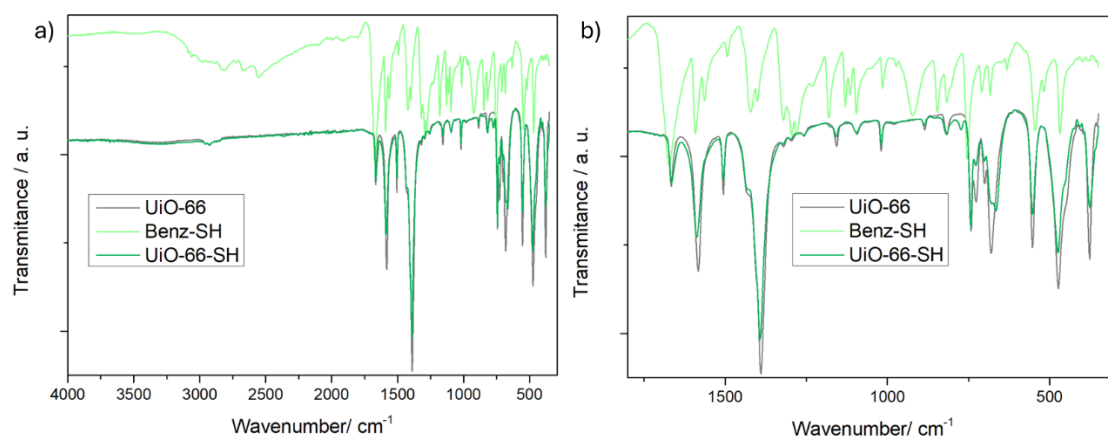
Figure S16: Raw FT-IR profiles of UiO-66-SH compared to pristine UiO-66 and Benz-SH modulator.
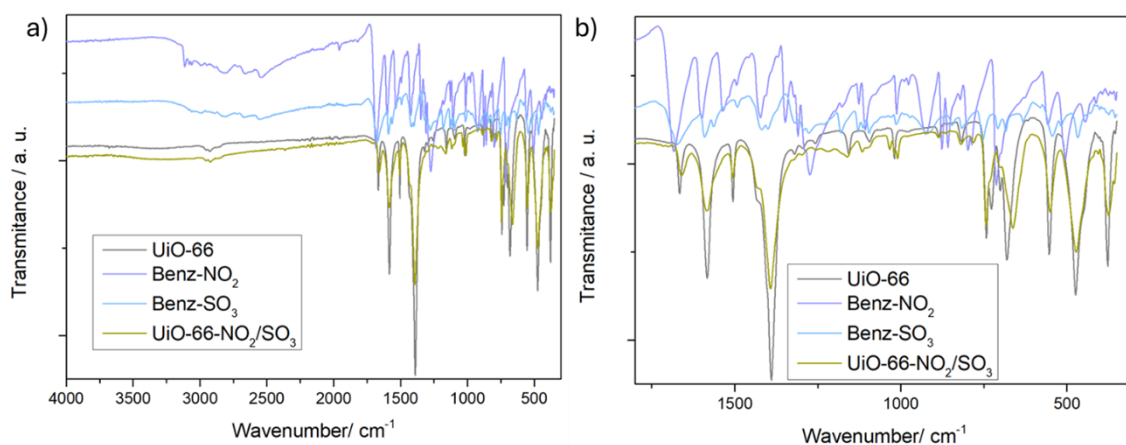
Figure S17: Raw FT-IR profiles of UiO-66-NO$_2$/SO$_3$ compared to pristine UiO-66, Benz-NO$_2$ and Benz-SO$_3$ modulators.
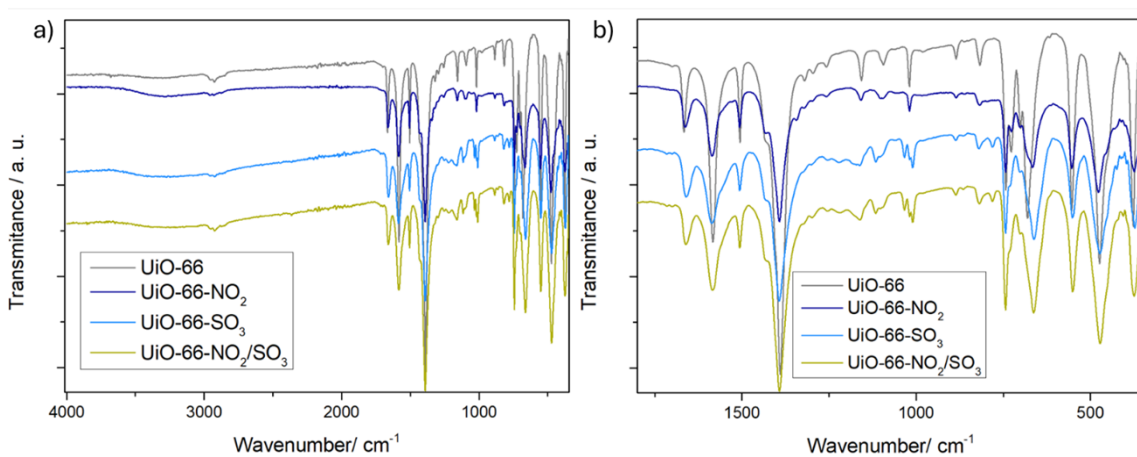
Figure S18: Raw FT-IR profiles of UiO-66-NO$_2$/SO$_3$ compared to pristine UiO-66, UiO-66-NO$_2$ and UiO-66-SO$_3$ single-modulated MOFs.
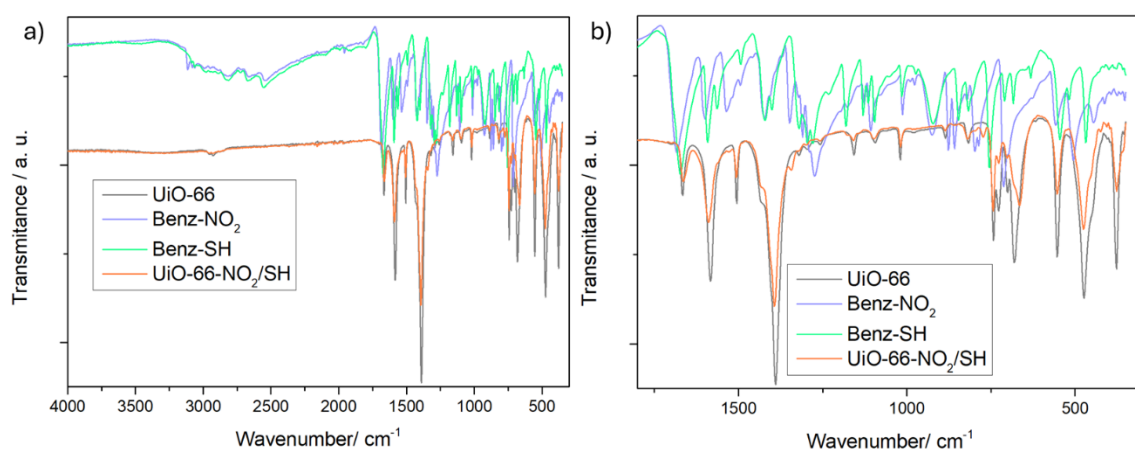
Figure S19: Raw FT-IR profiles of UiO-66-NO$_2$/SH compared to pristine UiO-66, Benz-NO$_2$ and Benz-SH modulators.
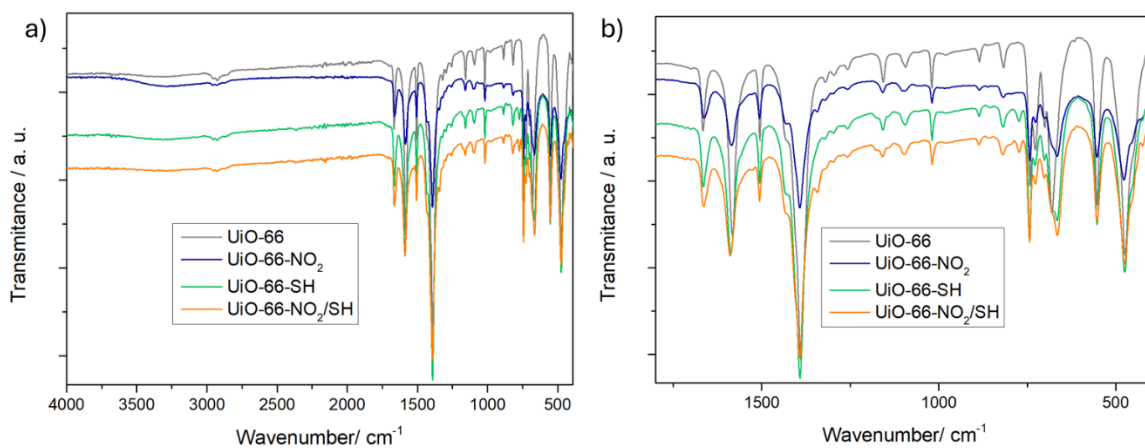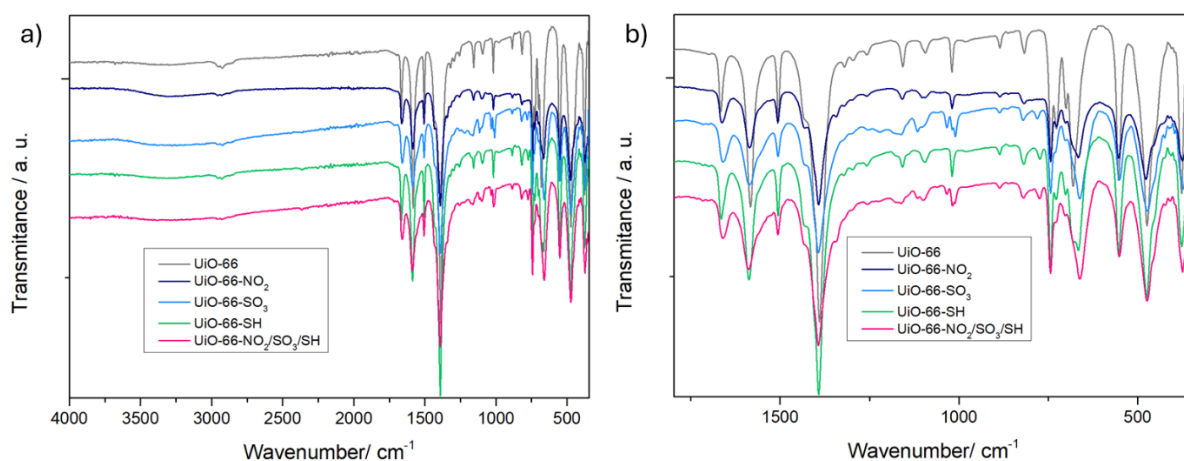
Figure S20: Raw FT-IR profiles of UiO-66-NO$_2$/SH compared to pristine UiO-66, UiO-66-NO$_2$ and UiO-66-SH single-modulated MOFs.

Figure S21: Raw FT-IR profiles of UiO-66-SO$_3$/SH compared to pristine UiO-66, Benz-SH and Benz-SO$_3$ modulators.
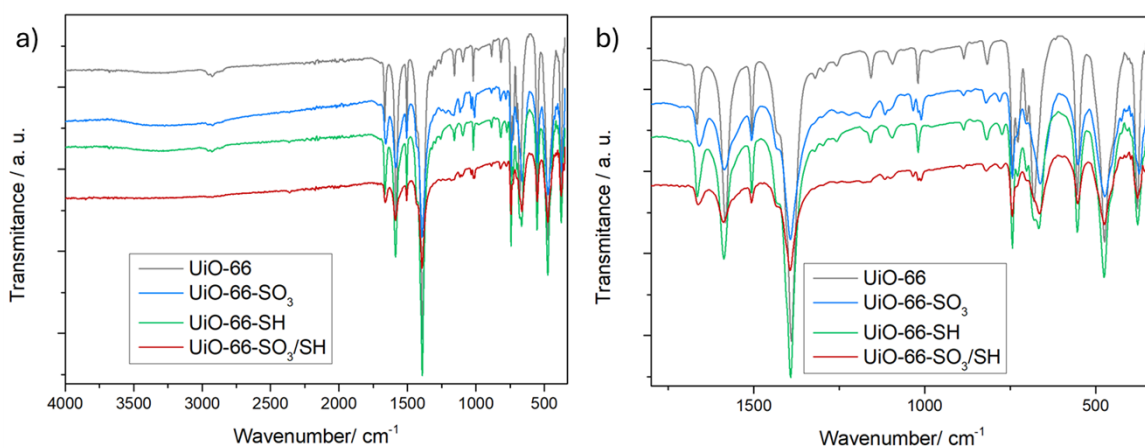
Figure S22: Raw FT-IR profiles of UiO-66-SO$_3$/SH compared to pristine UiO-66, UiO-66-SH and UiO-66-SH single-modulated MOFs.
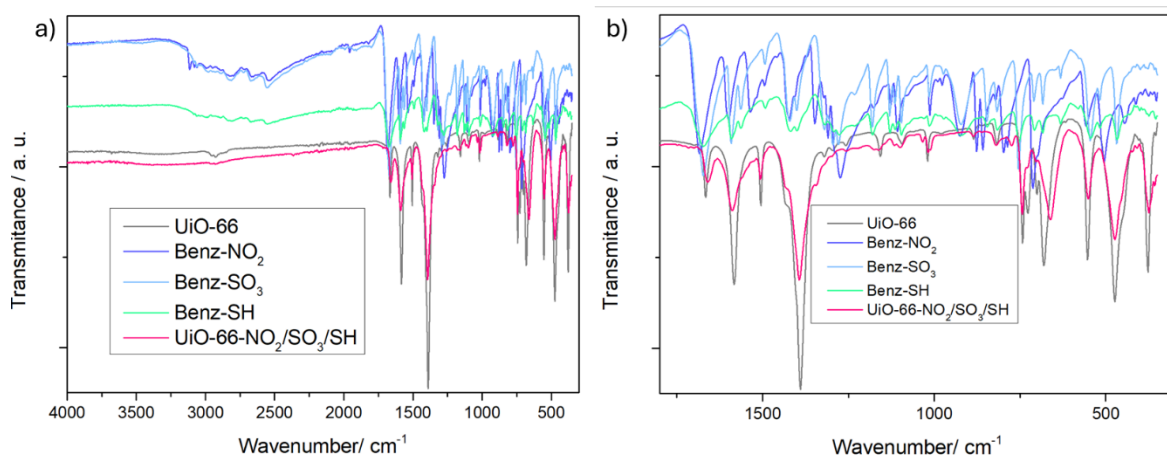
Figure S23: Raw FT-IR profiles of UiO-66-NO$_2$/SO$_3$/SH compared to pristine UiO-66, Benz-NO$_2$, Benz-SH and Benz-SO$_3$ modulators.

Figure S24: Raw FT-IR profiles of UiO-66-NO$_2$/SO$_3$/SH compared to pristine UiO-66, UiO-66-NO$_2$, UiO-66-SO$_3$ and UiO-66-SH single-modulated MOFs.
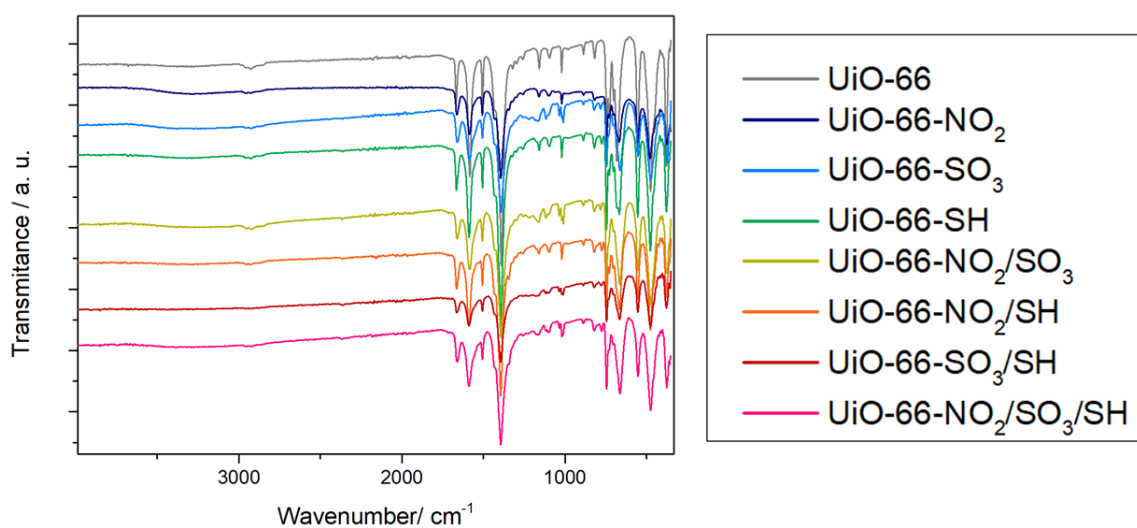
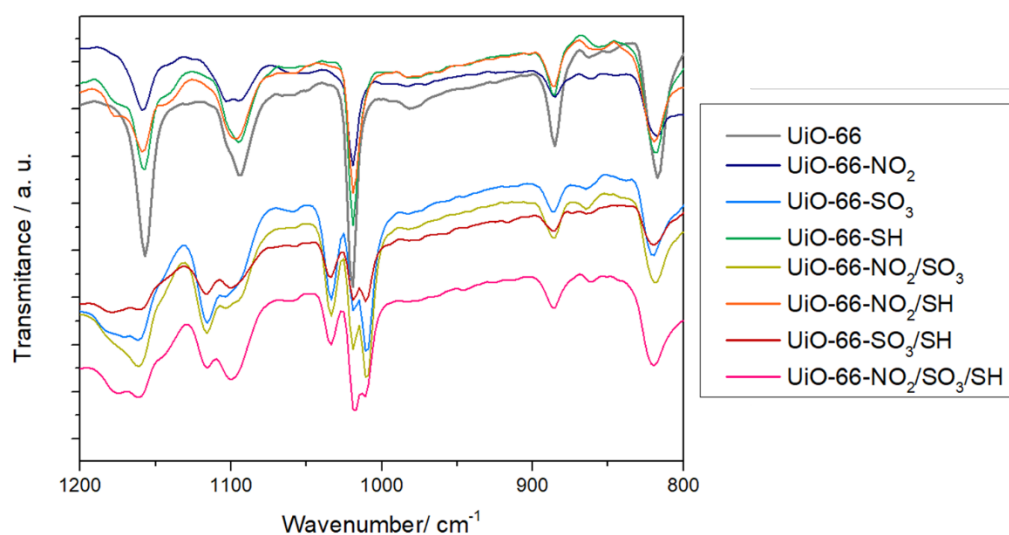**Figure S25:** Comparison of raw FT-IR profiles of single-modulated, tri-modulated and multimodulated samples.
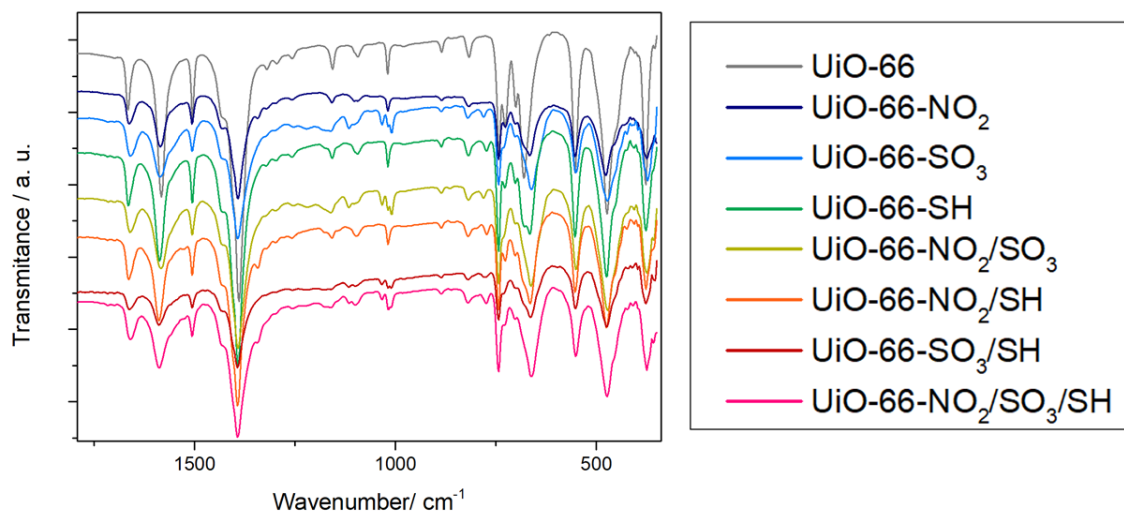
Figure S26: Comparison of amplified raw FT-IR profiles of single-modulated, tri-modulated, and multimodulated samples.

Figure S27: Comparison of amplified raw FT-IR profiles of single-modulated, tri-modulated, and multimodulated samples, highlighting the SO_3-containing samples, which display the same shifting in sulfonate signals as UiO-66-SO_3 due to the attachment of sulfonate groups to Zr_6 clusters.
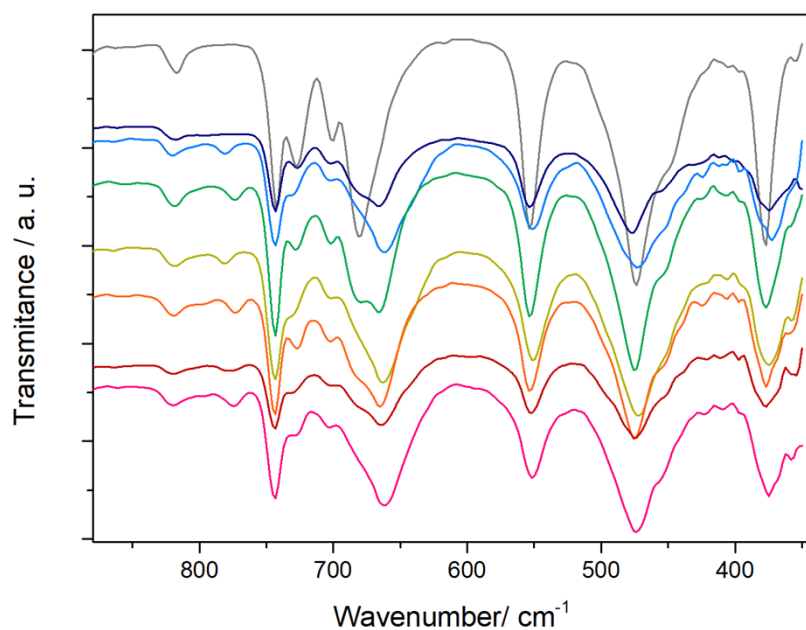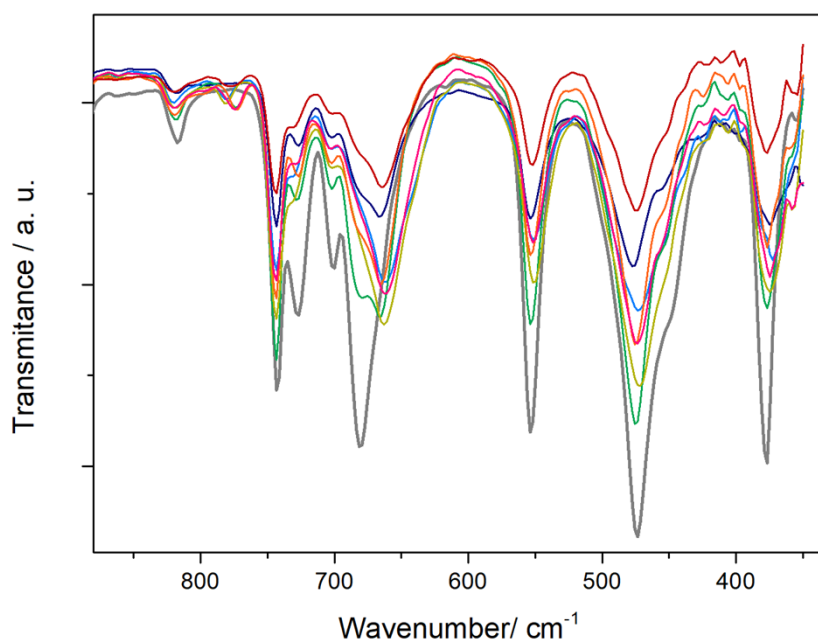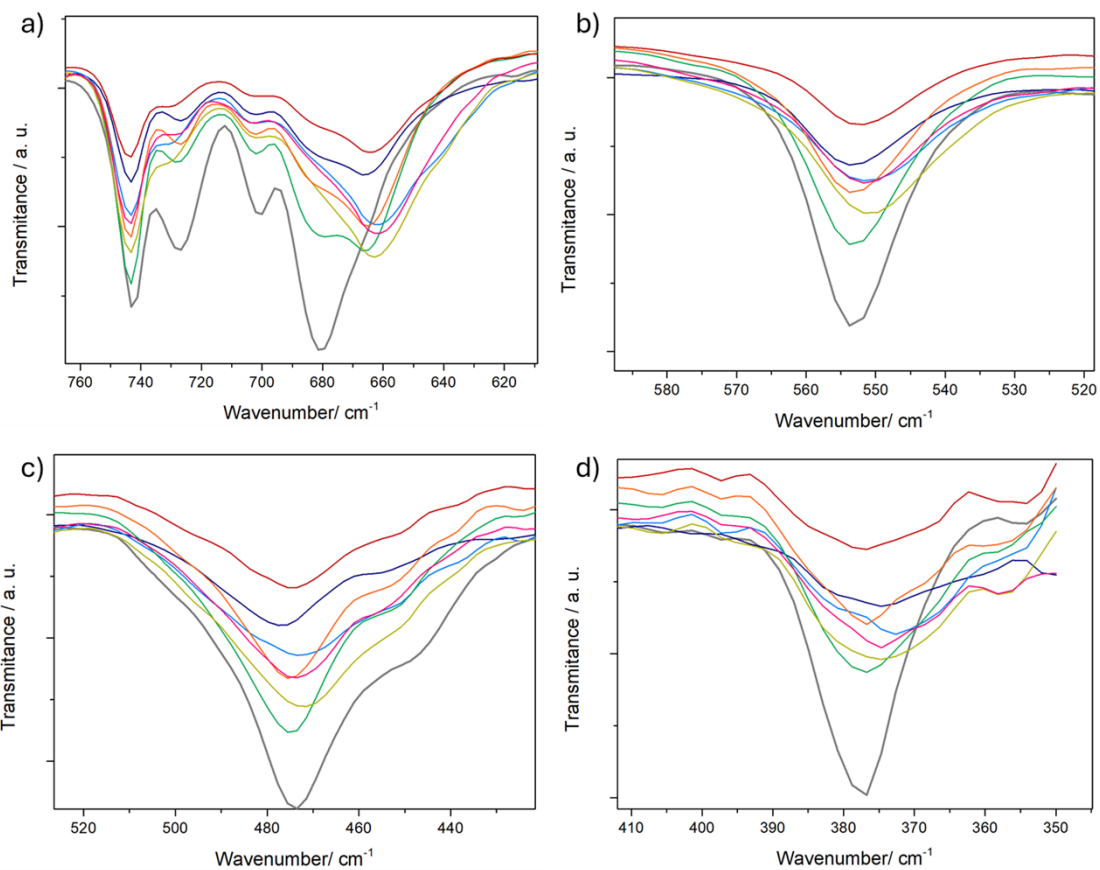
Figure S28: Comparison of amplified raw FT-IR profiles of single-modulated, tri-modulated and multimodulated samples, showing a general shifting in the signals between ca. 800 and 600cm^{-1}, attributed to μ_3-O stretching. [7] Labels from Figure S27 apply.

Figure S29: Comparison of amplified raw FT-IR profiles of single-modulated, tri-modulated and multimodulated samples, showing a general shifting in the signals between ca. 800 and 600cm^{-1}, attributed to μ_3-O stretching. [7] Labels from Figure S27 apply.

Figure S30: Comparison of amplified raw FT-IR profiles of single-modulated, tri-modulated and multimodulated samples, showing a general shifting in the signals a) attributed to μ_3-O stretching, b) attributed to Zr-(OC) stretching c) attributed to μ_3-OH stretching. [7] Labels from Figure S27 apply.

S.3.4 Thermogravimetric analysis (TGA)

We have estimated the composition of MTVM MUV-10 through the combination of TGA with molar ratios determined by ^{1}HNMR,[8] assuming that the modulators are incorporated into MUV-10 structure $\mathbf{Zr_6(O)_4(OH)_4(BDC)_X(Mod1)_y(Mod2)_z(FA)_A(AcOH)_B(OH/H_2O)_D}$ using previously reported methodology.[3] As Benzo-X decomposes during the decomposition range of BDC, the experimental ratio between the molecular weight of the dehydrated MOF (DH MOF) and its residue is expressed as follows for a dimodulated MOF, where Mod1 and Mod2 correspond to two different functionalised benzoic acid modulators.

$$(R_{expDH}) = \frac{M_w\,[DH\,MOF]}{M_w[Residue]} = \frac{M_w\,[ZrO(BDC)_x(Mod1)_y(Mod2)_z(O)_{\frac{(2-2x-y-z)}{2}}]}{M_w\,[ZrO_2]}$$

Since, $$y\,Mod1 = x\,BDC * \left(\frac{Mod1}{BDC}\right) NMR\,ratio$$

Then,

$$R_{expDH} = \frac{M_w\,[ZrO(BDC)_x(Mod1)_{Xnmr1}(Mod2)_{Xnmr2}(O)_{\frac{(2-2X-Xnmr1-Xnmr2)}{2}}]}{M_w\,[ZrO_2]}$$

$$XBTC$$

$$= \frac{(R_{expDH} * M_w\,[ZrO_2]) - M_w\,ZrO - M_w[O]}{M_w\,[BdC] + nmr1 * M_w[Mod1] + nmr2 * M_w[Mod2] - (1 + 1/2nmr1 + 1/2nmr2) *}$$

Once X (ligands, bdc) has been obtained,

$$y\,Mod1 = x\,BDC * \left(\frac{Mod1}{BDC}\right) NMR\,ratio1$$

$$zMod2 = x\,BDC * \left(\frac{Mod2}{BDC}\right) NMR\,ratio2$$

$$a\,Formate = number\,of\,BDC * \left(\frac{FA}{BDC}\right) NMR\,ratio$$

$$b\,acetate = number\,of\,BDC * \left(\frac{AcOH}{BDC}\right) NMR\,ratio$$

The number of OH/H_2O pairs needed to compensate for the charge can be calculated using the following equation, taking into account the charge of the different species:

$$4Zr = (4/6) * OH + (4/6) * O + 2XBdC + yMod1 + zMod2 + XNMRFA + XNMRAcOH + OH$$

Then $OH = 4 - 2XBDC - yMod1 - zMod2 - XNMRFA - ZNMR\,AcOH$

Please note that the same mathematical methodology is applied for single, di- and tri-modulated MOFs.

It is also worth mentioning, that although mathematically the method is exact, the assumptions will only lead to an estimation of the structure composition. For example, the difficulty of determining exactly the amount of Benz-SO_3 modulator bound to Zr_6 clusters led us to include this species as a monotopic modulator, thus providing an error in the OH species needed to compensate for the charge. The validity of the estimations can be evaluated through the calculations expressed in **Table S9.**
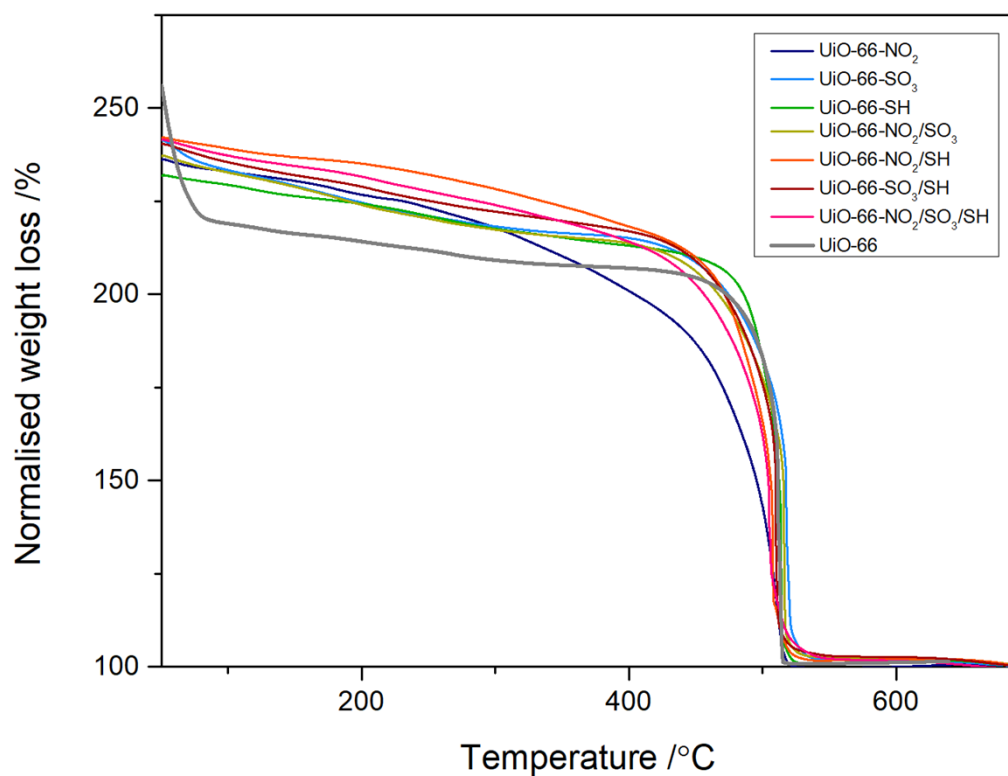
Figure S31: TGA profiles of the activated samples compared to pristine UiO-66, with the end of the decomposition profiles (residue) normalised to 100%.
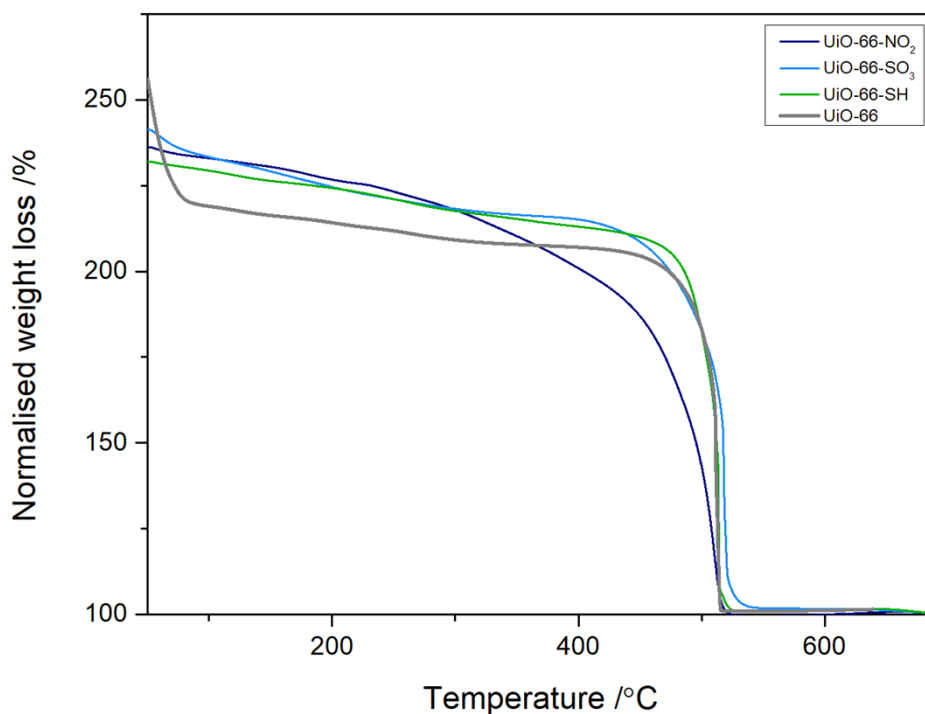

Figure S32: TGA profiles of the single-modulated samples compared to pristine UiO-66, with the end of the decomposition profiles (residue) normalised to 100%.
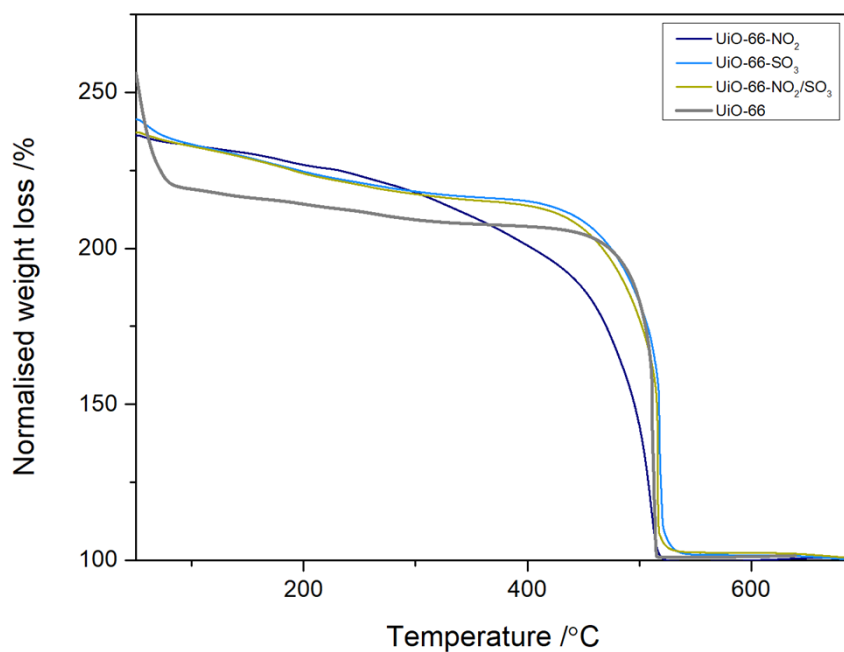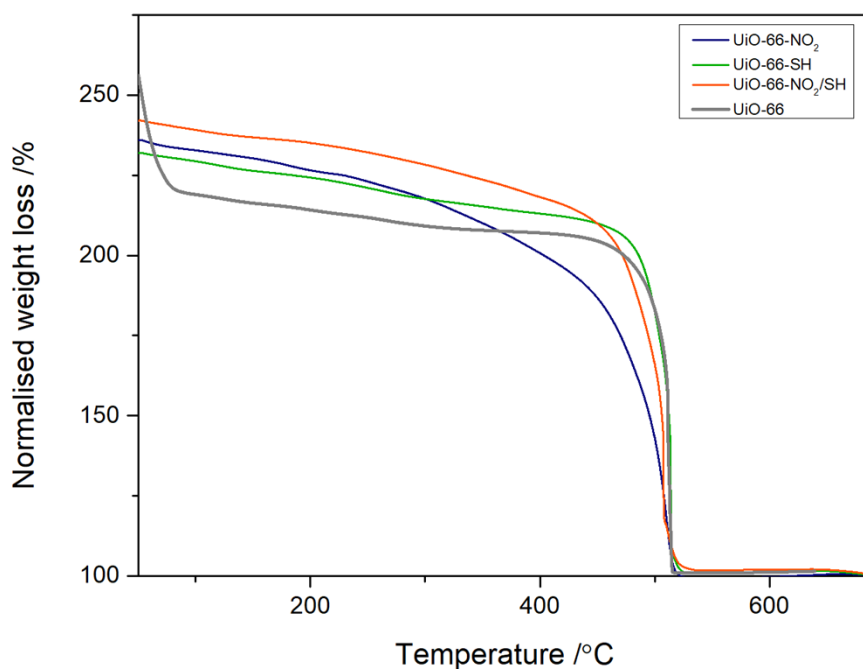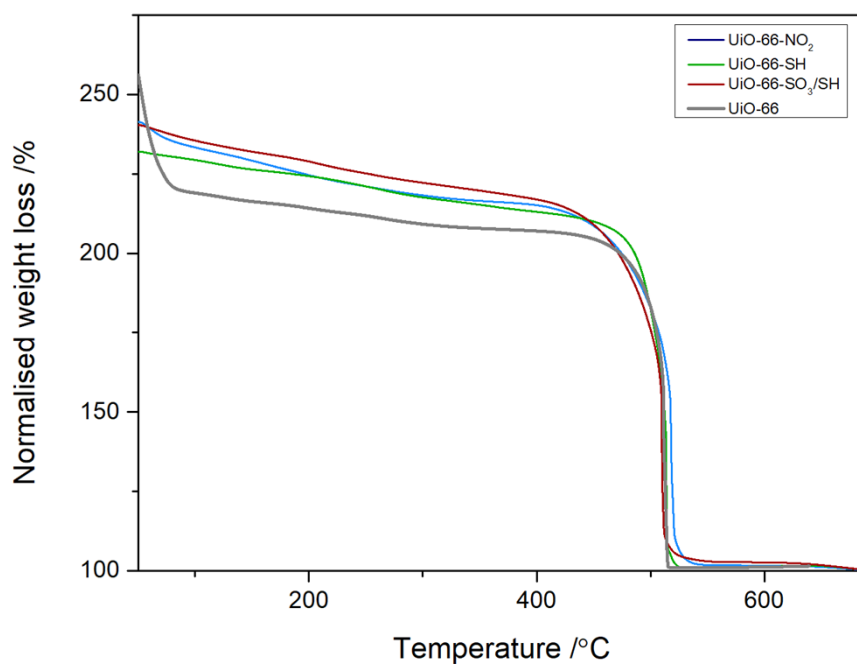
Figure S33: TGA profiles of the UiO-66-NO$_2$/SO$_3$ compared to pristine UiO-66 and equivalent single-modulated samples, with the end of the decomposition profiles (residue) normalised to 100%. The di-modulated sample shows a decomposition profile that stands between the decomposition temperatures of the single-modulated samples.
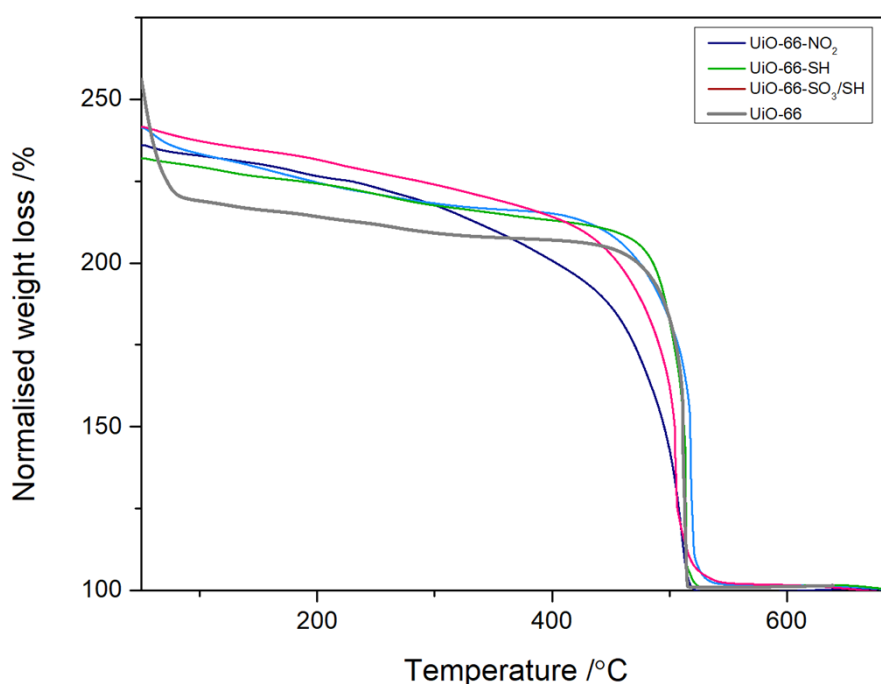

Figure S34: TGA profiles of the UiO-66-NO$_2$/SH compared to pristine UiO-66 and equivalent single-modulated samples, with the end of the decomposition profiles (residue) normalised to 100%. The di-modulated sample shows a decomposition profile that stands between the decomposition temperatures of the single-modulated samples.

Figure S35: TGA profiles of the UiO-66-SO$_3$/SH compared to pristine UiO-66 and equivalent single-modulated samples, with the end of the decomposition profiles (residue) normalised to 100%. The di-modulated sample shows a decomposition profile that stands between the decomposition temperatures of the single-modulated samples.

Figure S36: TGA profiles of the UiO-66-NO$_2$/SO$_3$/SH compared to pristine UiO-66 and single-modulated samples, with the end of the decomposition profiles (residue) normalised to 100%. The tri-modulated sample shows a decomposition profile that stands between the decomposition temperatures of the single-modulated samples.

Table S6: Data extracted from TGA analysis for the model framework $[Zr_6(O)_4(OH)_4(BDC)_X(Mod1)_Y(Mod2)_Z(Mod3)_W(FA)_A(AcOH)_B(OH/H_2O)_D]$.

	R_{expDH}	L	NO_2	SO_3	SH	AcOH	FA	OH/H_2O
UiO-66	2.07	0.89	n/a	n/a	n/a	0.083	0.071	0.066
UiO-66-NO₂	2.09	0.848	0.061	n/a	n/a	0	0.086	0.158
UiO-66-SO₃	2.13	0.751	n/a	0.15	0	0.01	0.21	0.127
UiO-66-SH	2.13	0.905	n/a	n/a	0.037	0.026	0.127	0
UiO-66-NO₂/SO₃	2.13	0.775	0	0.131	0	0.003	0.207	0.108
UiO-66-NO₂/SH	2.20	0.752	0.115	n/a	0.14	0.024	0.142	0.075
UiO-66-SO₃/SH	2.16	0.892	n/a	0.048	0.014	0.037	0.247	0
UiO-66-NO₂/SO₃/SH	2.22	0.755	0.127	0.041	0.087	0.018	0.153	0.066

Table S7: Data extracted from TGA analysis for the model framework $[Zr_6(O)_4(OH)_4(BDC)_X(Mod1)_Y(Mod2)_Z(Mod3)_W(FA)_A(AcOH)_B(OH/H_2O)_D]$.

	ML%	mod tot	ML	mod/ML	w/w % mods
UiO-66	10.998	0.000	0.110	n/a	n/a
UiO-66-NO₂	15.229	0.061	0.152	0.399	3.7
UiO-66-SO₃	24.889	0.150	0.249	0.604	10.8
UiO-66-SH	9.453	0.037	0.095	0.394	2.1
UiO-66-NO₂/SO₃	22.492	0.131	0.225	0.583	9.5
UiO-66-NO₂/SH	24.789	0.255	0.248	1.028	14.1
UiO-66-SO₃/SH	10.818	0.062	0.108	0.571	4.2
UiO-66-NO₂/SO₃/SH	24.547	0.254	0.245	1.037	14.7

Table S8: Data extracted from TGA analysis for the model framework $[Zr_6(O)_4(OH)_4(BDC)_X(Mod1)_Y(Mod2)_Z(Mod3)_W(FA)_A(AcOH)_B(OH/H_2O)_D]$.

	L	NO_2	SO_3	SH	AcOH	FA	OH/H_2O
UiO-66	5.340	n/a	n/a	n/a	0.498	0.427	0.395
UiO-66-NO₂	5.086	0.364	n/a	n/a	0.003	0.514	0.947
UiO-66-SO₃	4.507	n/a	0.901	n/a	0.060	1.262	0.763
UiO-66-SH	5.433	n/a	n/a	0.223	0.158	0.764	0
UiO-66-NO₂/SO₃Na	4.650	0.000	0.787	0.000	0.021	1.243	0.648
UiO-66-NO₂/SH	4.513	0.690	n/a	0.838	0.142	0.855	0.448
UiO-66-SO₃Na/SH	5.351	n/a	0.288	0.082	0.220	1.482	0
UiO-66-NO₂/SO₃/SH	4.527	0.763	0.244	0.519	0.107	0.916	0.396

Table S9: Experimental R_{exp} at the start of the decomposition profiles and calculated $R_{exptheo}$ based on the extracted molecular formulas, showing similar values that validate

the estimations performed, but highlighting that structural determination is not exact due to the complexity.

	Rexp	Rexp theo
UiO-66	2.18	2.19
UiO-66-NO$_2$	2.31	2.21
UiO-66-SO$_3$	2.30	2.28
UiO-66-SH	2.28	2.23
UiO-66-NO$_2$/SO$_3$Na	2.30	2.27
UiO-66-NO$_2$/SH	2.37	2.33
UiO-66-SO$_3$Na/SH	2.35	2.31
UiO-66-NO$_2$/SO$_3$/SH	2.36	2.35
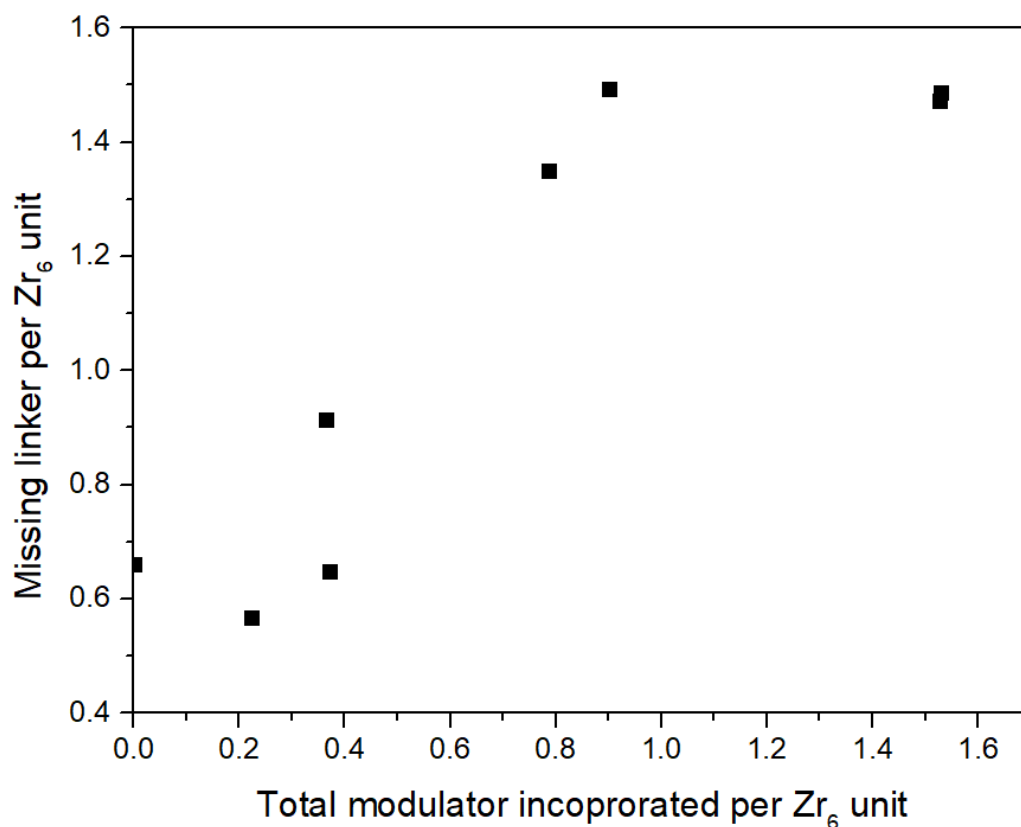
Figure S37: Relation between the total number of modulators incorporated and the missing linkers generated.
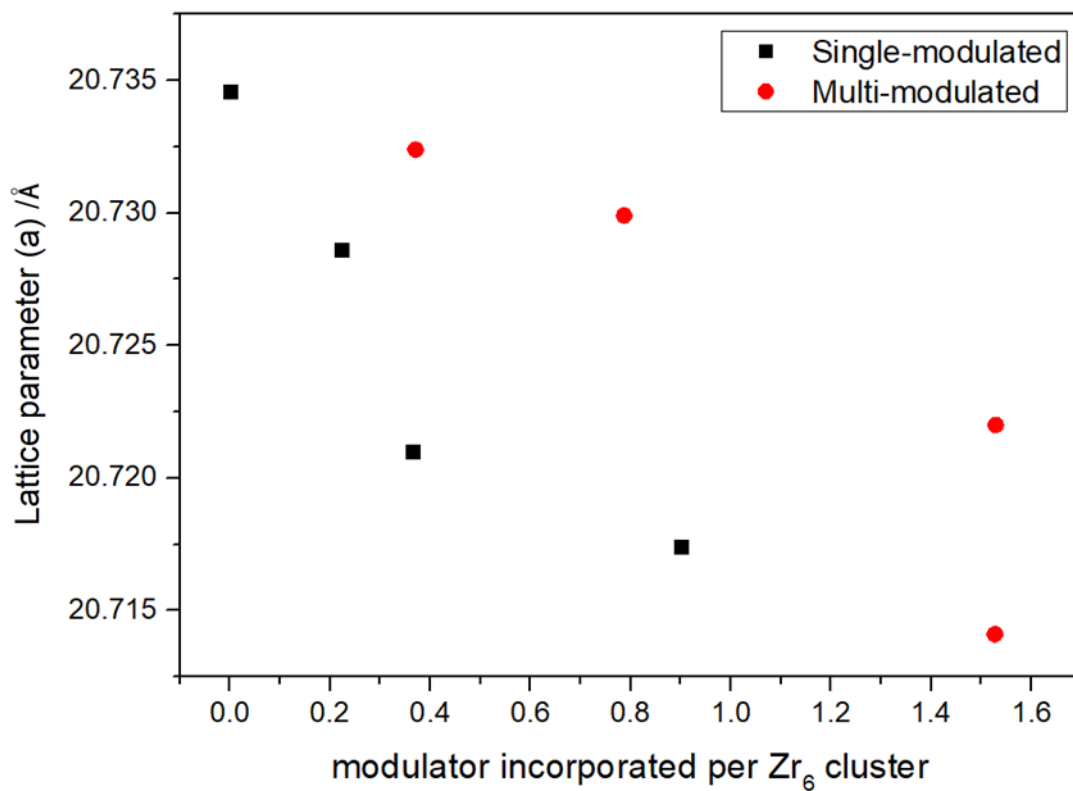
Figure S38: Variation in lattice parameter determined by Pawley refinements as a function of the total Benz-X modulators per Zr_6 incorporated, extracted from Table S7.

S.3.5 Pair Distribution function

I(Q) patterns of all MTVM-UiO-66 materials showed Bragg peaks (**Figure S39**), being consistent with the PXRD patterns. Structure factors, *S*(Q), (**Figure S40.a**) and pair distribution function (PDF), *D*(r), (**Figure S40.b**) were processed using GudrunX following well-documented procedures.[1,2]. Calculated total and partial PDFs (*g*(r)) were obtained using PDFGUI[3] from the optimized model of reported UiO-66 *fcu* (**Figure S41**).[3,4]
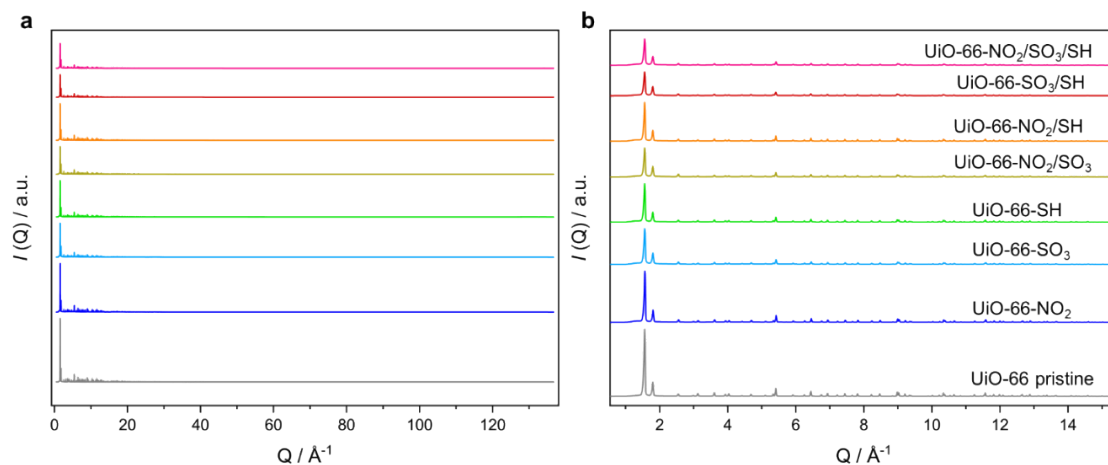
Figure S39. a. Experimental *I*(Q) for the pristine UiO-66 and their MTVM-UiO-66 derivatives. **b**. Zoom-in of the section 1.4-13.2 Å⁻¹.
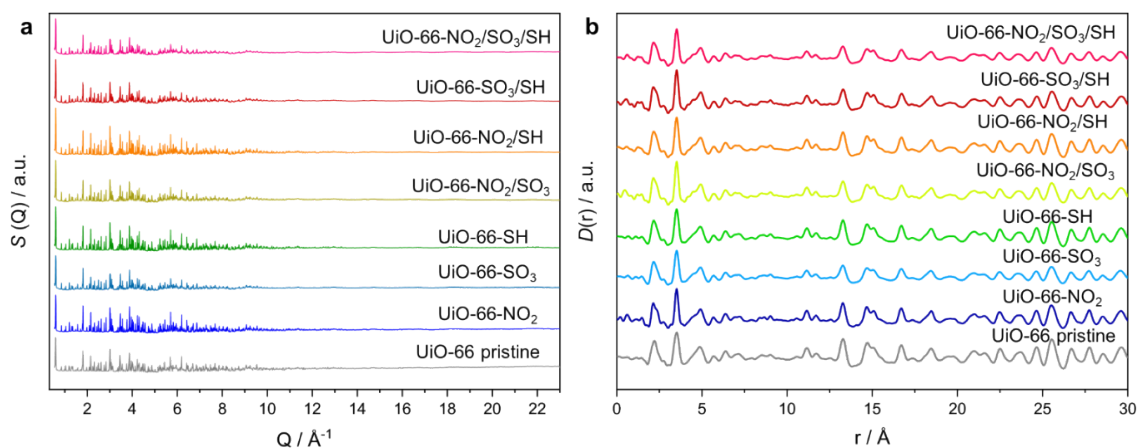
Figure S40. a. *S*(Q) of the pristine UiO-66 and their MTVM-UiO-66 derivatives. **b**. D(r) for the pristine UiO-66 and their MTVM-UiO-66 derivatives.
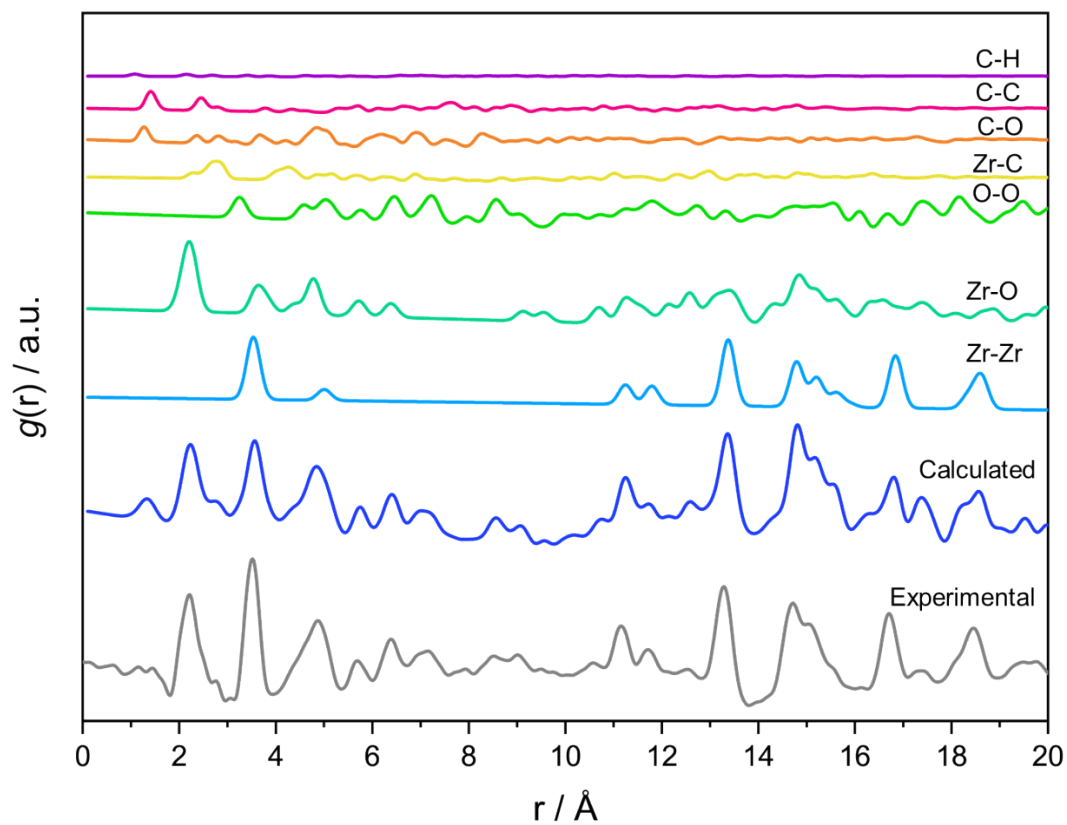
Figure S41. Calculated total and partial *g*(r)s using PDFGUI. A comparison of the calculated total PDF and the experimental one of the pristine UiO-66 is depicted showing similar correlations.
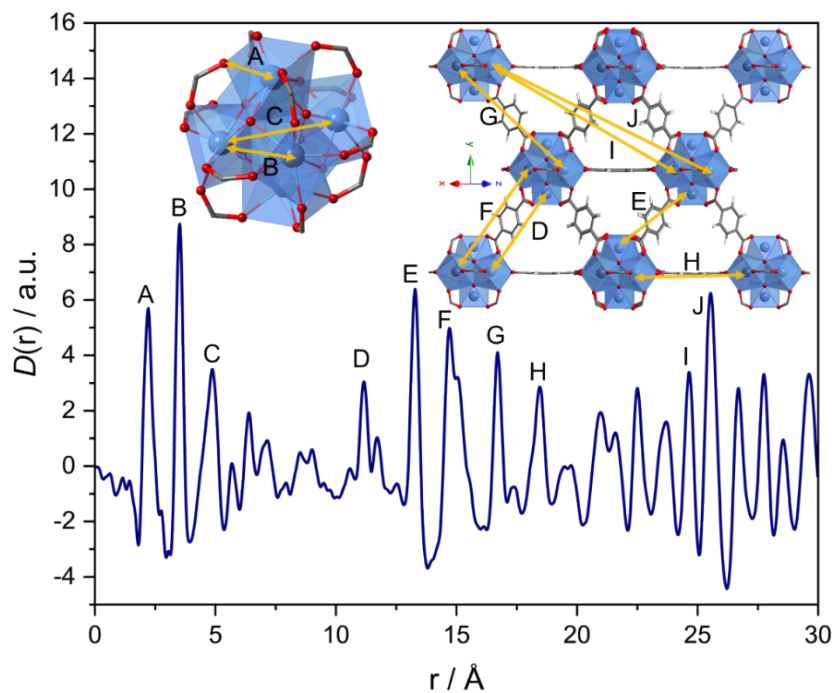
Figure S42. $D(r)$ of the pristine UiO-66 showing PDF peak assignment with letters (yellow arrows). Secondary building unit of the UiO-66 (Right up). 3-dimensional structure of the UiO-66 (Left up).
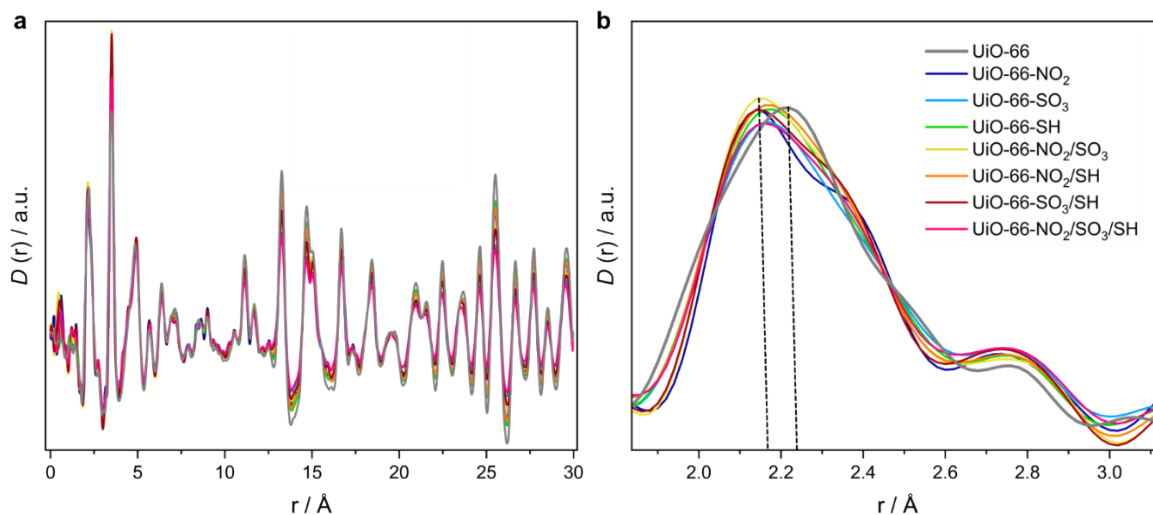
Figure S43. $D(r)$s of the pristine UiO-66 and MTV-UiO-66 materials. **a**. 0-30 Å range. **b**. 2.05-3.12 Å range showing the peak centred at 2.2 Å typical from Zr-O correlation.
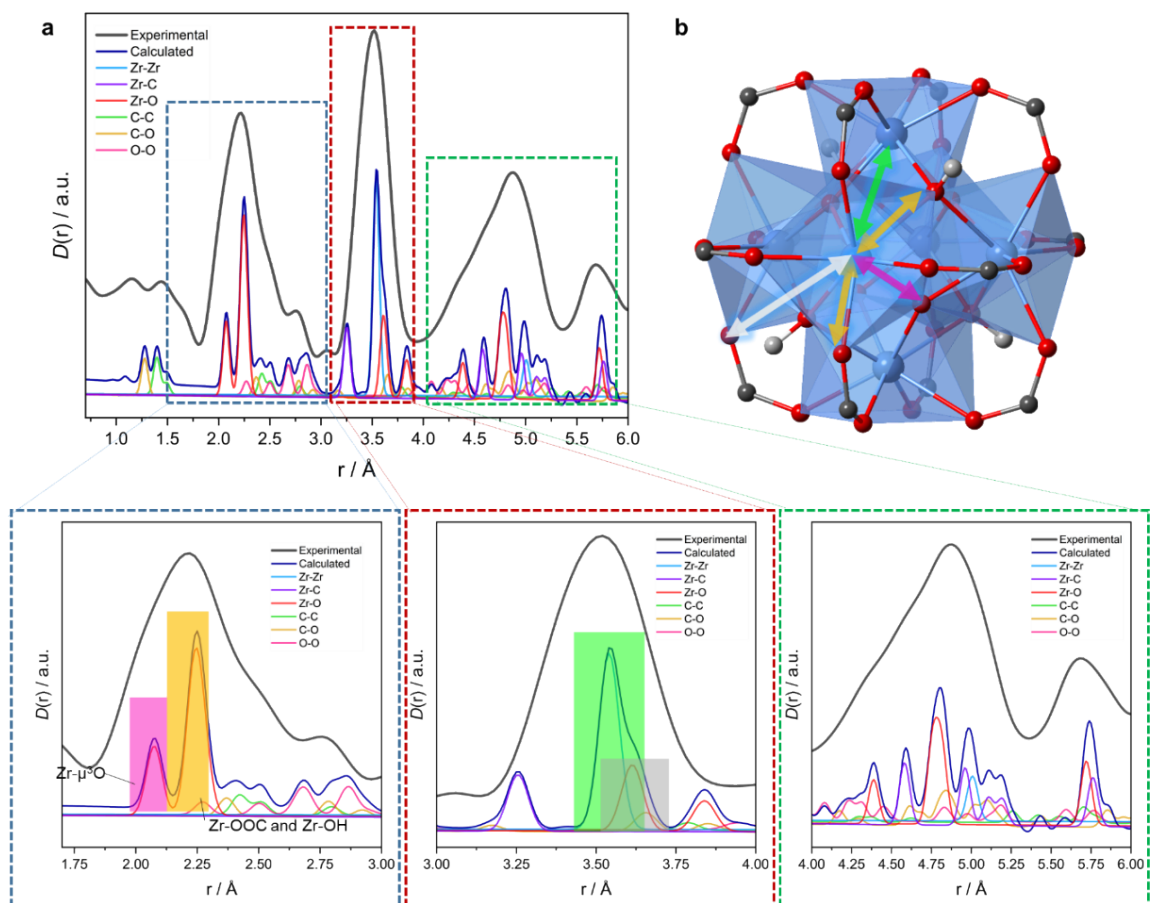
Figure S44. a. Comparison of the experimental $D(r)$ of the pristine UiO-66 with the calculated partial $g(r)$s using PDFGUI (ADP values are approached to 0.0005). Zoom-in of each dotted section appears more detailed below (pink: Zr-μ^3O, yellow: Zr-O_{COO}, green: Zr-Zr and light grey: Zr-O) **b**. Depiction of the Zr_6 secondary building unit. Coloured arrows indicate correlations depicted in Figure **a** Zr (blue), C (dark grey), O (red) and H (light grey).
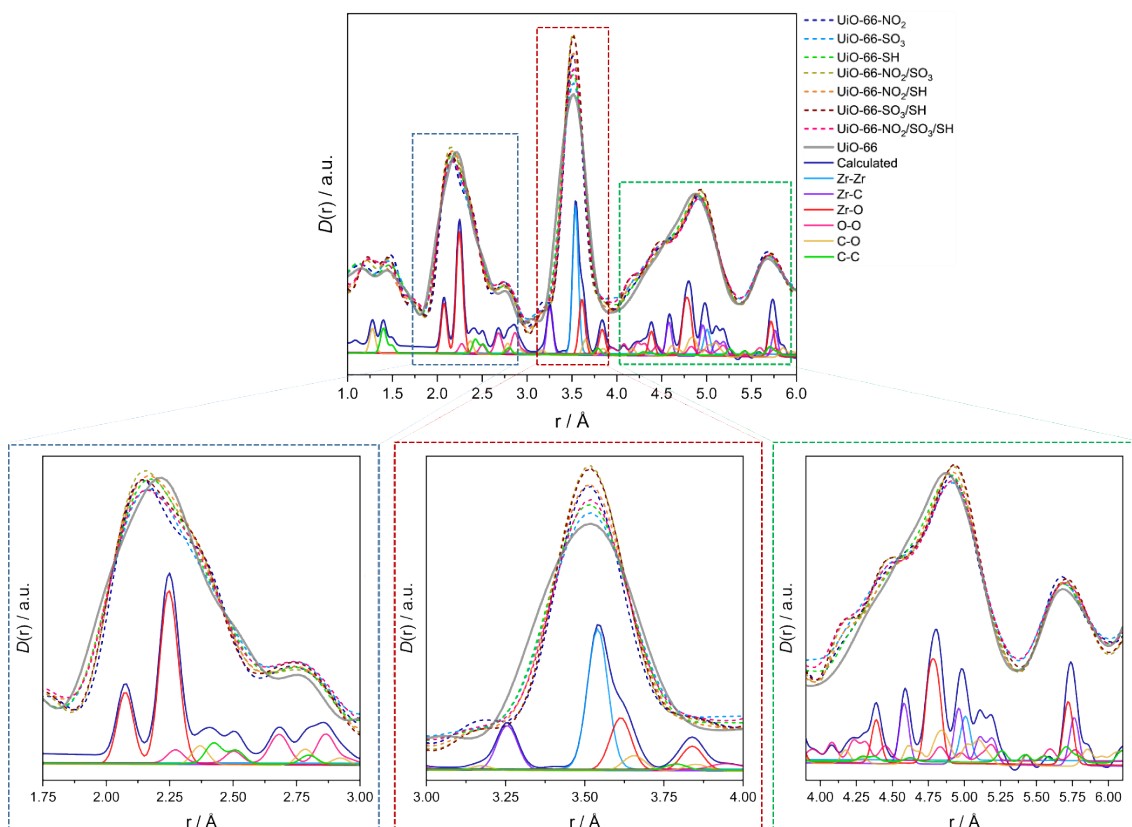
Figure S45. Comparison of the experimental $D(r)$ of the pristine UiO-66 and the MTVM materials with the calculated partial $g(r)$s using PDFGUI (ADP values are approached to 0.0005). Zoom-in of each dotted section appears more detailed.

Table S10. Fit report summary for peaks 1-4 of the $D(r)$s.

| Material	Peak 1		Peak 2		Peak 3		Peak 4	
	Position	Area	Position	Area	Position	Area	Position	Area
UiO-66 pristine	2.00447	0.511949	2.21205	2.85902	2.49615	0.861078	2.77485	0.317594
UiO-66-NO$_2$	2.04856	0.399326	2.15006	1.5699	2.36453	1.71121	2.74652	0.670269
UiO-66-SO$_3$	2.02814	0.321152	2.14629	1.36962	2.33986	2.20339	2.76893	0.438259
UiO-66-SH	2.03022	0.340153	2.14985	1.42222	2.33264	2.26944	2.76638	0.396603
UiO-66-NO$_2$/SO$_3$	2.03317	0.33667	2.13487	1.12788	2.3172	2.58364	2.76239	0.671091
UiO-66-NO$_2$/SH	2.03696	0.391749	2.14779	1.12506	2.31765	2.32673	2.75967	0.255029
UiO-66-SO$_3$/SH	2.02231	0.28417	2.1204	1.07916	2.31053	2.58607	2.752	0.756401
UiO-66-NO$_2$/SO$_3$/SH	2.02523	0.228462	2.12539	0.889846	2.29988	2.5479	2.75895	0.540739
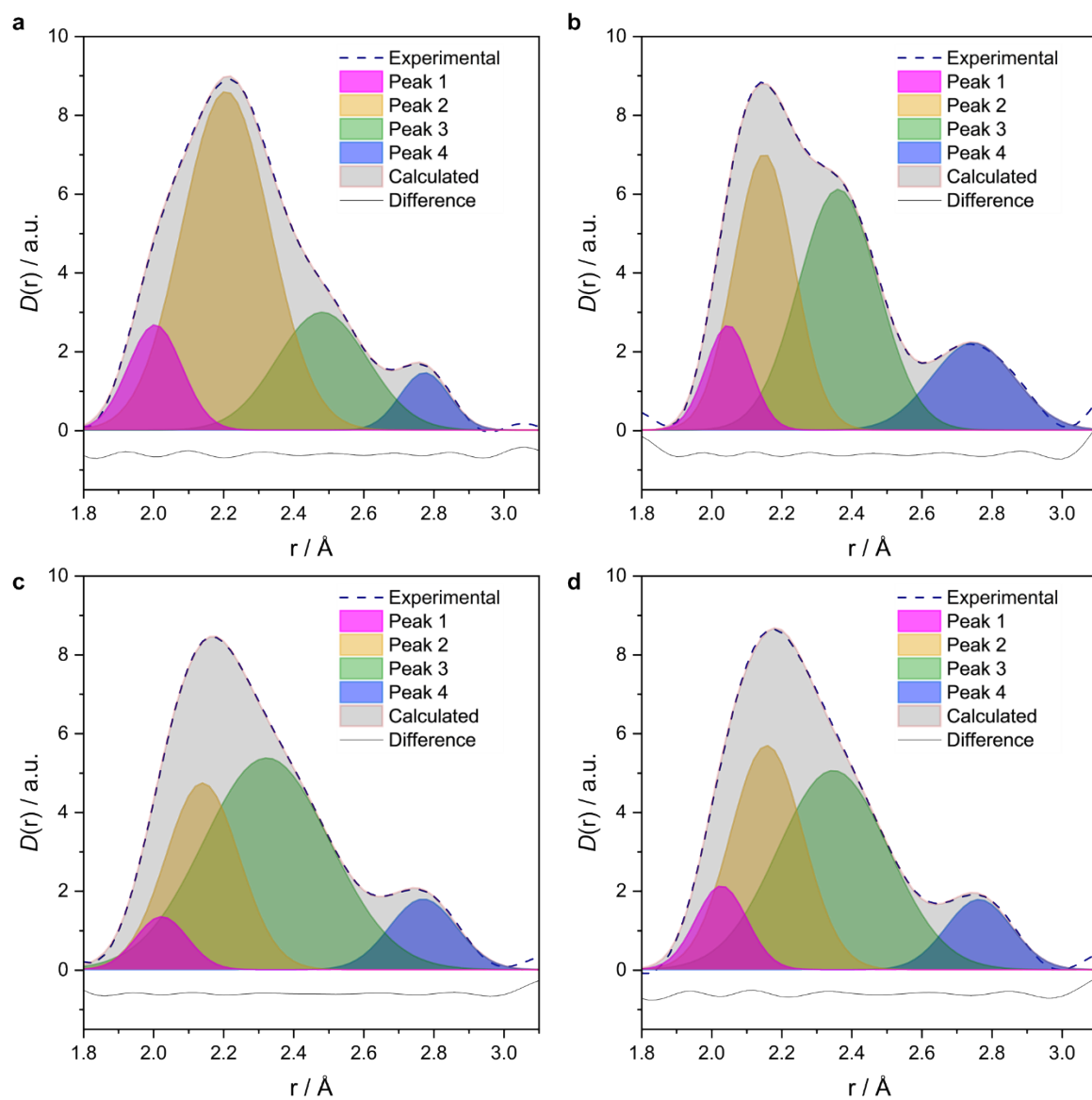
Figure S46. Representative curve fitting for the peaks centred at 2.2 and 2.8 Å for the $D(r)$s of **a**. Pristine UiO-66, **b**. UiO-66-NO$_2$, **c**. UiO-66-SO$_3$ and **d**. UiO-66-SH.
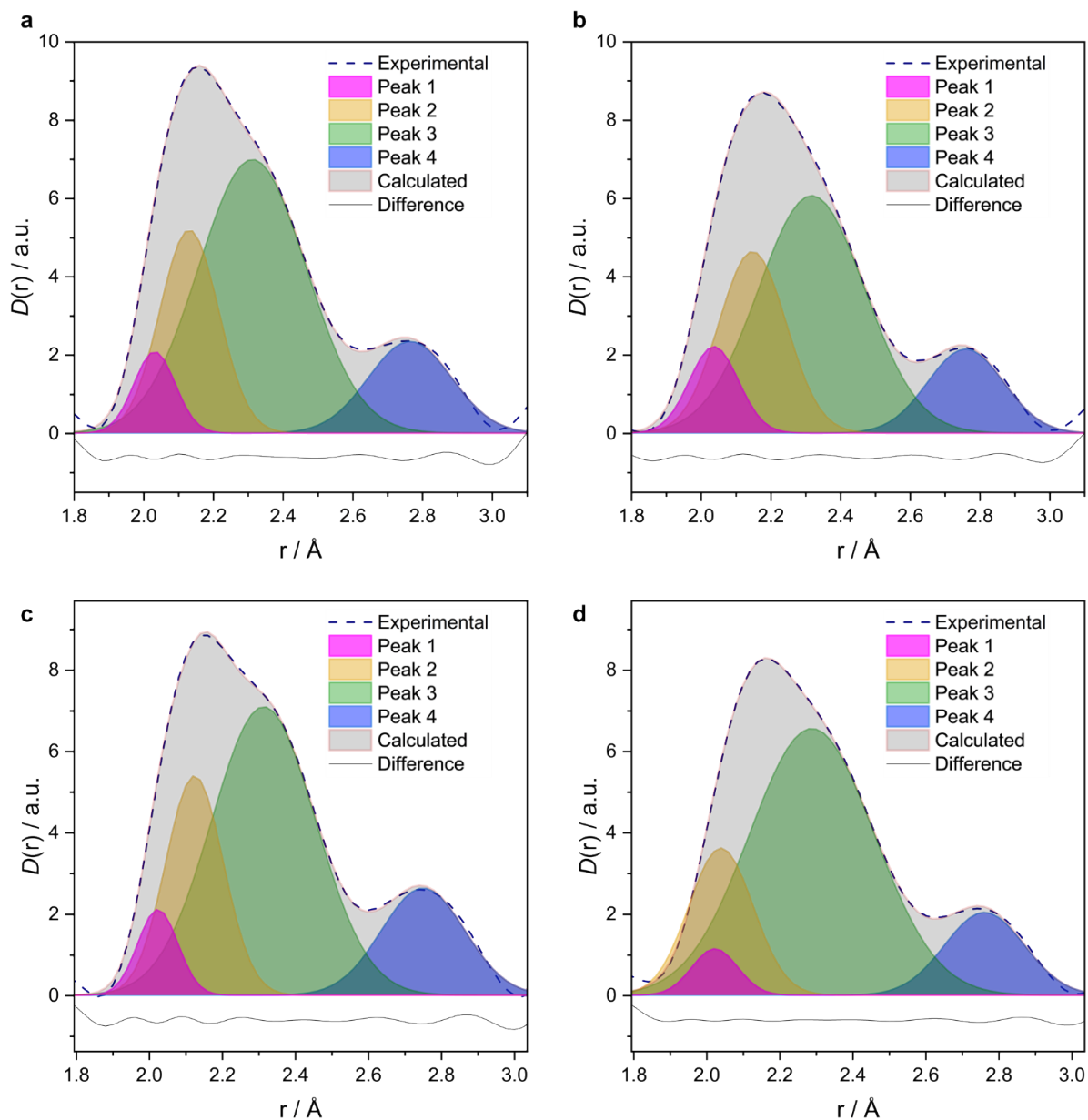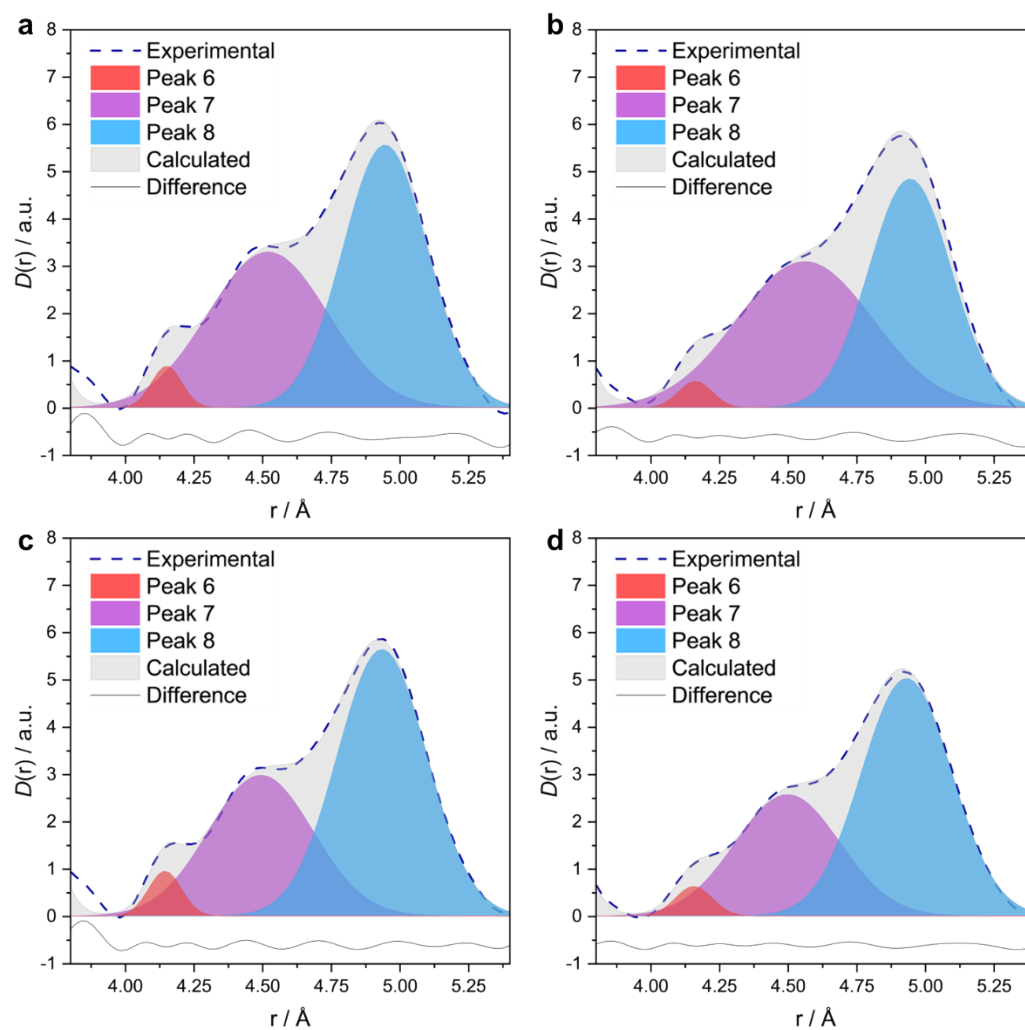
Figure S47. Representative curve fitting for the peaks centred at 2.2 and 2.8 Å for the D(r)s of **a**. UiO-66-NO$_2$/SO$_3$, **b**. UiO-66-NO$_2$/SH, **c**. UiO-66-SO$_3$/SH and **d**. UiO-66-NO$_2$/SO$_3$/SH.

Table S11. Fit report summary for peak centred at 3.5 Å

Material	Peak 5		
	Position	Height	Area
UiO-66 pristine	3.54799	11.1401	3.2140
UiO-66-NO$_2$	3.5200	13.6578	3.4892
UiO-66-SO$_3$	3.5200	11.2865	3.3639
UiO-66-SH	3.5082	12.7611	3.8321
UiO-66-NO$_2$/SO$_3$	3.5200	15.2453	4.21932
UiO-66-NO$_2$/SH	3.51228	13.8970	4.12513
UiO-66-SO$_3$/SH	3.5200	15.1610	4.19598
UiO-66-NO$_2$/SO$_3$/SH	3.51396	12.7296	3.73921
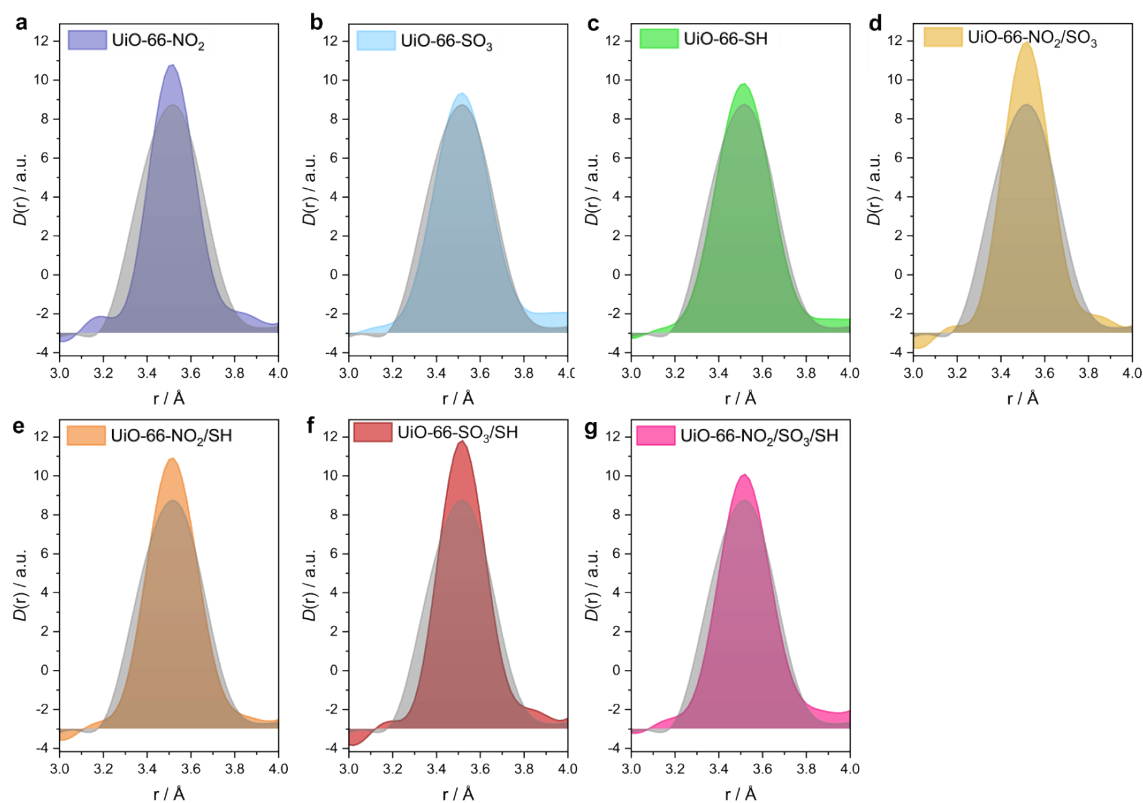
Figure S48. Integrated areas of the peak 5 centred at 3.54 Å from D(r) pattern of UiO-66 pristine (grey) and **a**. UiO-66-NO$_2$, **b**. UiO-66-SO$_3$, **c**. UiO-66-SH, **d**. UiO-66-NO$_2$/SO$_3$, **e**. UiO-66-NO$_2$/SH, **f**. UiO-66-SO$_3$/SH and **g**. UiO-66-NO$_2$/SO$_3$/SH.
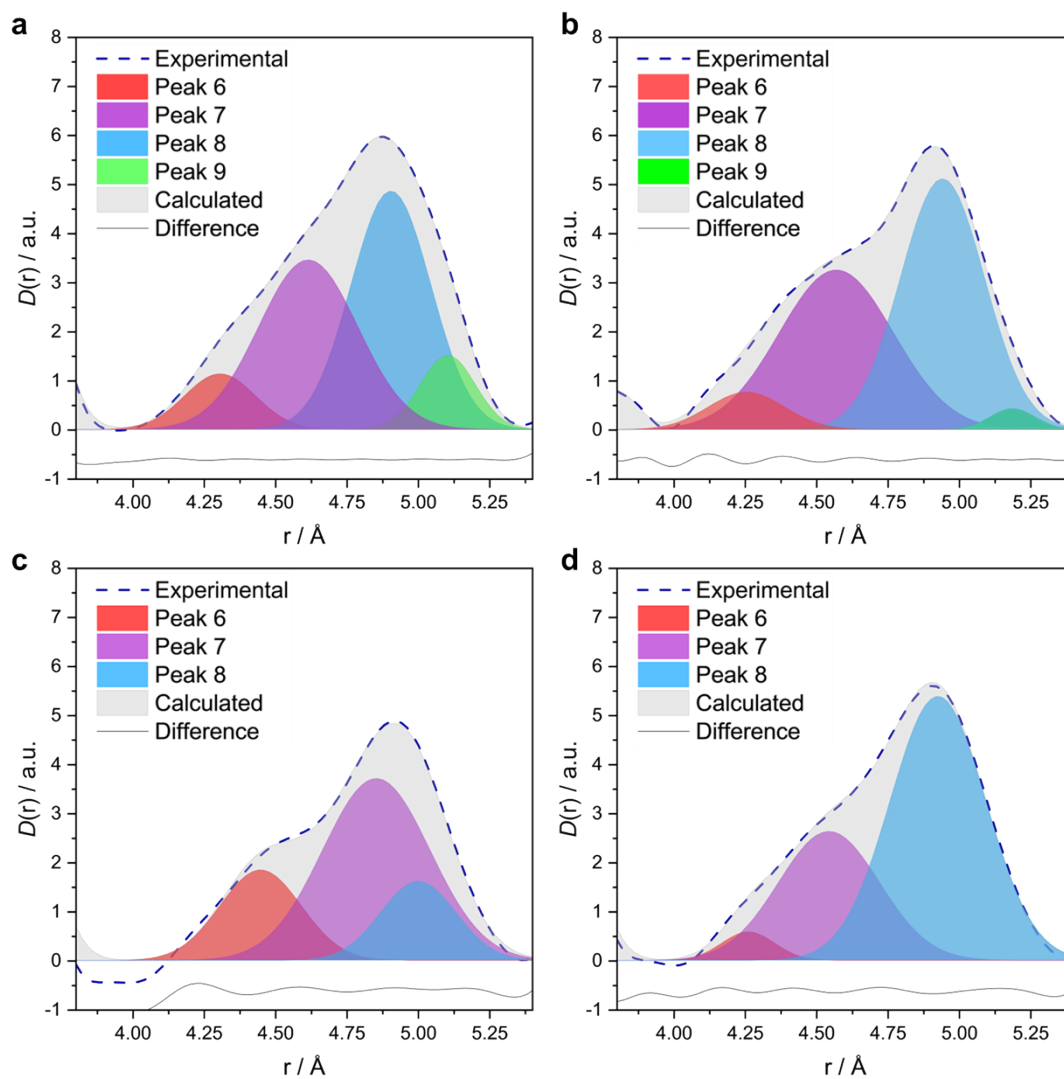
Figure S49. Representative curve fitting for the peaks centred at 4.1-5.2 Å for the $D(r)$s of **a**. Pristine UiO-66, **b**. UiO-66-NO$_2$, **c**. UiO-66-SO$_3$ and **d**. UiO-66-SH.

Figure S50. Representative curve fitting for the peaks centred at 4.1-5.2 Å for the $D(r)$s of **a**. UiO-66-NO$_2$/SO$_3$, **b**. UiO-66-NO$_2$/SH, **c**. UiO-66-SO$_3$/SH and **d**. UiO-66-NO$_2$/SO$_3$/SH.
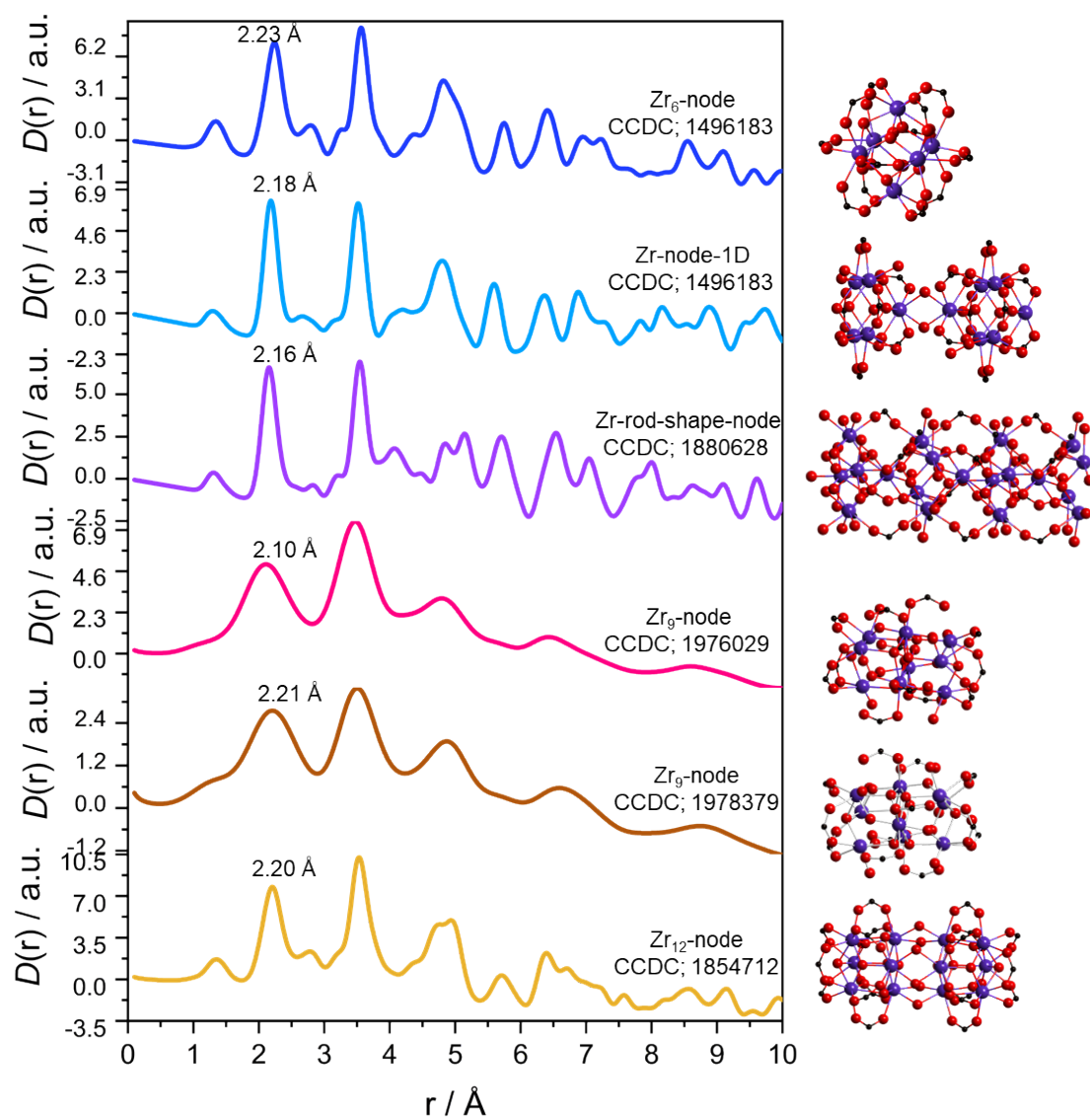
Figure S51. Calculated PDFs for Zr-clusters having different Zr-atom numbers.

Plot axis labels and annotations:

- y-axes (top to bottom): $D(r)$ / a.u.

Zr₆-node: peak at 2.23 Å; CCDC; 1496183
Zr-node-1D: peak at 2.18 Å; CCDC; 1496183
Zr-rod-shape-node: peak at 2.16 Å; CCDC; 1880628
Zr₉-node: peak at 2.10 Å; CCDC; 1976029
Zr₉-node: peak at 2.21 Å; CCDC; 1978379
Zr₁₂-node: peak at 2.20 Å; CCDC; 1854712

x-axis: r / Å

S.3.6 Scanning Electron Microscopy (SEM)
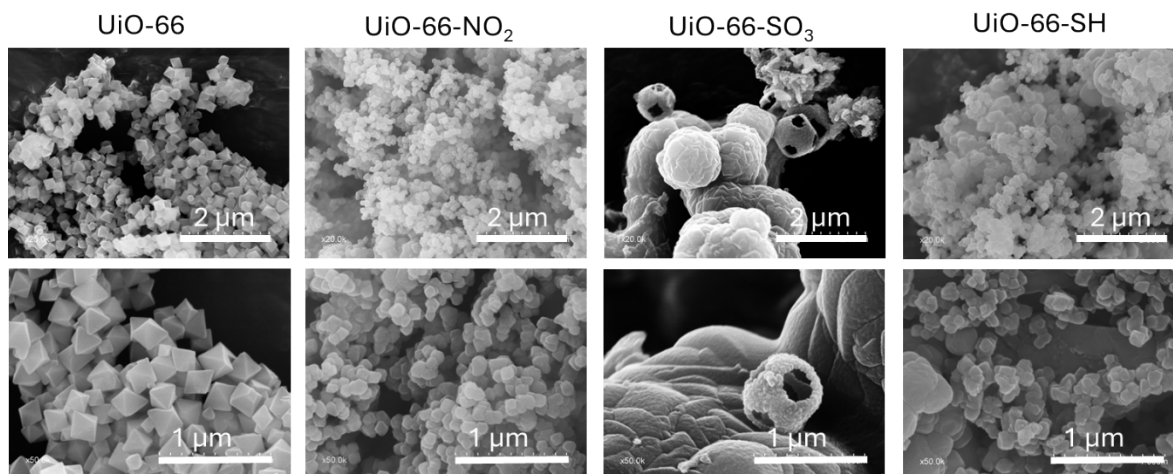
Figure S52: SEM images of single-modulated MOFs and pristine UiO-66.
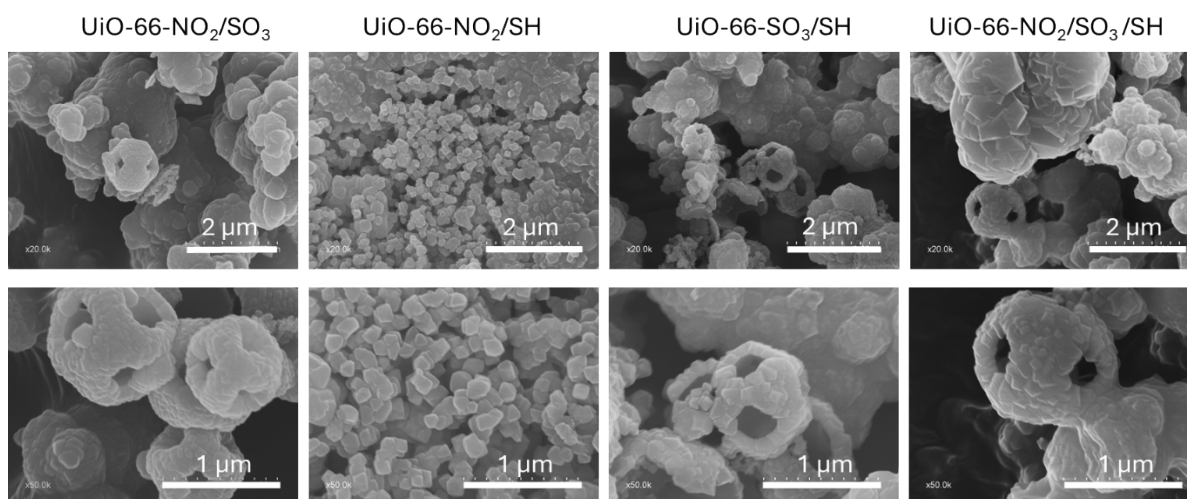
Figure S53: SEM images of multivariate modulated MOFs.

Table S12: Particle sizes of MOFs with octahedral morphology, determined by ImageJ software (50 particles).

	Average / nm	SD/ nm
UiO-66	296	49
UiO-66-NO$_2$	127	13
UiO-66-SH	115	15
UiO-66-NO$_2$/SH	160	24
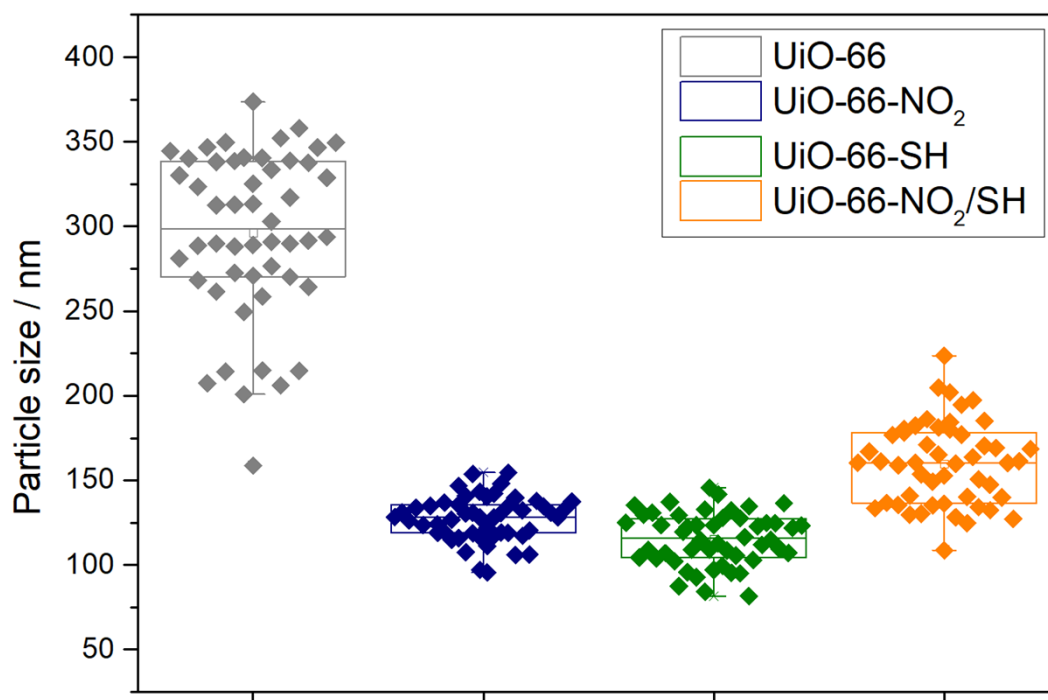
Figure S54: Box chart representation of MTVM MOFs' particle sizes. Bin size of 20 nm. Average size and standard deviation, 25% and 75% quartiles.
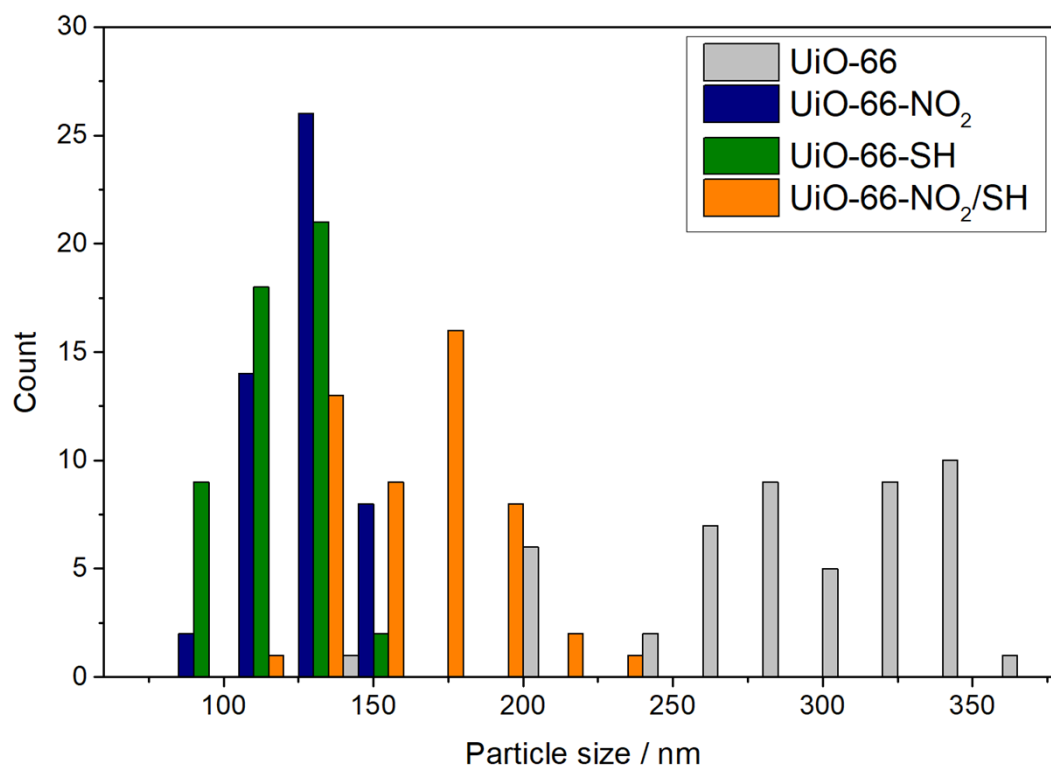
Figure S55: Histogram representation of MTVM MOFs' particle sizes. Bin size of 20 nm. Average size and standard deviation, 25% and 75% quartiles.
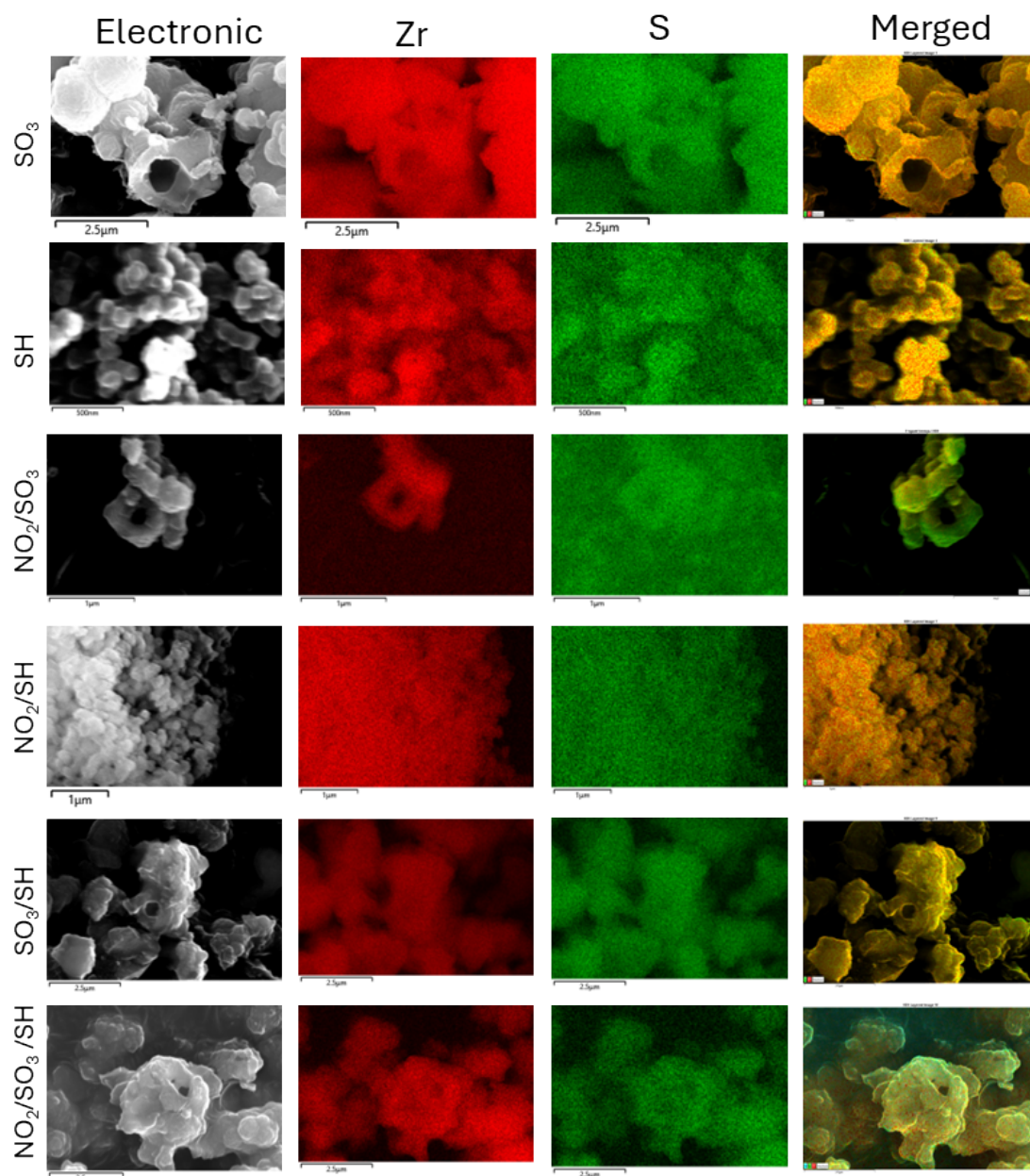
Figure S56: EDX mapping images of the S-containing samples, showing general homogenous distribution within the samples.

Table S13: Atomic S per Zr extracted by EDX measurements. Note that the spectral interference between S and Zr could result in inaccurate values for 0determination EDX.

Sample	S/Zr	SD
UiO-66-SO$_3$	0.217	0.009
UiO-66-SH	0.134	0.005
UiO-66-NO$_2$/SO$_3$	0.185	0.007
UiO-66-NO$_2$/SH	0.251	0.010
UiO-66-SO$_3$/SH	0.407	0.016
UiO-66-NO$_2$/SO$_3$/SH	0.395	0.016
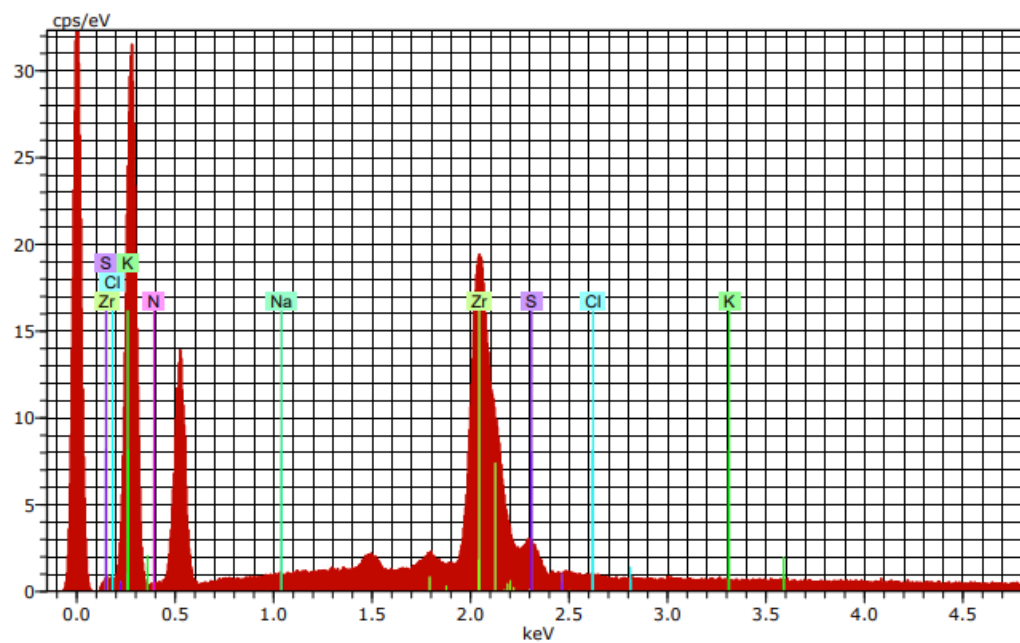
Figure S57: Example of an EDX spectrum showing the absence of K or Na SO$_3^-$ compensating species, the absence of Cl as defect-compensating species, and the proximity of Zr and S which leads to the inaccurate determination that increases the S content.

S.3.7 Z-potential and Dynamic Light Scattering (DLS)
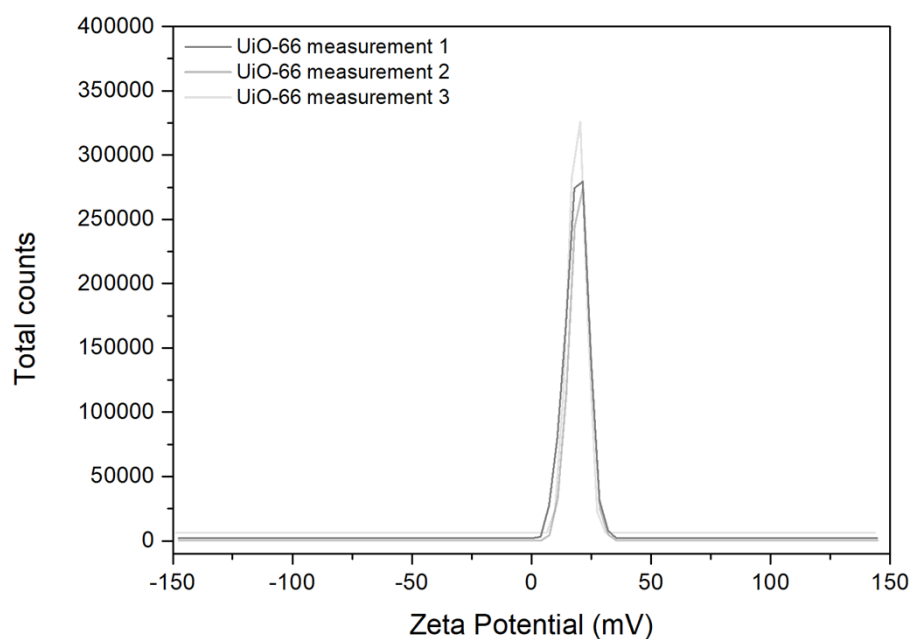
Figure S58: Z-potential of UiO-66 in water.
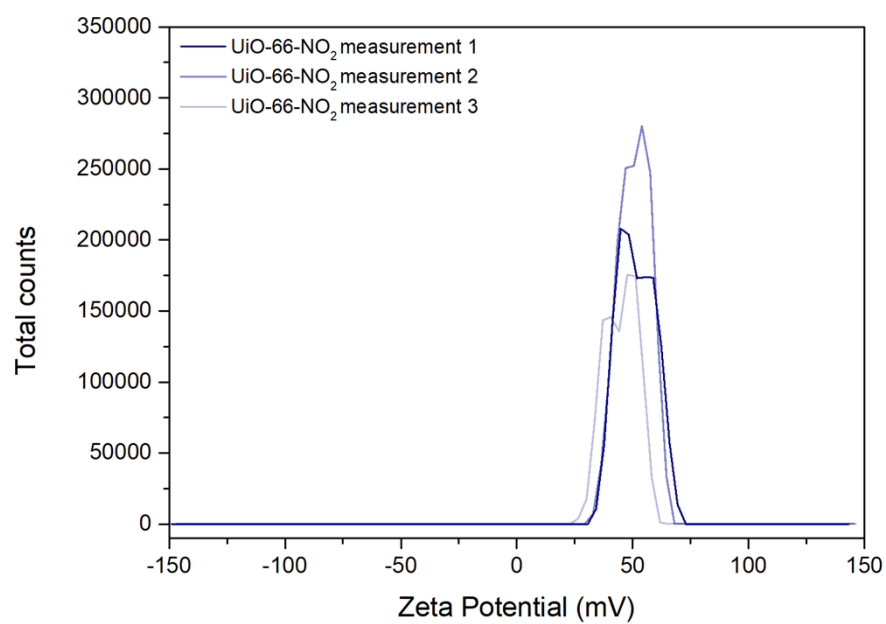
Figure S59: Z-potential of UiO-66-NO$_2$ in water.
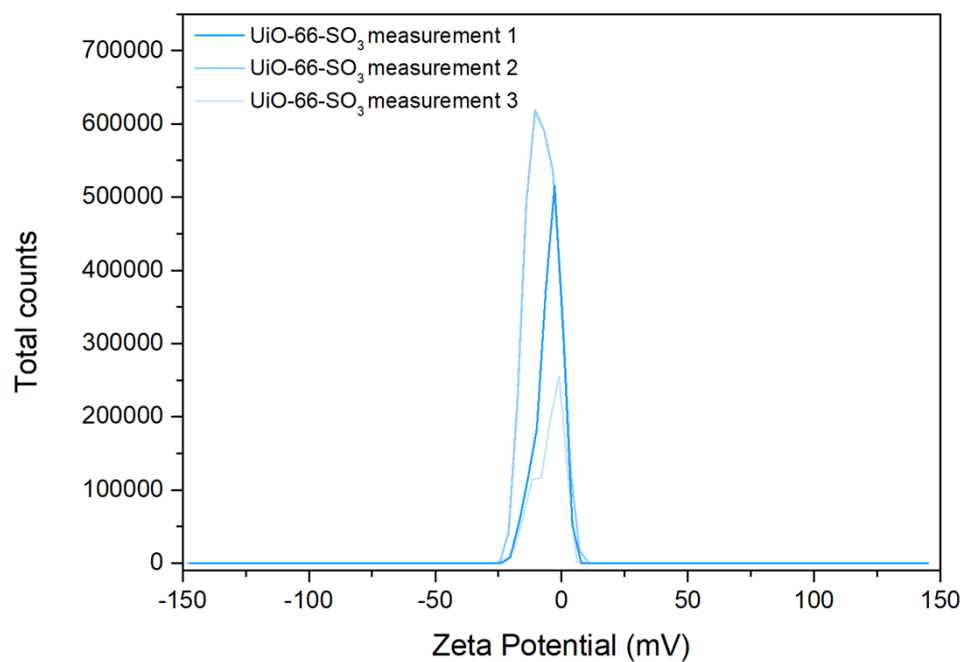
Figure S60: Z-potential of UiO-66-SO$_3$ in water.
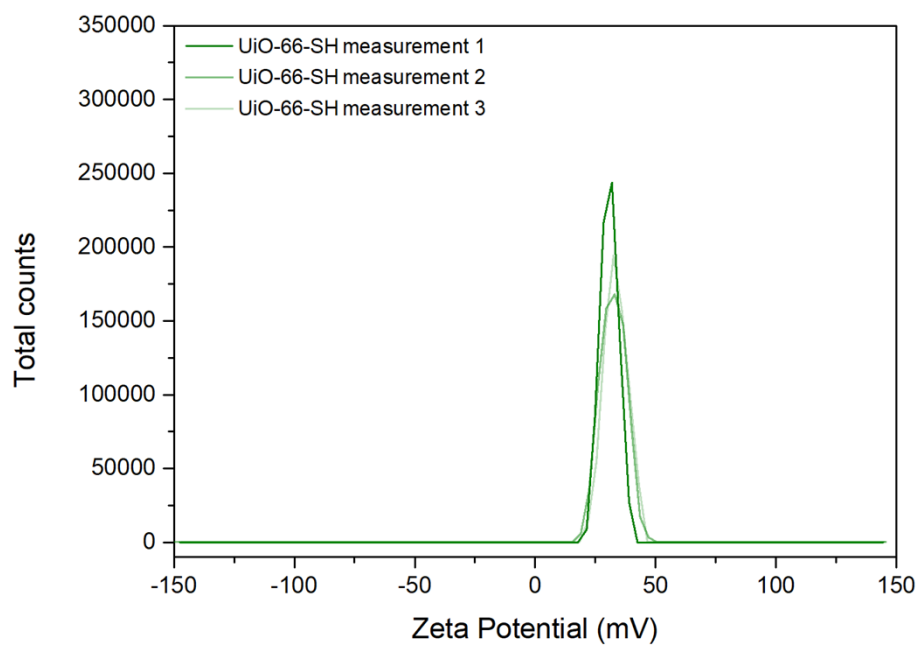
Figure S61: Z-potential of UiO-66-SH in water.
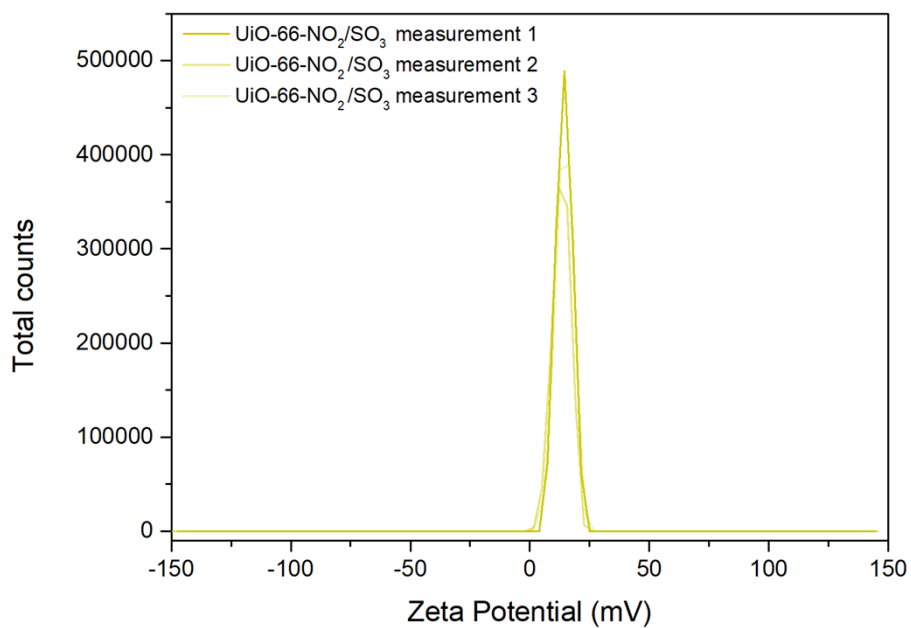
Figure S62: Z-potential of UiO-66-NO$_2$/SO$_3$ in water.
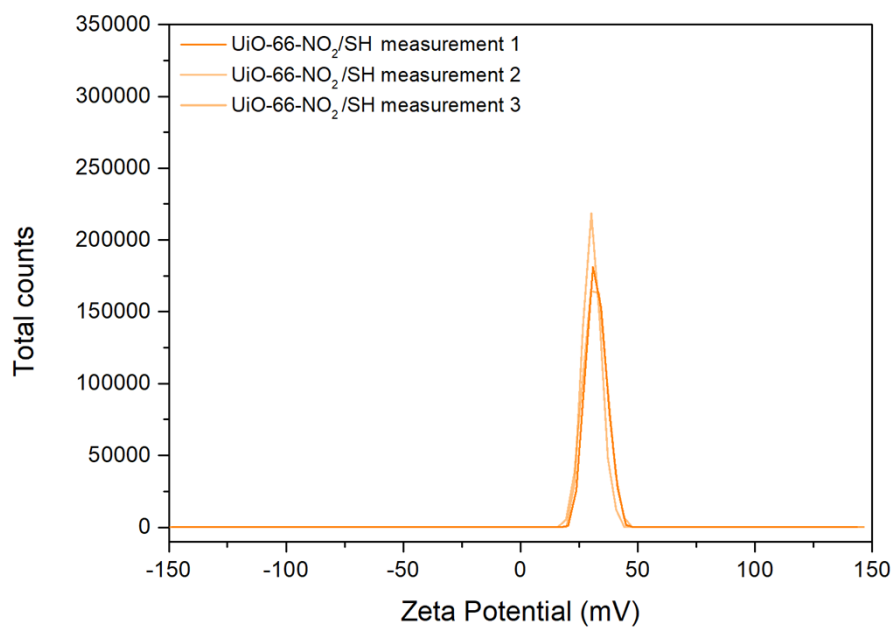
Figure S63: Z-potential of UiO-66-NO$_2$/SH in water.
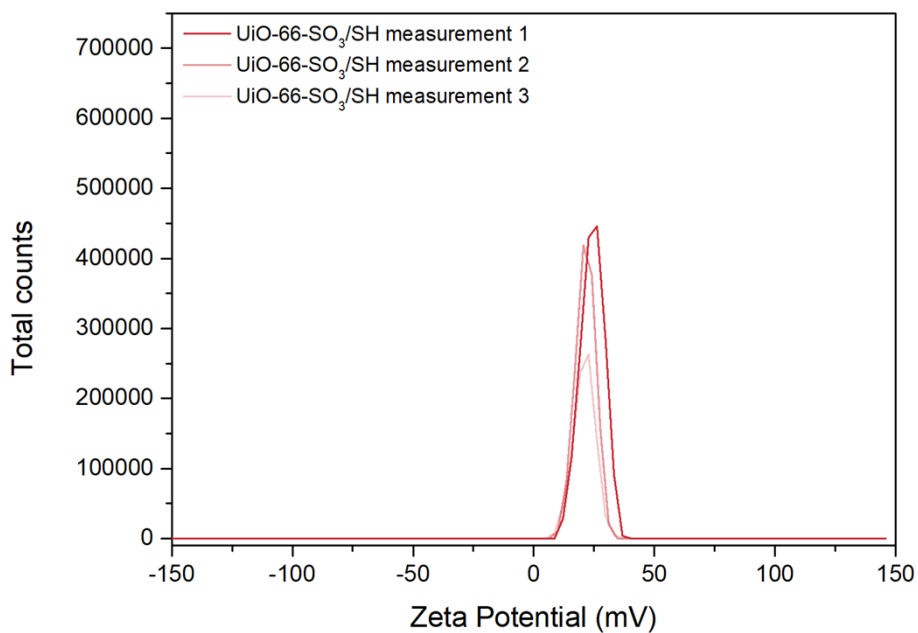
Figure S64: Z-potential of UiO-66-SO$_3$/SH in water.
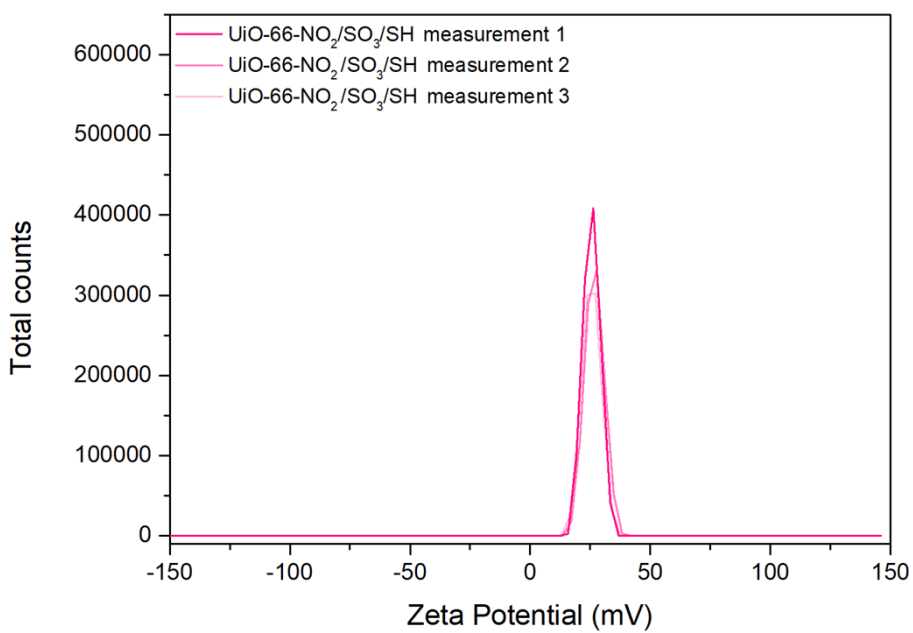
Figure S65: Z-potential of UiO-66-NO$_2$/SO$_3$/SH in water.

Table S14: Average and standard deviation values of Z-potential extracted from three measurements.

	Mean / eV	Standard Deviation / eV
UiO-66	19.234	0.621
UiO-66-NO$_2$	49.103	3.547
UiO-66-SO$_3$	-5.86	1.631
UiO-66-SH	32.205	1.331
UiO-66-NO$_2$/SO$_3$	14.029	0.647
UiO-66-NO$_2$/SH	31.587	0.854
UiO-66-SO$_3$/SH	22.219	1.774
UiO-66-NO$_2$/SO$_3$/SH	25.982	0.694
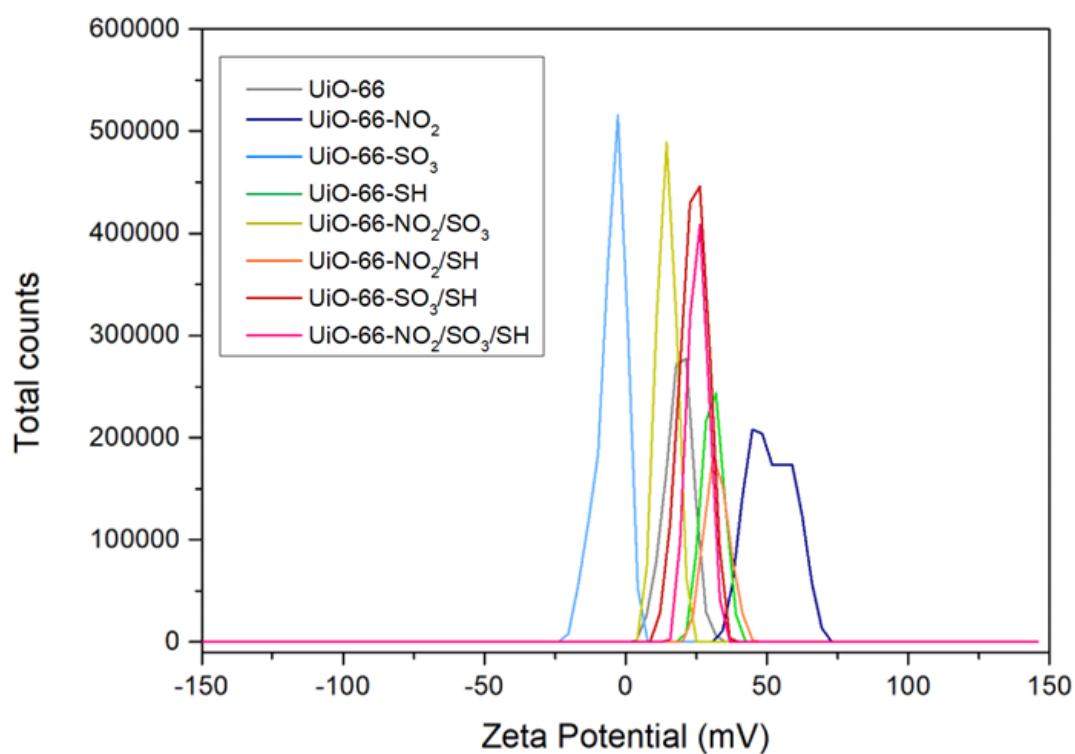
Figure S66: Comparison of the first measurement of Z-potential of UiO-66 samples.
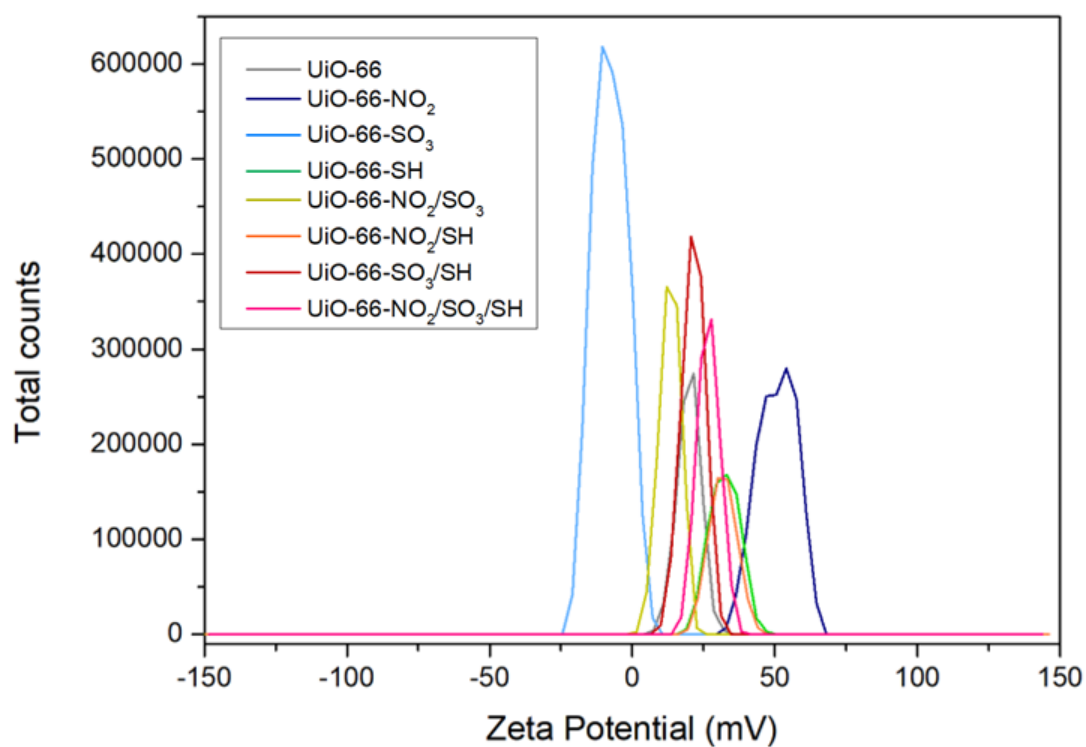
Figure S67: Comparison of the second measurement of Z-potential of UiO-66 samples.
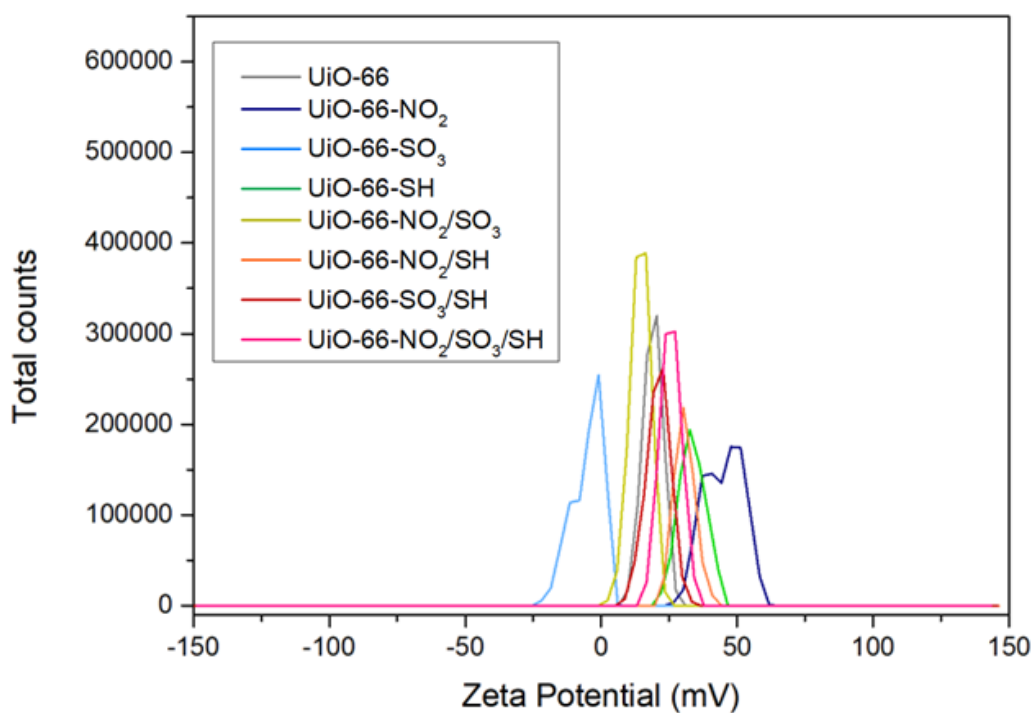
Figure S68: Comparison of the third measurement of Z-potential of UiO-66 samples.
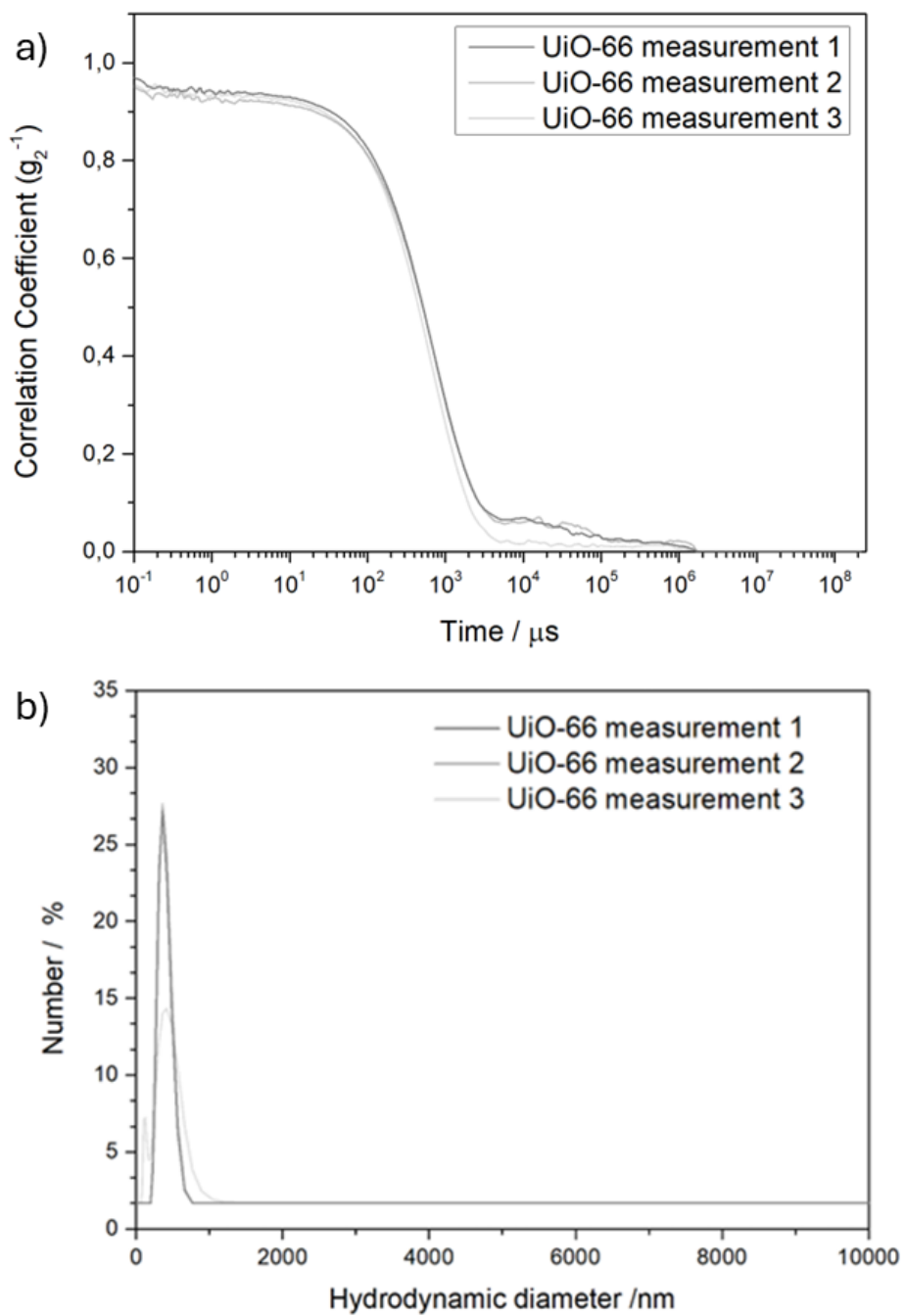
Figure S69: a) correlograms of dispersions in water and b) hydrodynamic diameters obtained from the correlograms.
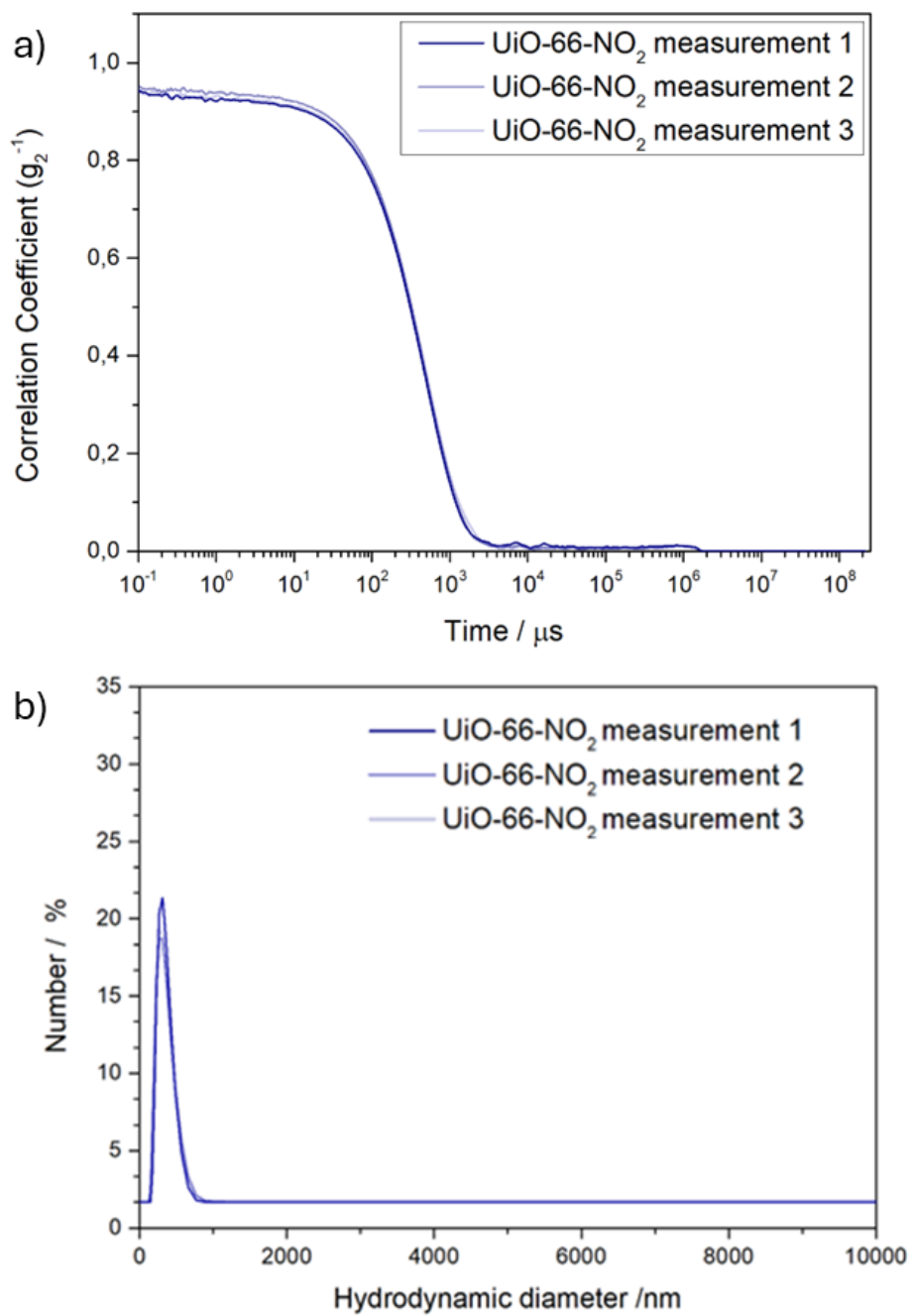
Figure S70: a) correlograms of dispersions in water and b) hydrodynamic diameters obtained from the correlograms.
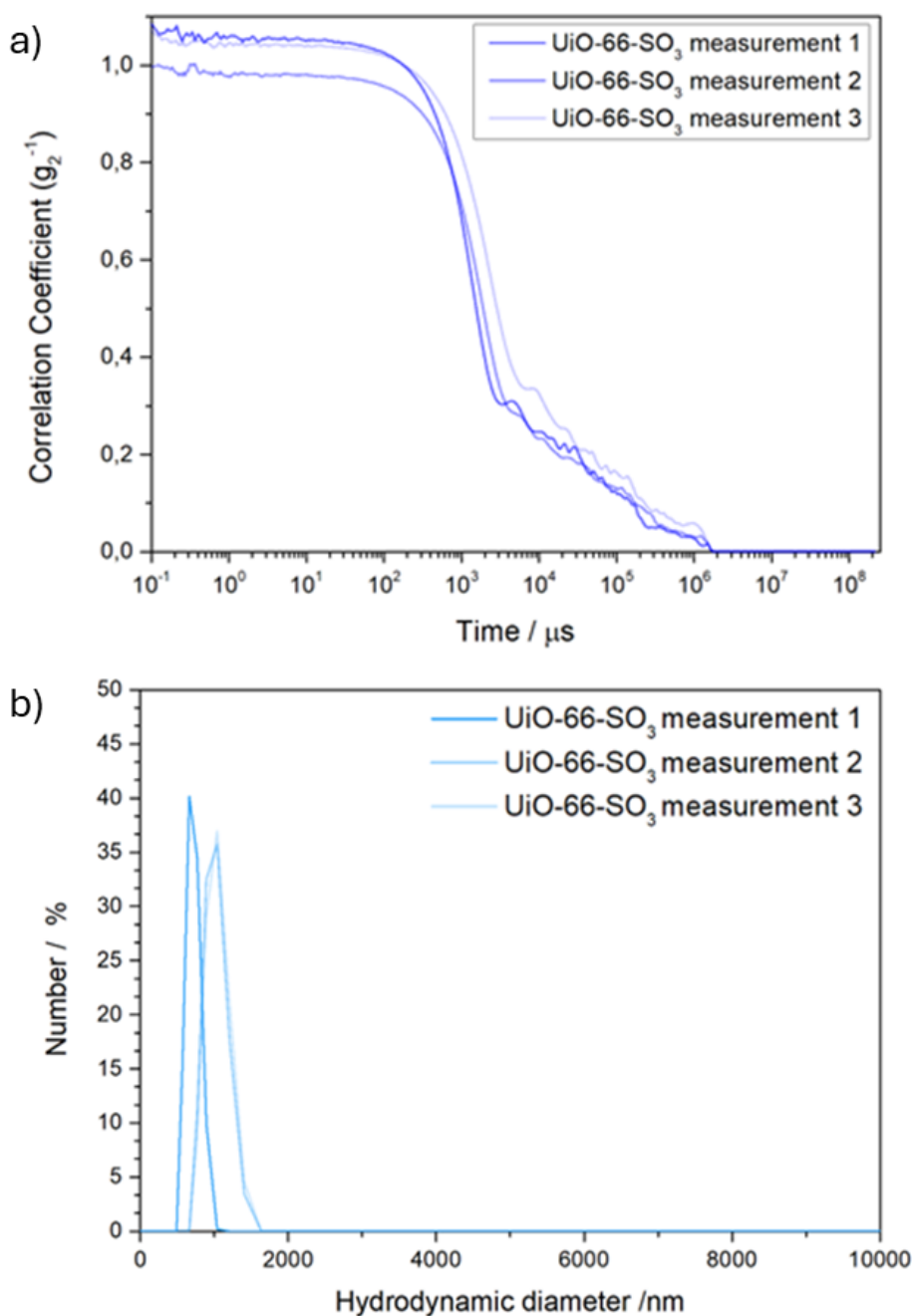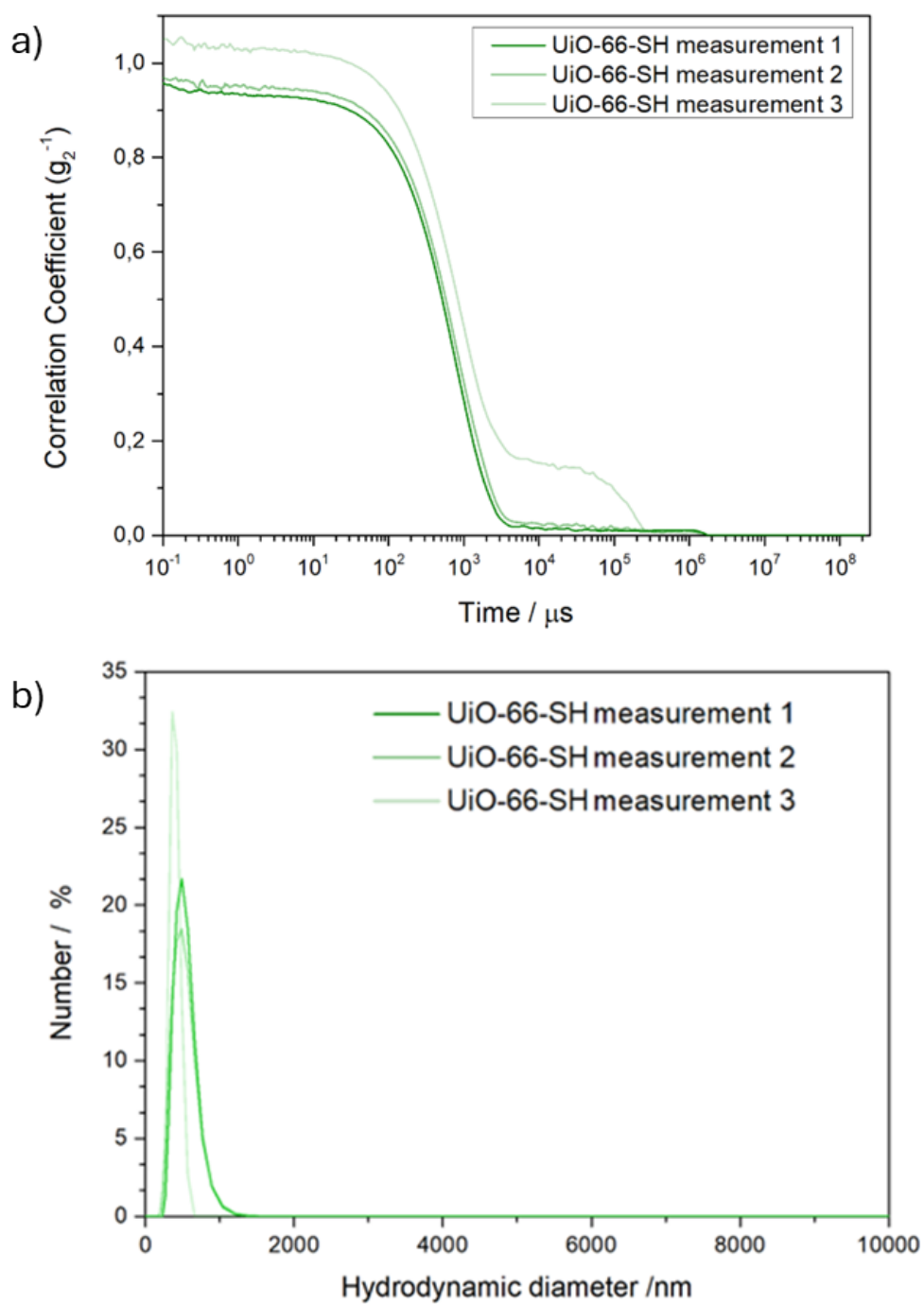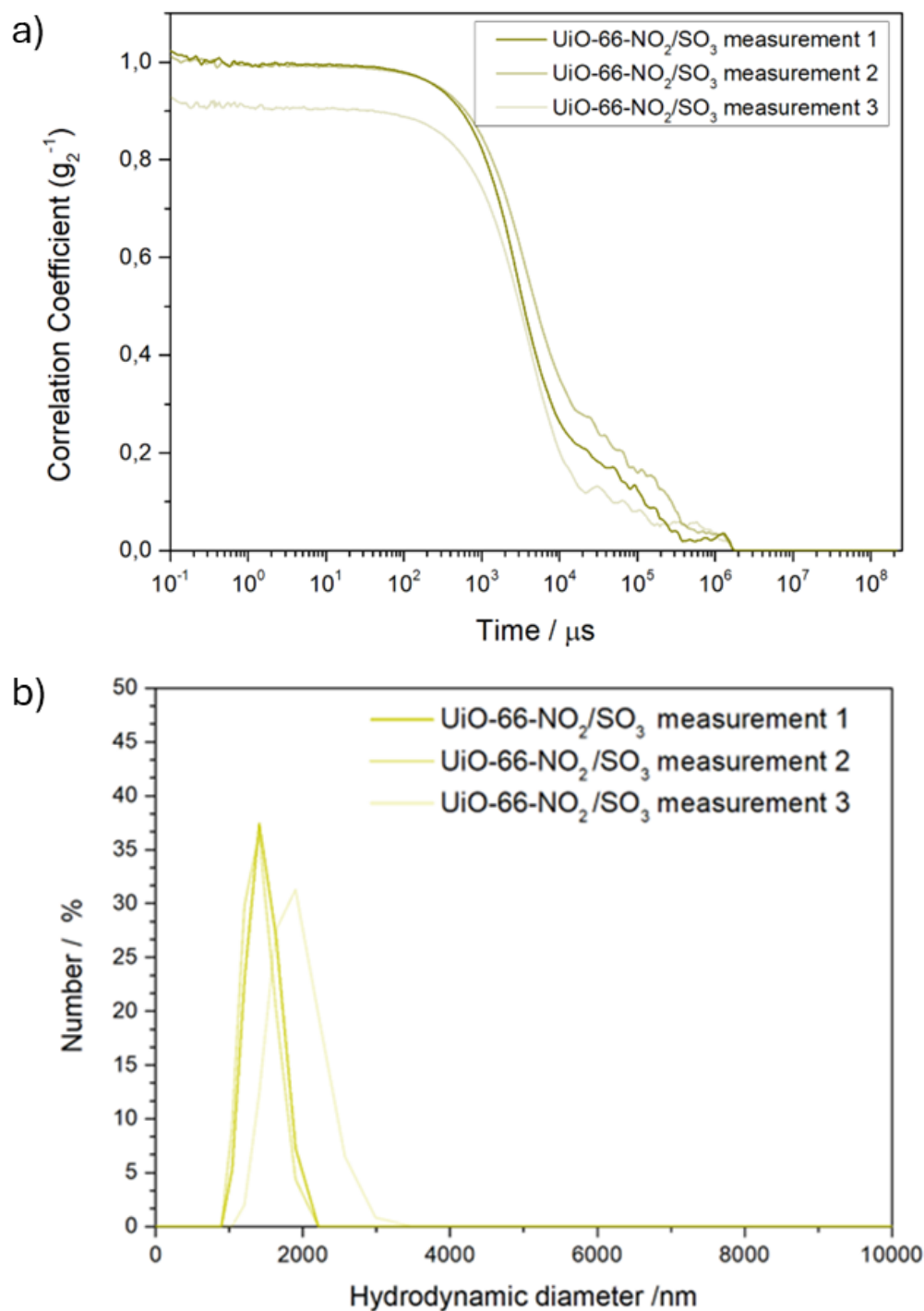
Figure S71: a) correlograms of dispersions in water and b) hydrodynamic diameters obtained from the correlograms. The correlograms show that UiO-66-SO$_3$ does not disperse well, in agreement with SEM images showing big particles. In fact, the appearance of aggregates is evident. some of which due to their high size are not present in the hydrodynamic diameter distribution.
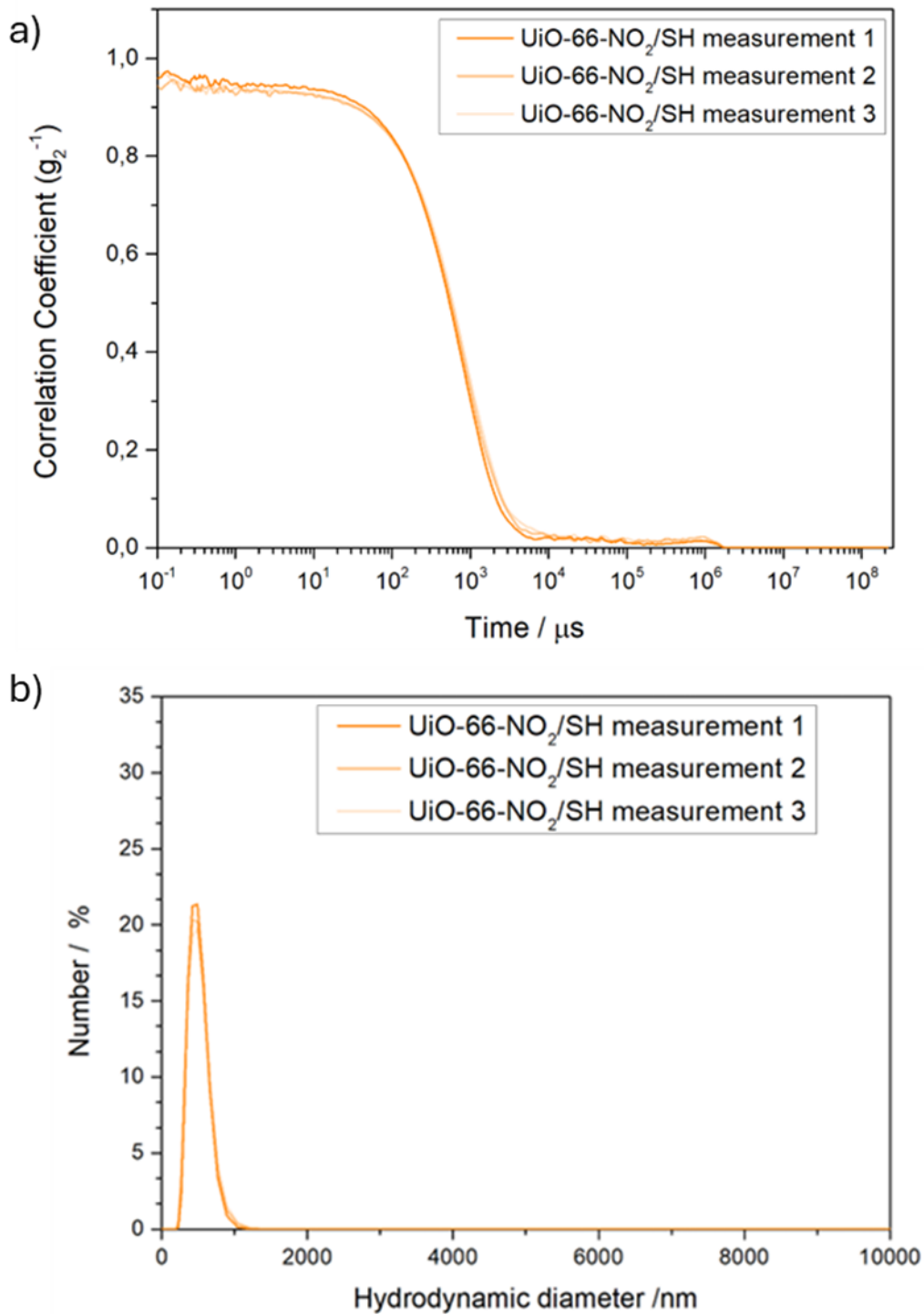
Figure S72: a) correlograms of dispersions in water and b) hydrodynamic diameters obtained from the correlograms.
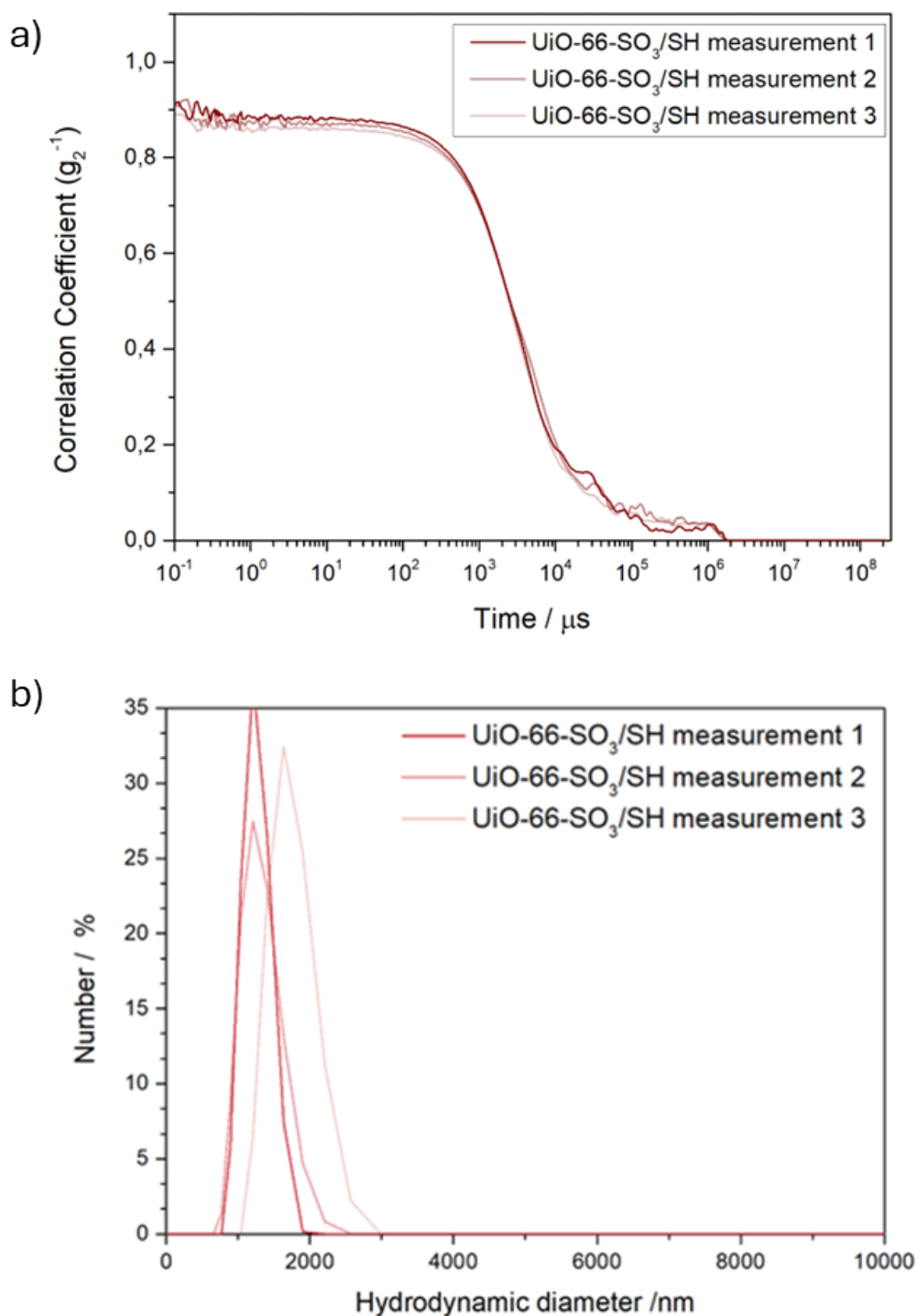
Figure S73: a) correlograms of dispersions in water and b) hydrodynamic diameters obtained from the correlograms. The correlograms show that UiO-66-NO$_2$/SO$_3$ does not disperse well, in agreement with SEM images showing big particles. The appearance of aggregates is evident. some of which due to their high size are not present in the hydrodynamic diameter distribution.
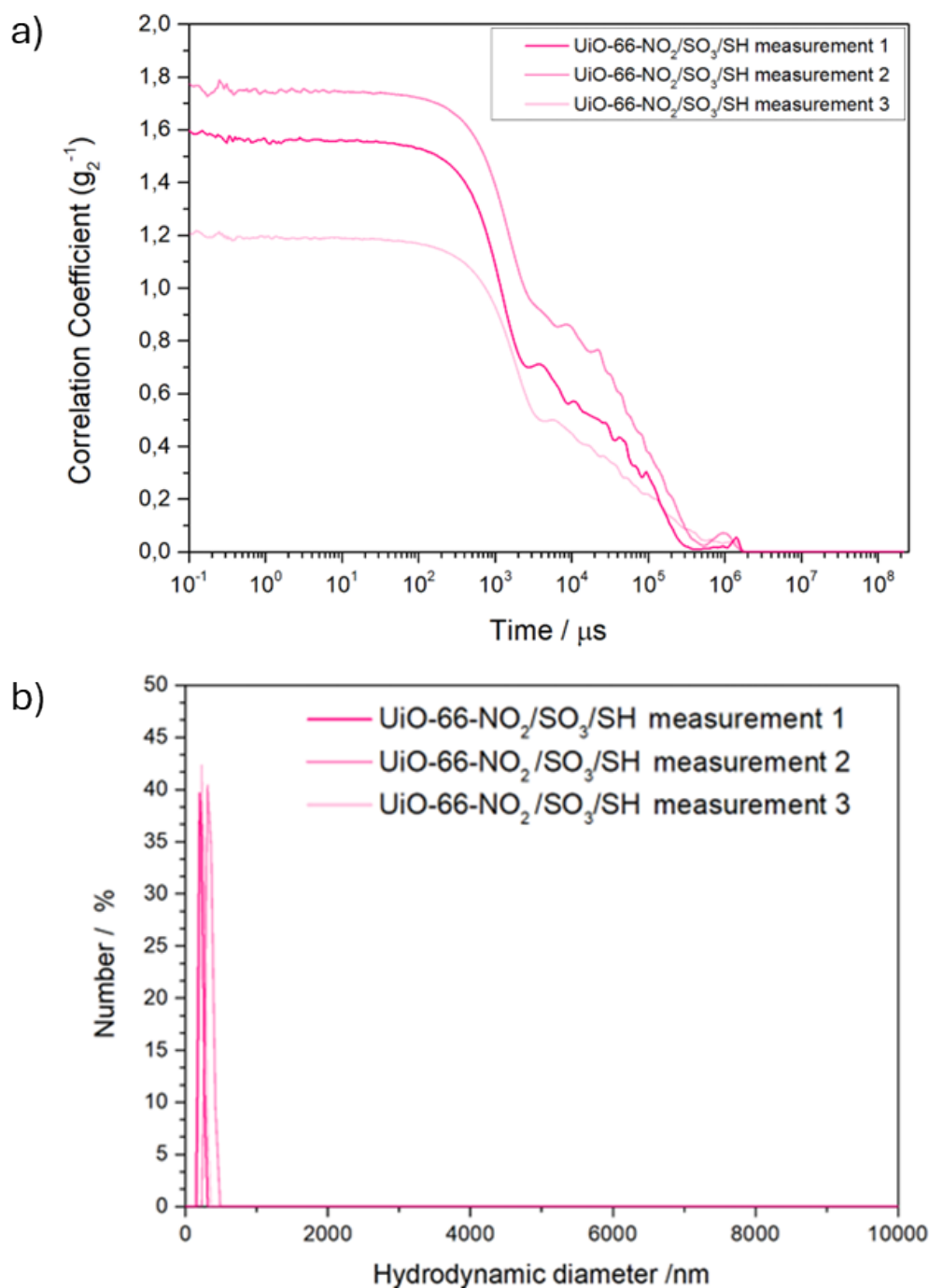
Figure S74: a) correlograms of dispersions in water and b) hydrodynamic diameters obtained from the correlograms.

Figure S75: a) correlograms of dispersions in water and b) hydrodynamic diameters obtained from the correlograms. UiO-66-SO₃/SH does not disperse well, in agreement with SEM images showing big particles. The appearance of aggregates is evident. some of which due to their high size are not present in the hydrodynamic diameter distribution.

Figure S76: a) correlograms of dispersions in water and b) hydrodynamic diameters obtained from the correlograms. The correlograms show that UiO-66-NO$_2$/SO$_3$/SH does not disperse well, in agreement with SEM images showing big particles. The appearance of aggregates is evident. some of which due to their high size are not present in the hydrodynamic diameter distribution.
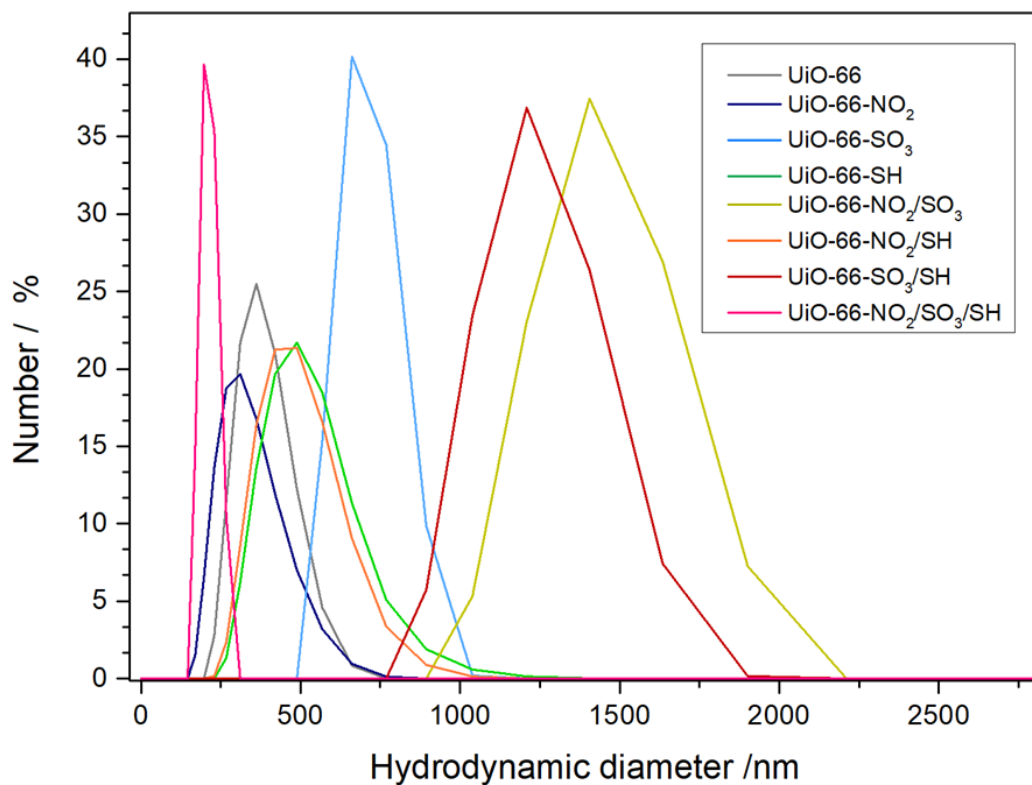
Figure S77: Comparison of the hydrodynamic diameters obtained from the correlograms. showing bigger values for the samples containing SO3 groups. in agreement with SEM showing bigger particle sizes.

S.3.8 Nitrogen Adsorption and Desorption Measurements

Table S15: Tabulated data extracted from N_2 adsorption and desorption measurements of UiO-66 MOFs showing a general increase in surface area, microporosity and total pore volumes.

Sample	S_{BET}	S_{MICRO}	S_{EXT}	V_{TOTAL}	V_{MICRO}	V_{MESO}
	(m^2/g)	(m^2/g)	(m^2/g)	(cm^3/g)	(cm^3/g)	(cm^3/g)
UiO-66	1315	1280	35	0.516	0.482	0.482
UiO-66-NO_2	1449	1346	103	0.587	0.507	0.08
UiO-66-SO_3	1296	1159	137	0.546	0.468	0.079
UiO-66-SH	1339	1248	91	0.539	0.452	0.087
UiO-66-NO_2/SO_3	1359	1244	115	0.548	0.476	0.072
UiO-66-NO_2/SH	1428	1343	85	0.530	0.472	0.058
UiO-66-SO_3/SH	1266	1155	111	0.52	0.446	0.074
UiO-66-NO_2/SO_3/SH	1348	1231	117	0.54	0.466	0.074

Note that in all cases S_{BET} corresponds to Brunauer–Emmett–Teller surface area. S_{micro} to micropore surface area. S_{ext} to the external surface area. V_{micro} to micropore volume. V_{meso} to mesopore volume and V_{total} to total pore volume.

V_{micro} was calculated using the *t*-plot model with the Harkins and Jura thickness curve based on the BET surface areas. V_{total} was calculated at $P/P_0 = 0.9$, before the inter-particle space and $V_{meso} = V_{total} - V_{micro}$. The pore size distributions were calculated applying the model that provided the lowest fitting error, NLDFT pillared clay cylindrical pore model.
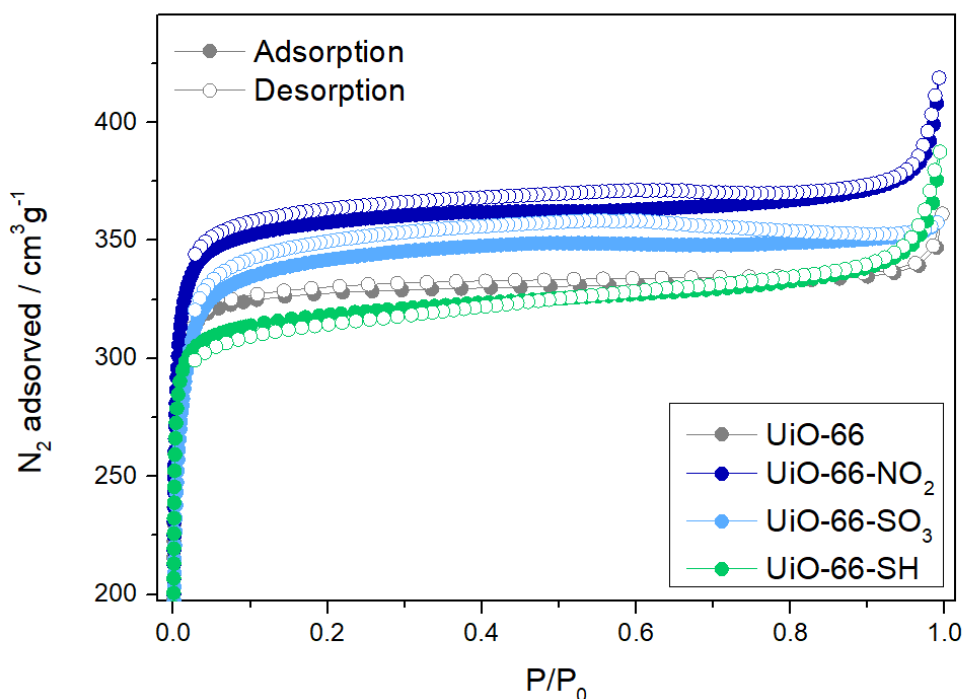
Figure S78: N_2 adsorption and desorption isotherms of single-modulated MOFs compared to pristine UiO-66.
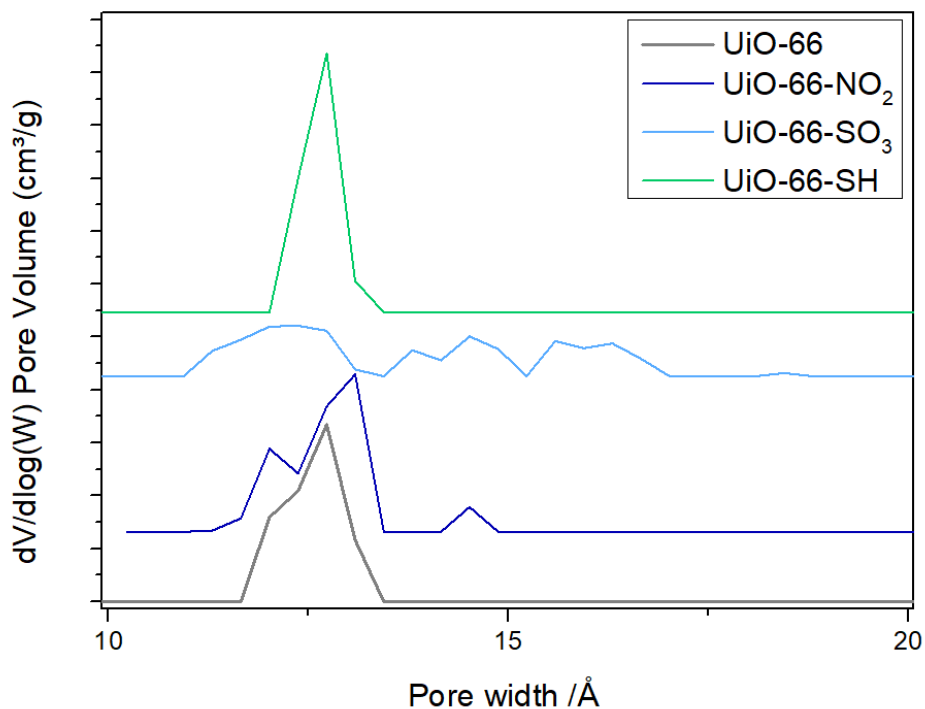

Figure S79: Comparison of pore size distributions of single-modulated MOFs compared to pristine UiO-66.
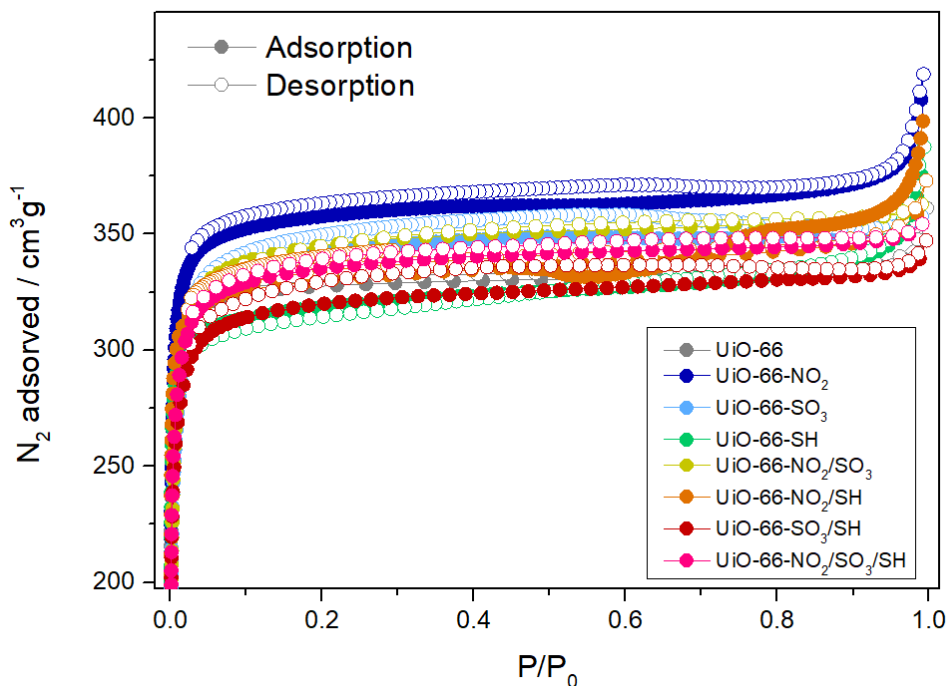

Figure S80: Comparison of N_2 adsorption and desorption isotherms of single-modulated di-modulated and tri-modulated MOFs compared to pristine UiO-66.
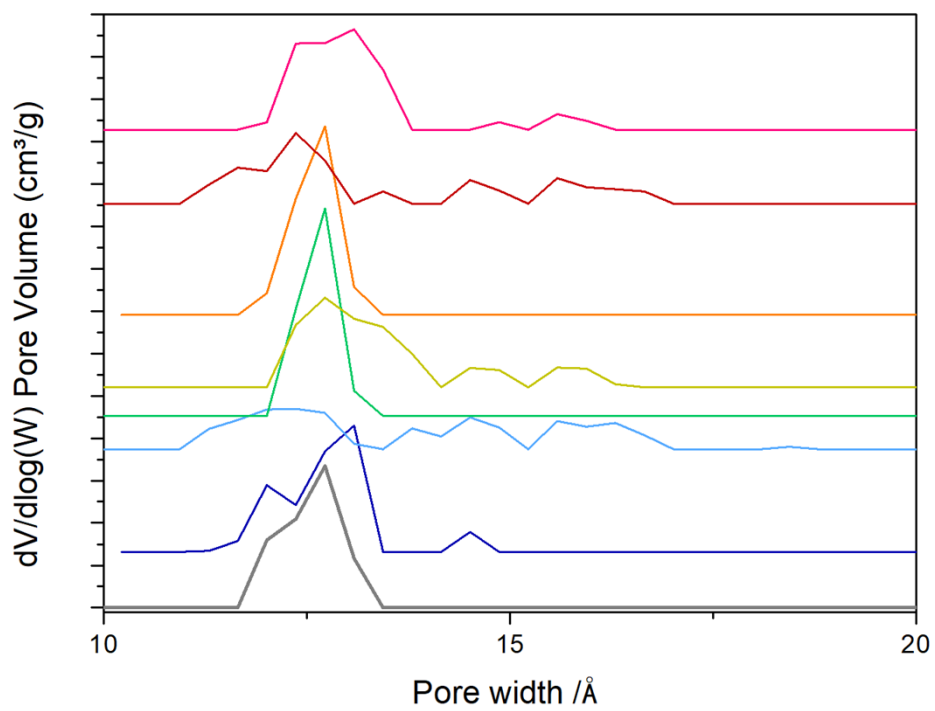
Figure S81: Comparison of stacked pore size distributions of single-modulated, di-modulated and tri-modulated MOFs compared to pristine UiO-66.

S.3.9 Photoluminescence

Photoluminescence (PL) emissions were measured at room temperature using a MonoSpec 27 Jarrel-Ash monochromator coupled with a Hamamatsu R446 photomultiplier using excited by an Innova Argon-ion laser. (λ_{exc} = 350.7 nm; 2.57 eV. 200 mW). The PL emission spectra were deconvoluted using Voigt-type functions with PeakFit™ software fixing three distinct components located at 410, 481, and 542 nm for all spectra.
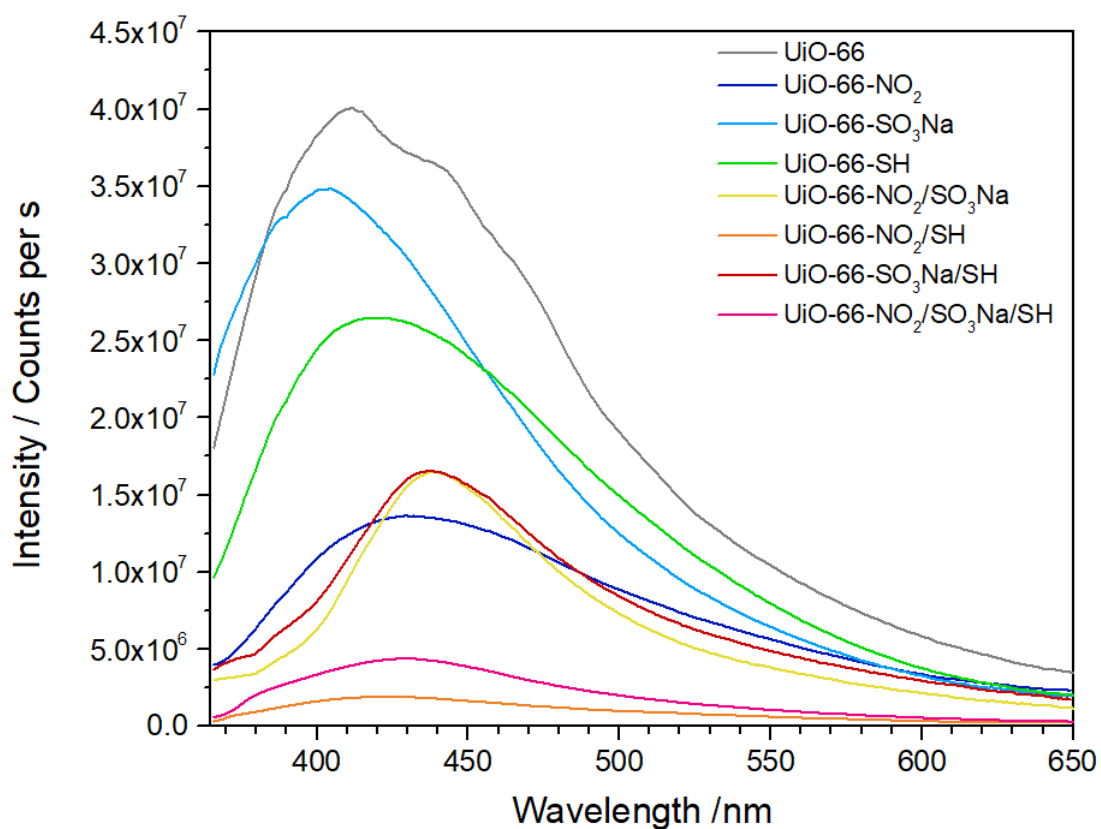
Figure S82: PL emission spectra for the samples.
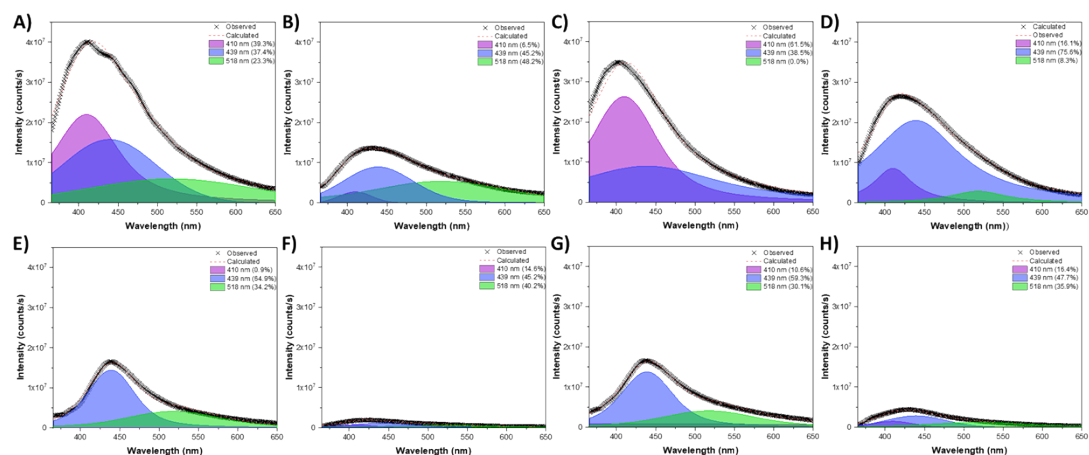
Figure S83. PL deconvolution spectra of the samples **A)** UiO-66. **B)** UiO-66-NO$_2$. **C)**. UiO-66-SO$_3$Na. **D)** UiO-66-SH. **E)** UiO-66-NO$_2$/SO$_3$Na. **F)** UiO-66-NO$_2$/SH. **G)** UiO-66- SO$_3$Na/SH. and **H)** UiO-66-NO$_2$/SO$_3$Na/SH.

When using the -NO$_2$ and -SH modulators, a reduction in the contribution of more energetic defects (410 nm) is observed compared to the pristine sample, reaching values of 6.5% and 16.1%, respectively. This reduction coincides with the analysis of the maximum emission wavelength, which shows the generation of less energetic intermediate levels. With the -SO$_3$ modulator, the opposite behaviour is observed; there is an intensification of the contribution of higher energy (61.5%). For samples with multiple modulators, the same behaviour is observed, showing a sharp reduction in the most energetic defects, indicating that these are directly connected to the new linkers obtained through the use of Benz-SO$_3$.
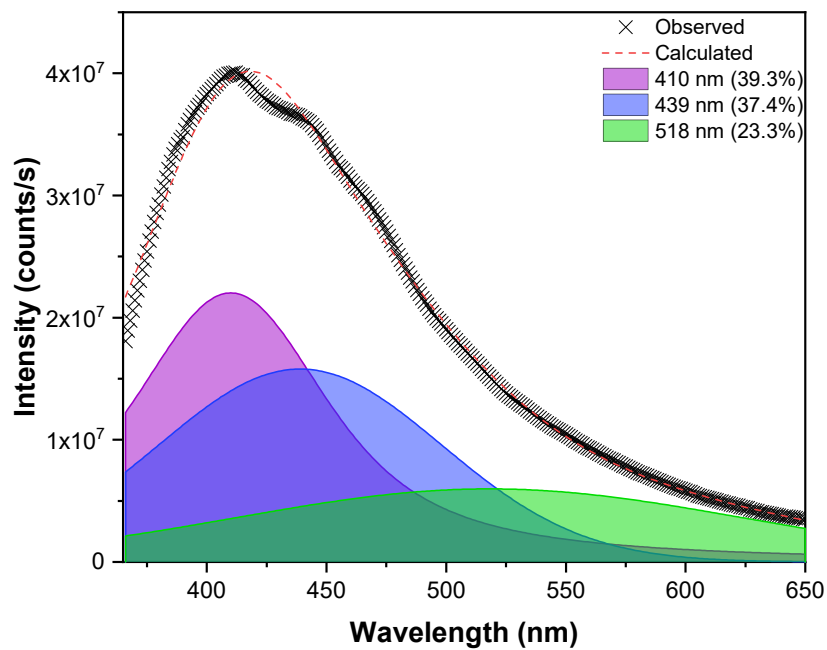
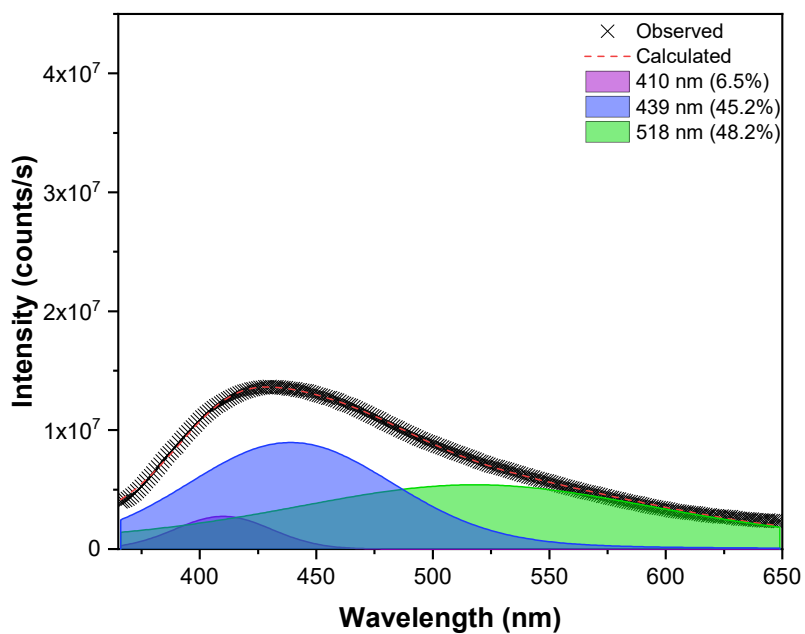**Figure S84.** PL deconvolution spectra of UiO-66

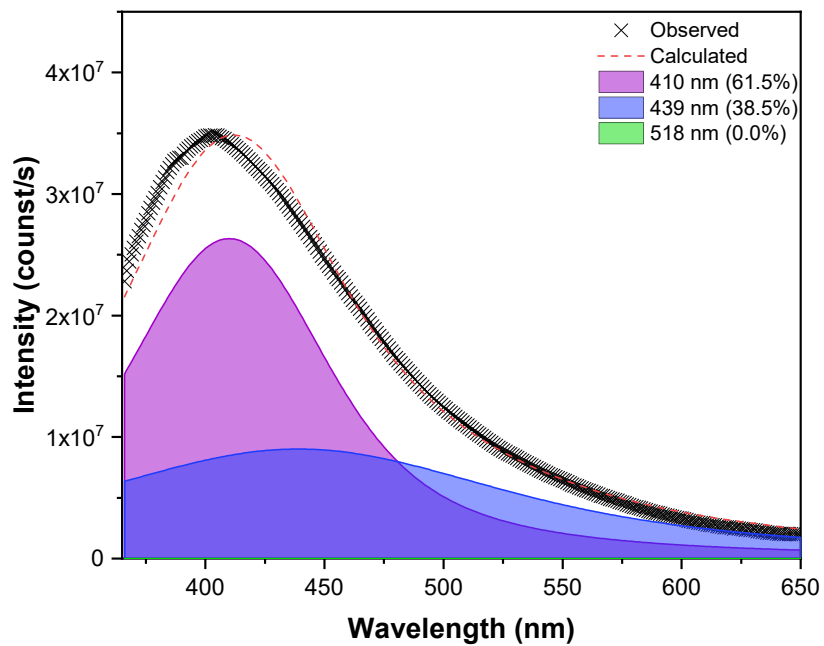**Figure S85.** PL deconvolution spectra of UiO-66-NO$_2$.
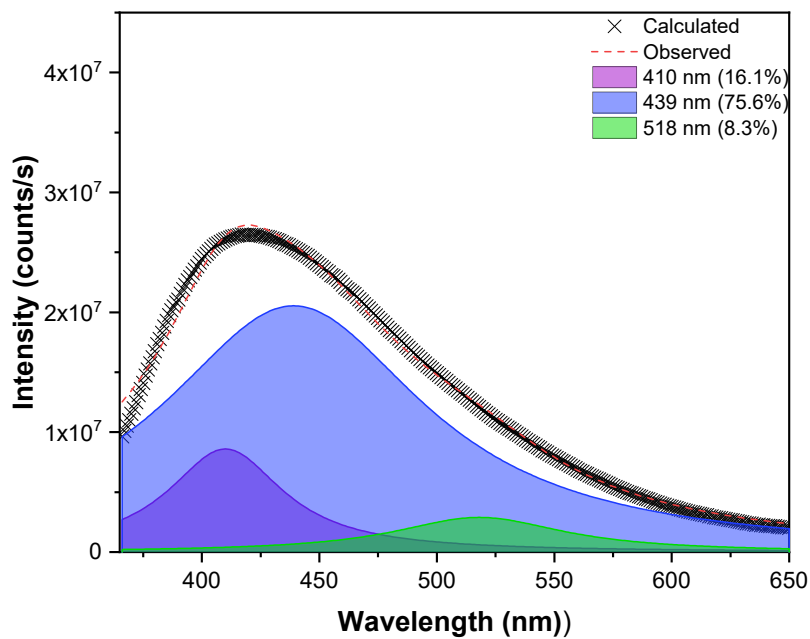
Figure S86. PL deconvolution spectra of UiO-66-SO$_3$.

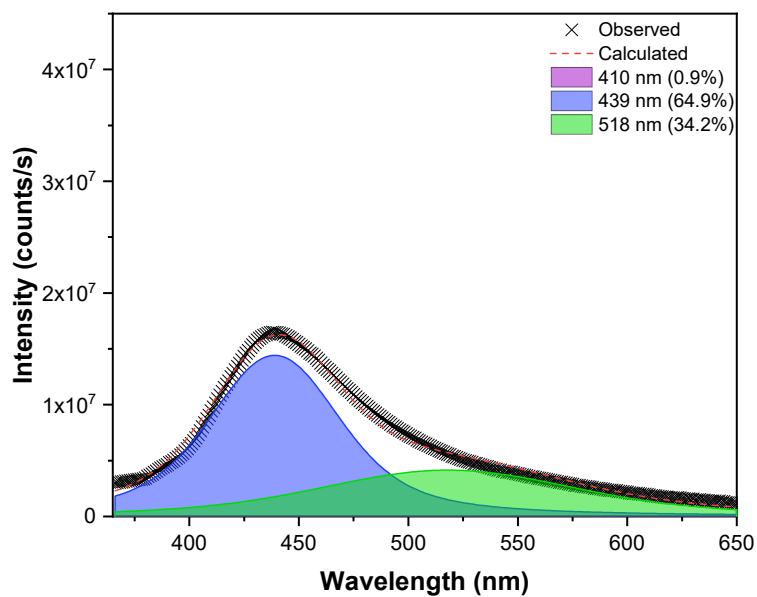**Figure S87.** PL deconvolution spectra of UiO-66-SH.
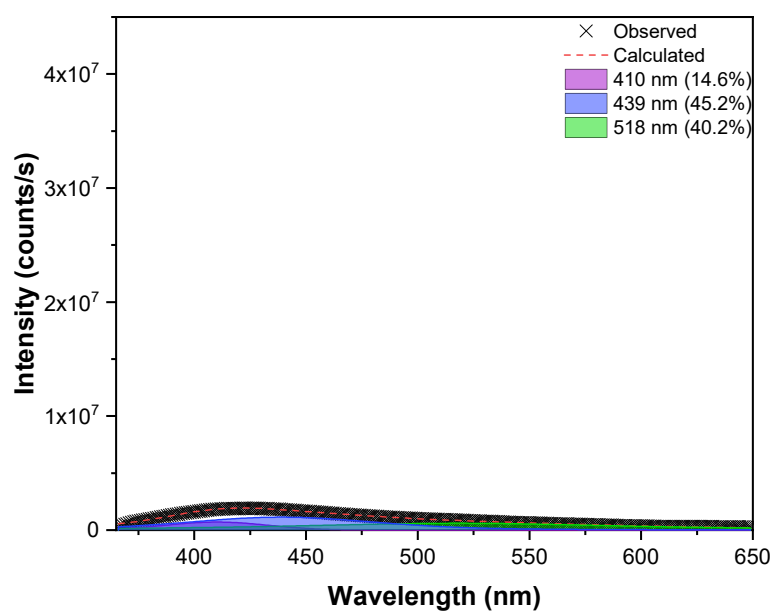
Figure S88. PL deconvolution spectra UiO-66-NO$_2$/SO$_3$.
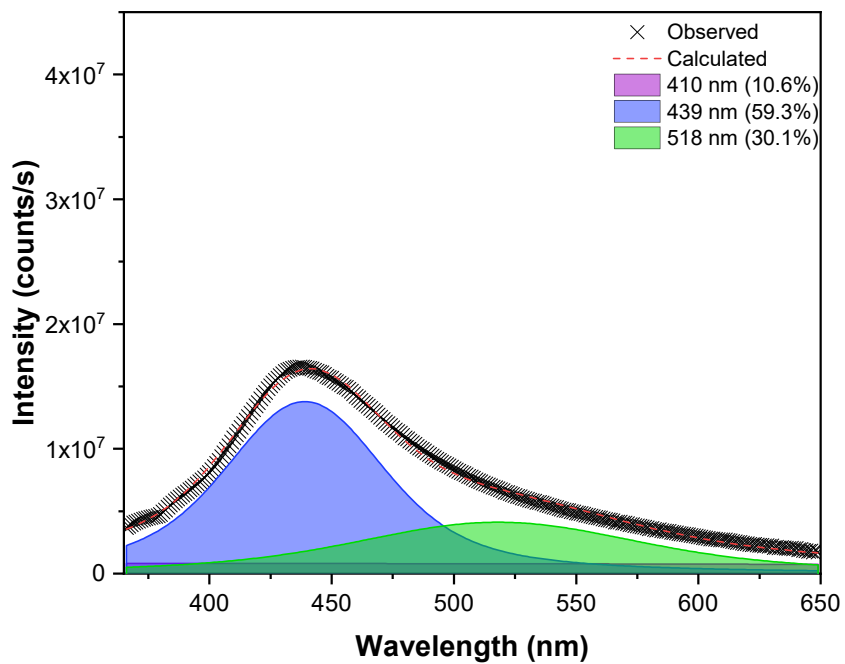

Figure S89. PL deconvolution spectra of UiO-66-NO$_2$/SH.

Figure S90. PL deconvolution spectra of UiO-66- SO$_3$/SH.
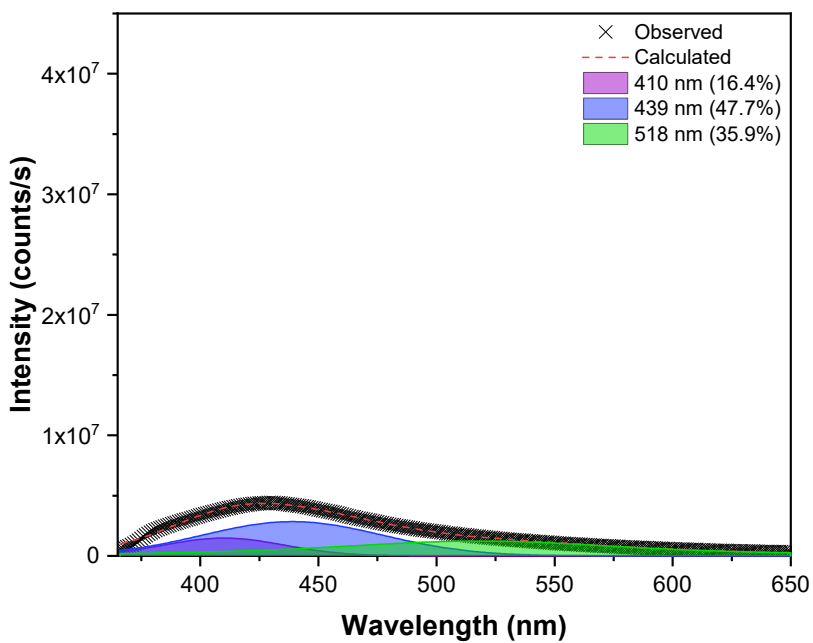

Figure S91. PL deconvolution spectra of UiO-66-NO$_2$/SO$_3$/SH.
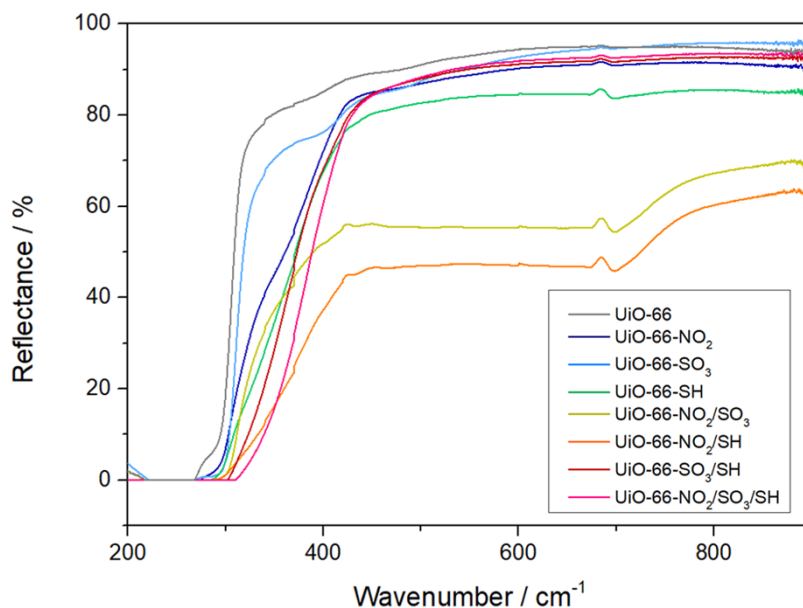
S.3.10 Band Gap

Figure S92: Diffuse reflectance spectra of the MOFs.
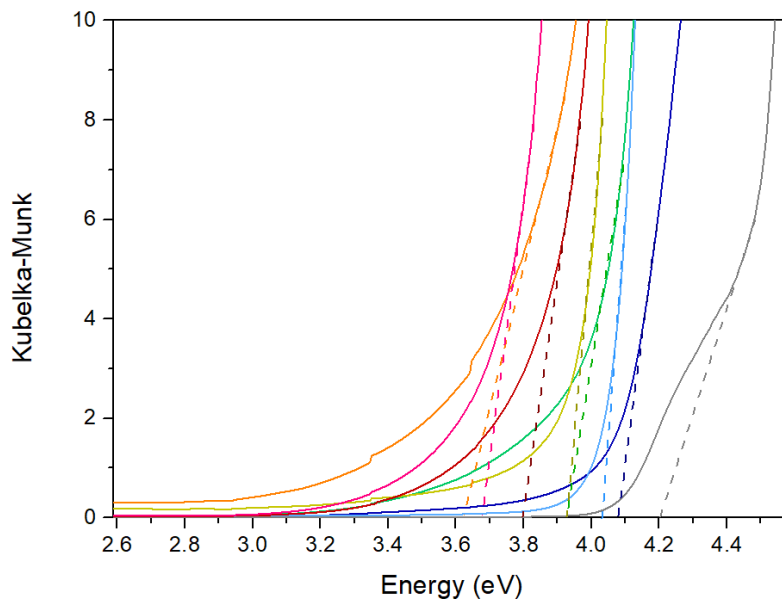

Figure S93: Kubelka Munk and Tau plots of the MOFs. Legend from Figure S92 applies.

Table S16: Extracted band gap estimated values for the Kulbelka Munk and Tau plots.

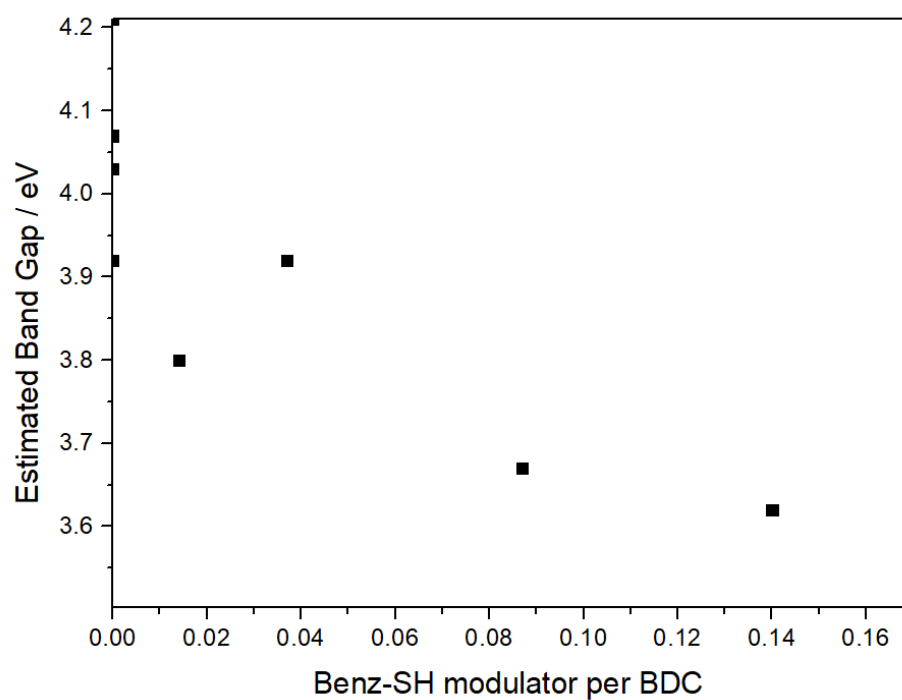| Sample	Band Gap (eV)
UiO-66	4.21
UiO-66-NO$_2$	4.07
UiO-66-SO$_3$	4.03
UiO-66-SH	3.92
UiO-66-NO$_2$/SO$_3$	3.92
UiO-66-NO$_2$/SH	3.62
UiO-66-SO$_3$/SH	3.80
UiO-66-NO$_2$/SO$_3$/SH	3.67

Figure S94: Estimated band gap as a function of the Benz-SH modulator per BDC.
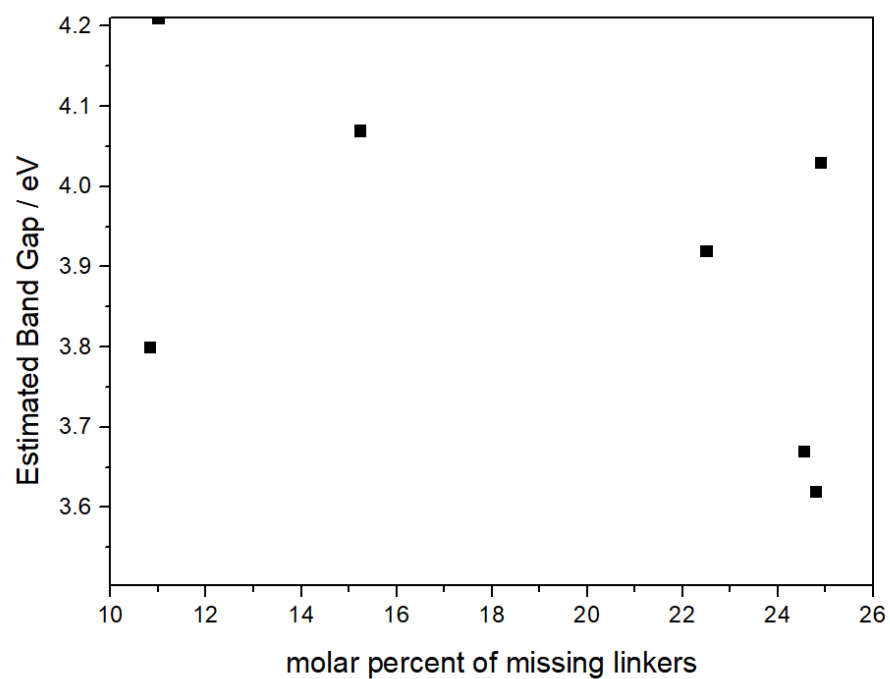

Figure S95: Estimated band gap as a function of the molar percent of missing linkers.
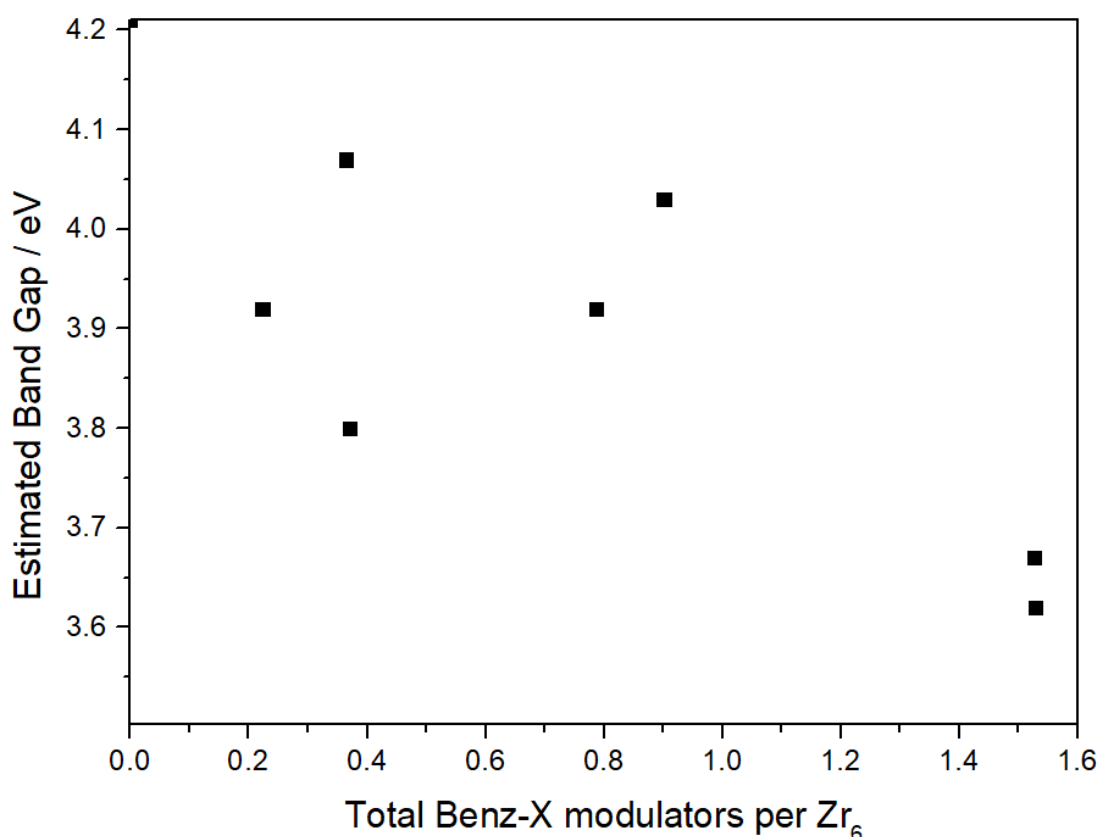
Figure S96: Estimated band gap as a function of the total modulators per Zr_6.

S.4 References

1 a) A. K. Soper and E. R. Barney, *J. Appl. Crystallogr.*, 2011, **44**, 714–726. B) A. K. Soper, GudrunN and GudrunX: programs for correcting raw neutron and X-ray diffraction data to differential scattering cross section, 2011.

2 D. A. Keen, *J. Appl. Crystallogr.*, 2001, **34**, 172–177.

3 C. L. Farrow, P. Juhas, J. W. Liu, D. Bryndin, E. S. Božin, J. Bloch, T. Proffen and S. J. L. Billinge, *J. Phys.: Condens. Matter.*, 2007, **19**, 335219-335227.

4 L. Liu, Z. Chen, J. Wang, D. Zhang, Y. Zhu, S. Ling, K.-W. Huang, Y. Belmabkhout, K. Adil, Y. Zhang, B. Slater, M. Eddaoudi and Y. Han, *Nat. Chem.*, 2019, **11**, 622–628.

5 G. C. Shearer, S. Chavan, S. Bordiga, S. Svelle, U. Olsbye and K. P. Lillerud, *Chem. Mater.*, 2016, **28**, 3749–3761.

6 X. Feng, J. Hajek, H. S. Jena, G. Wang, S. K. P. Veerapandian, R. Morent, N. D. Geyter, K. Leyssens, A. E. J. Hoffman, V. Meynen, C. Marquez, D. E. D. Vos, V. V. Speybroeck, K. Leus and P. V. D. Voort, *J. Am. Chem. So.c*, 2020, **142**, 3174–3183.

7 L. Valenzano, B. Civalleri, S. Chavan, S. Bordiga, M. H. Nilsen, S. Jakobsen, K. P. Lillerud and C. Lamberti, *Chem. Mater.*, 2011, **23**, 1700–1718.

8 I. A. Lázaro, *Eur J Inorg Chem,* 2020, **2020**, 4284-4294.